THE INFLUENCE OF HEAT TREATMENT ON CORROSION BEHAVIOR OF

MARTENSITIC STAINLESS STEEL UNS 42670

by

Armen Kvryan

A dissertation

submitted in partial fulfillment

of the requirements for the degree of

Doctor of Philosophy in Materials Science and Engineering

Boise State University

May 2019

BOISE STATE UNIVERSITY GRADUATE COLLEGE

DEFENSE COMMITTEE AND FINAL READING APPROVALS

of the dissertation submitted by

Armen Kvryan

Dissertation Title: The Influence of Heat Treatment on Corrosion Behavior of Martensitic Stainless Steel – UNS-42670

Date of Final Oral Examination: 08 April 2019

The following individuals read and discussed the dissertation submitted by student Armen Kvryan, and they evaluated his presentation and response to questions during the final oral examination. They found that the student passed the final oral examination.

Michael Hurley, Ph.D.   Chair, Supervisory Committee

Brian J. Jaques, Ph.D.   Member, Supervisory Committee

Hui (Claire) Xiong, Ph.D.   Member, Supervisory Committee

Hitesh Trivedi   Member, Supervisory Committee

The final reading approval of the dissertation was granted by Michael Hurley, Ph.D., Chair of the Supervisory Committee. The dissertation was approved by the Graduate College.

ACKNOWLEDGEMENTS

that I can do the same. Finally, I must thank my very patient wife, Christina, who has always believed in me and made me realize how much impact a single person can have on one's life. Though a thousand miles away, you have been my rock in this difficult endeavor and I would not be able to have done this without you. I love you and am confident that this shows that we will be able to tackle any obstacles that we may encounter. I only hope that I can be as much of an inspiration for you as you have been for me.

If opportunity doesn't knock, build a door.

– Milton Berle

ABSTRACT

Ceaseless demand for lighter, faster, and more efficient aircraft has been one of the greatest driving forces behind bearing steel innovations. Recent studies demonstrate that corrosion is one of the leading causes of bearing failure in both military and commercial aircraft. High-performing bearing steels are available but are not being used in US military applications due to high cost and security issues when steels are produced outside of the continental United States. One approach to address this issue is to engineer steels that are cost-efficient and heat treated for corrosion resistance, long wear life, etc.

This dissertation presents information on the effects of heat treatment on bearing steels, specifically UNS 42670 (Pyrowear 675, or simply P675). P675 is a martensitic stainless steel (MSS) engineered for use in the aerospace industry. Through proprietary heat treatments, P675 can be transformed from a mediocre performing steel to one which can withstand fatigue more than all other steels in its class, while maintaining acceptable corrosion resistance. Here we demonstrate the effects of heat treatments on the new generation of bearing steels to inform and aid steel developers in designing cost-efficient steels that can provide superior corrosion resistance while maintaining required tribological performance.

Samples studied were heat treated using three different methods; High temperature tempering (HTT), Low temperature tempering (LTT), and Carbo-Nitriding (CN). This study was initiated to test the following hypotheses:

- Electrochemical techniques (i.e. anodic polarization (AP), electrochemical impedance spectroscopy (EIS)) will yield faster and more accurate results than conventional corrosion testing methods for screening bearing steels for corrosion behavior.

- HTT samples will have the lowest corrosion resistance due to a larger depletion of chromium from the matrix experienced at the highest tempering temperature which will lead to the highest microgalvanic couple between the carbides and matrix.

- CN will have the highest corrosion resistance from the steels tested due to the addition of nitrogen and encouraged passivation at the oxide/metal interface.

The objective of this dissertation is to understand and explain the implications of heat treatments on the newest and upcoming generation of MSS. A combination of accelerated corrosion testing, modeling, and nanoscale surface analysis was used to determine corrosion mechanism and provide recommendations.

Key results from this study include the following:

- Corrosion performance of P675 is highly dependent on heat treatment where CN outperforms all three heat treatments for corrosion testing, while HTT has the lowest corrosion resistance.

- EIS data was fitted to an equivalent circuit and a mechanism of corrosion attack was proposed for each of the bearing steels studied where HTT experienced general corrosion attack while LTT and CN pitting corrosion.

- SKPFM Volta potential difference (VPD) measurements in an inert environment showed HTT as the thermodynamically most favorable to experience microgalvanic corrosion between the chromium-rich precipitated carbides and the surrounding martensitic matrix, with a measured carbide-matrix VPD of 200 mV, while LTT (150 mV) and CN (90 mV) were less.

- Corrosion propagation was also monitored in real time via in situ AFM and revealed that HTT underwent the most rapid spread of corrosion attack across the sample, while LTT and CN were less affected and showed much more localized, intergranular attack and adjacent to carbides.

- Bulk electrochemical testing results agreed with in situ AFM results, with LTT and CN showing distinct passive regions as compared to HTT, confirming the nanoscale differences in corrosion behavior observed between the steel heat treatments investigated.

- Corrosion rate measurements alone are not adequate to be a predicting factor of bearing performance. The mechanism of corrosion initiation and propagation must be investigated to properly design new bearing steels.

- Based on this work, HTT would be recommended over the other two tempering procedures for use in aerospace bearings where corrosion is not a primary concern. However, when the bearing assembly is prone to corrosion attack, CN is recommended for bearing use due to its high resistance to both corrosion onset and propagation.

In conclusion, this study will allow the United States Armed Forces a new tool (electrochemistry coupled with surface analysis via SPM) to screen candidate bearing

steels for gas turbine engine applications and will give steel developers insight into the effects of heat treatment on the corrosion performance of MSS (i.e P675). This work is a quintessential application of the materials engineering triangle; By varying the heat treatment **(processing)** of the steel, the microstructure **(structure)** of the surface of the steels were changed, thus altering the corrosion behavior **(properties)** and affecting the overall **performance**.

TABLE OF CONTENTS

LIST OF TABLES

LIST OF FIGURES

LIST OF ABBREVIATIONS

ABA	Active brazing alloys
AFM	Atomic force microscope
AP	Anodic polarization
BSE	Backscatter electron
CCT	Cyclic corrosion testing
CIT	Cyclic immersion testing
cm	Centimeter
CN	Carbo-nitriding
CPE	Constant phase element
CPP	Cyclic potentiodynamic polarization
CVN	Charpy V-notch
DC	Direct current
DI	Deionized
EBSD	Electron beam backscatter diffraction
EDS	Energy dispersive spectroscopy
EIS	Electrochemical impedance spectroscopy
EWF	Electronic work function
HPLC	High performance liquid chromatography
HRC	Hardness Rockwell C
HTT	High temperature tempering

Hz	Hertz
J	Joules
kHz	Kilohertz
LTT	Low temperature tempering
MDN	million DN, where DN= [bearing bore (mm)] x [speed (rpm)]
mg	milligram
MHz	Megahertz
mm	millimeter
MPa	Mega Pascal
MSS	Martensitic stainless steel
mV	Millivolts
OCP	Open circuit potential
P675	Pyrowear 675
PN	Plasma nitriding
PPN	Pulse plasma nitriding
PREN	Pitting resistance equivalency number
RCF	Rolling contact fatigue
Rp	Resistance polarization
Rp*	Effective resistance polarization
SCE	Saturated calomel electrode
SPM	Scanning probe microscopy
SE	Secondary Electron
SEM	Scanning electron microscope

SKPFM	Scanning Kelvin probe force microscopy
V	Volt
VC	Vanadium carbide
VP	Volta potential
VPD	Volta potential difference
VIMVAR	Vacuum-induction-melted vacuum-arc-remelted
XRD	X-Ray diffraction
µm	Micrometer

CHAPTER ONE: INTRODUCTION

There has been more than a century of work on alloys for rolling bearings that is elegantly summarized by Zaretsky and Bhadeshia [1-3]. A condensed history of aerospace bearing steels is presented in this dissertation to inform the reader on the progression of these steels. Bearings consist of rolling elements and rings which form the raceways. These rolling elements can consist of balls, cylinders, or barrel shaped metal objects. On engine shafts, bearings must tolerate vibratory stresses, bending moments, high speeds, elevated temperatures, and aggressive lubrication [4].

Background

Bearing Steel Progression

52100 steel was the first alloy that was specifically designed for bearing use and was commercially available. Having a high carbon content (1%), this steel had poor impact toughness [1, 2, 5]. To fix this issue, bearing steel producers began to utilize carburizable steel alloys. The first example of this was 4620 steel, that produced a surface microstructure consisting of tempered martensite, retained austenite, and alloy carbides [5]. The main disadvantage of this steel was its low corrosion resistance [5]. Several factors have been shown to influence corrosion rates in steels: alloying elements, microstructure, carbide properties, and heat treatment [1, 2, 5-10]. The two most commonly used alloying elements that provide corrosion resistance are chromium and nickel [11, 12]. Iron alloys with a chromium content exceeding 12% are considered "stainless" since chromium creates an oxide layer over the surface which passivates the

steel [1, 2]. Other alloying elements known to increase corrosion resistance include nickel, molybdenum, and titanium [1, 13, 14]. Utilizing the principle of a naturally occurring oxide, alloy 440C was created to resist corrosion via a protective film [5]. Molybdenum was also added as an alloying element to inhibit pitting corrosion [1, 13, 14]. While alloy 440C had significant corrosion resistance, it did not perform well in elevated temperatures [1]. T1 steel and M2 steel were the first bearing steels engineered to be used in high temperature [5]. Developed in Europe for jet application in the early 1950's, T1 and M2 steels contained significant amounts of tungsten, 18% and 6% respectively. This prompted the United States to develop the M50 high speed steel which was an attempt to replicate these two steels without the use of tungsten due to tungsten being primarily sourced in the former Soviet Union [5]. Generally, most high speed steels are double-tempered to re-temper any martensite that forms during the first tempering process [5]. These steels experience secondary hardening, and high hardness accomplished by the transformation from retained austenite to martensite during tempering [15, 16]. Over time M50 and M50-NiL, a low-carbon variant for use at elevated temperatures, became the standard in aircraft engine applications in the United States [1, 2, 17]. These high speed steels seemed to address fracture toughness but at the cost of corrosion, as M50 steel has an unacceptable corrosion rate [1, 18, 19]. UNS 42670 (Pyrowear 675, or simply P675), a low-cost, carburizable alloy was developed to have high corrosion resistance and high fracture toughness.

An alternative: P675

In the early 1990's, P675 was developed for commercial use as a bearing steel that had equivalent corrosion resistance to 440C steel whilst maintaining a fracture

toughness higher than that of M50 or M50NiL [20]. Ten main goals were set by Carpenter technologies when attempting to develop the alloy:

(1) The cleanliness of aerospace bearing steels is essential and fatigue life is enhanced by vacuum induction melting and vacuum arc re-melting (VIM-VAR) [21].

(2) Type 440C steel is considered to have sufficient corrosion behavior for bearing steels [19, 20]. Corrosion studies using humidity cone and electrochemical testing have shown P675 as having similar corrosion resistance to 440C [19, 20].

(3) It was essential to create an alloy that could be carburized in order to tailor the alloy case structure processing based on fatigue requirements. Carbide morphology is altered during carburization and heat treatment and control of carbide morphology avoids issues with carbide membraning and necklacing [20].

(4) Within bearing steels, case and core requirements differ and often are in conflict with each other. To meet Charpy V-notch (CVN) and fracture toughness requirements, low carbon content is needed in the core to promote toughness in the material. However, if the carbon content is too little, then excessive core ferrite might be present, introducing other issues [20]. The required level of delta ferrite (5%) is controlled by austenite stabilizers such as nickel and cobalt [20, 22]. Nickel is added to the steel to increase toughness and keep a low-ferrite core. Cobalt is added to raise the temperature at which martensite is formed, thus reducing the retained austenite in the case [20, 22]. Chromium is added to provide significant corrosion protection via a protective oxide film. The level of chromium in P675 (13%) is less than that of 440C (17%) to control the amount of ferrite in the core [20]. Molybdenum and cobalt help with resistance to localized corrosion attack [11, 23, 24]. In steel, vanadium increases wear

resistance to the surface (case) and manganese aids in balancing austenite [20, 25, 26]. However, case-hardening redistributes chromium, giving very different corrosion behavior compared to the core.

(5) Preliminary testing has shown that P675 has good fatigue resistance that is similar to steel SAE 9310; a bearing steel that is used as an industry standard for fatigue resistance [9, 20].

(6) Pfaffenberger and Tarrantini concluded that P675 has superior fatigue resistance compared to bearing steels 440C and M50 [27]. Specifically, P675 showed 6.5 times the experimental life of M50 [20].

(7) When developing P675, the goal was to achieve good wear compatibility with SAE 4340, a steel used in structural components within commercial and military aircraft. To test this, P675 and SAE 8620 (a common steel used for aerospace bearing application) samples individually were coupled with SAE 4340 and subjected to ASTM G83 crossed cylinder wear test. P675 resulted in losing a total volume of 1.37 mm^3 vs 1.72 mm^3 measured for SAE 8620 [20].

(8) Hot hardness refers to the hardness value of the material when it is at elevated temperatures [28]. When tested at an operating temperature of 200°C, an HRC of 60 was obtained at the case, equivalent to that of M50 and M50NiL [20].

(9) In order to support the case with strength, the core of the steel must have significant hardness. An HRC of 35 is the minimum for aerospace case-hardened bearing steels, and tests confirmed that P675 exceeds this requirement by having a HRC of 40 [20].

(10) The Charpy V-notch impact test consists of a pendulum that is dropped to strike a notched specimen of material to determine the amount of energy absorbed by the material during fracture [29]. P675 averaged toughness values of 175 J, as compared to 47.5 J for M50 NiL [20]. Fracture toughness gives information about the ability of a material to resist fracture if a crack already exists [30, 31]. The minimum fracture toughness to prevent failure in bearing service is 44 MPa-m$^{1/2}$ (determined by testing M50 NiL); P675 averaged 165 MPa-m$^{1/2}$ [20].

While P675 is a well-engineered steel, processing modifications are necessary in order to address the ever increasing demands of the aerospace industry. For P675, the Navy has taken a particular interest in heat treatments to better the materials properties. Some of these heat treatments include: high temperature tempering (HTT), low temperature tempering (LTT), plasma nitriding (PN), pulse plasma nitriding (PPN), carbo-nitriding (CN), and any combination thereof. This study will be focused on LTT (316°C), HTT (496°C), and CN as these heat treatments show the most promise, and interest from industry. *This dissertation bridges the gap between processing (i.e. heat treatment) and corrosion behavior, by providing information on the effects of heat treatment on the localized corrosion behavior of martensitic P675 steel with three different heat treatments; HTT, LTT, and CN.*

Necessary Processing

Case-hardening consists of hardening the surface of a metal in order to increase hardness on the surface [32]. This method of surface hardening is especially advantageous with bearing steels due to the introduction of compressive stresses [1]. Compressive stresses found on the surface allow the bearings to perform under higher

loads and higher rotational speeds [10]. Carburization is a diffusion driven form of case-hardening during which carbon is introduced to the surface of a low carbon steel yielding a martensitic structure [1, 33]. The aforementioned stresses initiate during the quenching process that follows carburization. Specifically, the stresses are a direct result of the austenite transforming into martensite and this expansion of the case is constrained by the core, thus leading to the compressive stresses [10]. A steel with an initial carbon content of 0.2% will achieve a content as high as 1% carbon at the carburized layer [33]. Carbides develop as a result of carburization and are compounds composed of carbon and a neighboring alloying element [34]. Significant work has been done to characterize carbides found in high alloy steels by Hetzner and Geertruyden [5]. Through the use of metallography, X-ray diffraction (XRD), and electron beam backscattered diffraction (EBSD) M_7C_3 (orthorhombic) and $M_{23}C_6$ (face-centered cubic) were determined to be the primary carbides found in P675 [5, 10]. Because carbon content decreases for P675 as a function of depth within the steel, M_7C_3 is found more readily at the surface, whereas $M_{23}C_6$ is more abundant deeper within the steel [5]. Generally, coarse carbides are associated with poor fatigue performance. and rolling contact fatigue testing shows that carbides contribute to premature fatigue spalling, yet the mechanism of failure is still not clear [1, 35, 36]. *Carbides are of interest to the work because of its abundance in the steels studied, as well as its detrimental effects on fatigue performance.*

Nitriding is a heat treatment applied to bearing steels which introduces nitrogen to the surface and penetrates to a certain depth (based on time, temperature, and atmosphere composition) referred to as the case [1, 7, 9, 33]. This acts as any other case in that it creates a series of compressive residual stresses just beneath the hardened layer [37].

When the solubility limit is reached, nitrides are precipitated to the grain boundaries. This in turn makes dislocations difficult to navigate and ultimately increases hardness. The nitrogen interacts with steel and other elements to form compounds at the surface. Carbo-nitriding (CN) is a process of introducing both carbon and nitrogen into the surface of a metal with the effect of producing a case hardened metal [7]. CN has been seen to improve corrosion resistance significantly [19, 33]. Common steel alloying elements such as molybdenum, chromium, and vanadium tend to form nitrides [33, 37]. With P675-CN samples received, targeted case depth ranges from 750-1250 µm [9].

Problem

Convention Corrosion Analysis

Salt fog testing, developed approximately a century ago, is widely accepted as a fundamental type of corrosion testing [38]. Many aerospace standards include it as a requirement for assessment of corrosion susceptibility [38, 39]. This testing method is difficult to quantify and inaccurate to the real behavior of materials in use [40-43]. Additionally, the testing itself is very time consuming; with a range of exposure from 2-1000 hours [38, 39]. Testing consists of samples being placed in a temperature-controlled chamber where a salt-containing solution (5% NaCl by weight) is sprayed, at 35°C, as a very fine fog mist over the samples. This corrosive mist is continuous during the entire test causing samples to constantly remain wet. Subsequently, this causes the samples to continuously undergo corrosion. Ultimately, samples are rated by recording the number of hours to reach a qualitative aesthetic level of surface rusting and/or appearance. One main issue of this type of testing is that the surface of the test coupons are constantly wet, with no cyclic drying, which is rare in normal usage conditions. This hinders the

formation of protective oxide coatings for some materials. Also, the international standard (ISO 9227) for the test states that salt spray tests are suitable only as quality control tests for analysis of discontinuities, pores, and damage in paint or metallic coatings [39].

Cyclic immersion testing (CIT) or cyclic corrosion testing (CCT) is a relatively recent testing method that was developed mainly for the automotive industry. CCT attempts to accelerate corrosion conditions and replicate the corrosion that materials undergo in real world applications. Testing duration can range significantly, but 48 hours is the minimum for most aerospace standards. CCT tests expose specimens to a series of different environments in a repetitive cycle. Simple cyclic testing methods such as prohesion may consist of cycling between salt fog and dry conditions. More sophisticated automotive methods call for multistep cycles that may incorporate immersion, humidity, condensation, along with salt fog and dry-off. The most popular test method utilizes a corrosive environment with dry-off testing, as this is accepted as the most representative testing method. A dry-off environment may be achieved in an open laboratory or inside a chamber. The area should be maintained with enough air circulation to avoid pooling and to allow sufficient drying of the material. A drawback of this type of testing is the vagueness of the term "sufficient drying." Currently, there is disagreement on whether a specimen should be considered dry when the surface is dry (via air drying), or when the specimen has dried thoroughly (via a heating element for a predetermined period of time). This issue becomes more significant as testing time increases because as corrosion products build up, the material requires a longer time to achieve "drying." The lack of proper drying may lead to an inaccurate corrosion mechanism and subsequently makes

CCT an ineffective method of testing. *Both CCT and salt fog testing provide only a qualitative ranking amongst steels and do not yield fundamental corrosion initiation or kinetics information essential in determining corrosion mechanisms.*

<u>Knowledge Gap: Corrosion Behavior of Bearing Steels</u>

Previous work on the microstructure of bearing steels is primarily concerned with heat treatment and post wear test failure [7, 9, 44-52]. There is a small amount of research done on bearing steel microstructure and its effects on corrosion behavior [53-57]. While it is generally assumed that localized corrosion is the predominant mechanism observed in corrosion-resistant bearing steels due to their stainless nature, general corrosion is also a concern [1, 2]. The primary mechanism of corrosion attack has not been studied with this generation of martensitic bearing steels. Attempts to predict localized corrosion behavior of stainless steels have been made via pitting resistance equivalency number (PREN) calculations [58]. PREN is an empirical metric for predicting corrosion resistance based solely on composition [58]. In preliminary testing conducted, the PREN were evaluated and did not correlate with measured corrosion rate [19]. *For the next generation of bearing steels currently in development, the effects of heat treating on corrosion behavior are not well determined and there is a need for more thorough study [1, 6-9]. This dissertation addresses this issue by studying the effect of heat treatment on microstructure and the resulting impact of corrosion behavior of P675.*

Motivation

Contemporary bearing steel improvement is driven in part by the demands of the aerospace industry. Gas-turbine engines require that the bearings be able to withstand higher operating speeds, temperatures, greater impact strength, and a resistance to

corrosive environments [1, 35]. Unanticipated failures through corrosion are a concern in aerospace applications, particularly those operating in marine environments [7]. Such failures have precedent, with corrosion-related bearing failure being observed in both planes and helicopters [59, 60]. One survey of aerospace bearing failures found that 11.7% of failures were due to corrosion [60]. Localized corrosion is the predominant form of corrosion observed in bearing steels [1, 7]. This behavior is attributed to the "stainless" nature of most bearing steels. Chromium and iron alloys with a chromium content exceeding 12% are considered "stainless" since chromium creates an oxide layer over the surface which passivates the steel [1, 2]. This oxide can and will break over time, resulting in pits or holes in the oxide layer. *Localized pitting corrosion, experienced frequently with bearing steels, can lead to complete mechanical failure [11, 12].*

The performance required is often in conflict with materials properties and optimization requires compromise. For example, high corrosion resistance typically will result in decreased hardness due to the relatively soft nature of corrosion resistant alloying elements (i.e. chromium, nickel, etc.). This study gives insight into the correlation between heat treatment and corrosion behavior of bearing steels. By possessing a holistic knowledge of bearing steels microstructure/property relationship, informed decisions for materials selection and further research can be made. *There is ample motivation to design superior steels: in addition to safety concerns, bearing longevity also offers economic incentives in reduced maintenance and repair costs [7, 8, 61].*

Scientific Impact

Current research of bearing steels is focused towards mechanical and wear behavior of steels with little to no specific assessment of corrosion susceptibility [7, 9, 44, 46, 49]. This dissertation is a comprehensive collection of electrochemical testing data providing localized corrosion rate information, and in-depth microstructural analysis pre and post corrosion to give insight into how corrosion evolves. This newly acquired data and interpretation is a valuable tool for any industry dealing with alloy development, machines and gears, aerospace bearings, and failure analysis amongst others. This was accomplished by: *(1) rapidly assessing localized corrosion behavior by conducting accelerated corrosion testing via electrochemical methods, (2) determining the microstructural influence on corrosion mechanism by correlating electrochemical testing data with microstructural characterization via scanning electron microscope/energy dispersive spectroscopy and scanning probe microscopy techniques, (3) providing an assessment of the effects of heat treatment on corrosion behavior of MSS with newly acquired data and results of aforementioned methods.*

Dissertation Organization

Chapter two describes how steel samples were tested for corrosion behavior using accelerated electrochemical techniques and ranked based on measured corrosion rate. In Chapter three fitting parameters were extracted from time-dependent EIS data and coupled with visual observation pre and post-testing. Chapter four describes how SKPFM was used to characterize braze samples (where surface features were larger and more pronounced) to develop the skill and knowledge required to use this technique effectively. This same technique, along with *in-situ* AFM, was utilized in Chapter five to

investigate the surface of the P675 bearing samples, monitor corrosion propagation in real time and verify the aforementioned corrosion mechanisms proposed. Chapter six summarizes all of the efforts and conclusions of the dissertation along with recommendations based on findings. Chapter seven provides some suggestions on future work and some possible avenues to explore for the next steps of this research.

References

1. Bhadeshia, H. K. D. H. "Steels for bearings." *Progress in Materials Science* 57.2 (2012): 268-435.

2. Zaretsky, Erwin V. "Rolling bearing steels–a technical and historical perspective." *Materials Science and Technology* 28.1 (2012): 58-69.

3. Zaretsky, Erwin V. "Selection of rolling-element bearing steels for long-life applications." *Effect of Steel Manufacturing Processes on the Quality of Bearing Steels*. ASTM International, 1988.

4. Davies, D. P. "Gear materials in helicopter transmissions." *Metals and Materials* 2.6 (1986): 342-347.

5. Hetzner, Dennis W. and William Van Geertruyden. "Crystallography and metallography of carbides in high alloy steels." *Materials Characterization* 59.7 (2008): 825-841.

6. Ragen, Mark A., Donald L. Anthony, and Ronald F. Spitzer. "A comparison of the mechanical and physical properties of contemporary and new alloys for aerospace bearing applications." *Bearing Steel Technology*. ASTM International, 2002.

7. Trivedi, Hitesh K. and Monahan, Ray, "Low Temperature Plasma Nitriding of Pyrowear 675." *Bearing steel Technologies: 10th Volume, Advances in Steel Technologies for Rolling Bearings, STP 1580*, John M. Beswick, Ed., pp 444-464, doi:10.1520/STP158020140062 ASTM International: West Conshocken, PA, USA, 2015

8. Hurley, Michael F., et al. "Corrosion assessment and characterization of aerospace-bearing steels in seawater and ester-based lubricants." *Corrosion* 68.7 (2012): 645-661.

9. Trivedi, Hitesh K., Otto, Frederick, McCoy, Bryan, Bhattacharya, Rabi S., Piazza, Timothy, "Heat Treatment Process for Martensitic Stainless Steel Pyrowear 675 for Improved Corrosion Resistance." *Bearing Steel Technologies: 10th Volume,*

Advances in Steel Technologies for Rolling Bearings, STP 1580; John M. Beswick, Ed., pp 465-484, doi:10.1520/STP158020140061, ASTM International: West Conshocken, PA 2015

10. Klecka, Michael A., Ghatu Subhash, and Nagaraj K. Arakere. "Microstructure–property relationships in M50-NiL and P675 case-hardened bearing steels." *Tribology Transactions* 56.6 (2013): 1046-1059.

11. Jones, D. A. "The technology and evaluation of corrosion." *Principles and Prevention of Corrosion (2nd Edition), Upper Saddle River, NJ. Prentice-Hall* (1996): 3-4.

12. Uhlig, Herbert H. *Uhlig's corrosion handbook*. Vol. 51. John Wiley & Sons, 2011.

13. Mottu, N., et al. "Structure and composition effects on pitting corrosion resistance of austenitic stainless steel after molybdenum ion implantation." *Surface and Coatings Technology* 200.7 (2005): 2131-2136.

14. Mesquita, T. J., et al. "Lean duplex stainless steels—The role of molybdenum in pitting corrosion of concrete reinforcement studied with industrial and laboratory castings." *Materials Chemistry and Physics* 132.2-3 (2012): 967-972.

15. Goldschmidt, H. J. "The structure of carbides in alloy steels." *Journal of the Iron and Steel Institute* 160 (1948): 345.

16. Goldschmidt, H. J. "The structure of carbides in alloy steels. 2. Carbide formation in high-speed steels." *Journal of the Iron and Steel Institute* 170.3 (1952): 189.

17. Zaretsky, Erwin V. "Bearing and gear steels for aerospace applications." NASA Technical Memorandum 102529 (1990).

18. Popgoshev, D., and R. Valori. "Rolling contact fatigue evaluation of advanced bearing steels." *Rolling Contact Fatigue Testing of Bearing Steels*. ASTM International, 1982.

19. Kvryan, A., Faulkner, E., Lysne, D., Carter, N., Acharya, S., Rafla, V., Trivedi, H. K., and Hurley, M. F., "Electrochemical Corrosion Test Methods for Rapid Assessment of Aerospace Bearing Steel Performance," *Bearing Steel Technologies: 11th Volume, Progress in Steel Technologies and Bearing Steel Quality Assurance, ASTM STP1600*, J. M. Beswick, Ed., ASTM International, West Conshohocken, PA, 2017, pp. 466–486, http://dx.doi.org/10.1520/STP1600201601503

20. Wert, David E. "Development of a carburizing stainless steel alloy." *Advanced Materials and Processes* 145.6 (1994): 89-91.

21. Bamberger, E. N. "Bearing Design—Historical Aspects, Present Technology and Future Problems." *ASME Century* 2 (1980): 1-46.

22. Callister, William D., and David G. Rethwisch. *Materials science and engineering: an introduction*. Vol. 7. New York: John Wiley & Sons, 2007.

23. Peissl, S., et al. "Influence of chromium, molybdenum and cobalt on the corrosion behaviour of high carbon steels in dependence of heat treatment." *Materials and Corrosion* 57.10 (2006): 759-765.

24. Olsson, C-OA, and D. Landolt. "Passive films on stainless steels—chemistry, structure and growth." *Electrochimica Acta* 48.9 (2003): 1093-1104.

25. Kim, Chang Kyu, et al. "Effects of alloying elements on microstructure, hardness, and fracture toughness of centrifugally cast high-speed steel rolls." *Metallurgical and Materials Transactions A* 36.1 (2005): 87-97.

26. Choudhury, Alok. "State of the art of superalloy production for aerospace and other application using VIM/VAR or VIM/ESR." *ISIJ International* 32.5 (1992): 563-574.

27. Pfaffenberger, E., and Tarrantini, P. "High temperature corrosion resistant bearing steel development." *29th Joint Propulsion Conference and Exhibit*. 1993.

28. O'Neill, Hugh. *Hardness Measurement of Metals and Alloys*. Chapman & Hall, 1967.

29. Meyers, Marc André, and Krishan Kumar Chawla. *Mechanical Behavior of Materials*. Cambridge university press, 2008.

30. Hertzberg, Richard W. "Deformation and fracture mechanics of engineering materials." (1989).

31. Anderson, Ted L. *Fracture Mechanics: Fundamentals and Applications*. CRC press, 2017.

32. Smallman, R.E. and Ngan, A. H. W. *Physical Metallurgy and Advanced Materials*. Elsevier Science & Technology, 2007.

33. Schneider, M. J., Chatterjee, M.S., and The Timken Company "Introduction to surface hardening of steels." *ASM Handbook, Steel Heat-Treating Fundamentals and Processes* 4 (2013).

34. Godec, Matjaž, et al. "Characterization of the carbides and the martensite phase in powder-metallurgy high-speed steel." *Materials Characterization* 61.4 (2010): 452-458.

35. Ebert, Franz-Josef. "An overview of performance characteristics, experiences and trends of aerospace engine bearings technologies." *Chinese Journal of Aeronautics* 20.4 (2007): 378-384.

36. Parker, Richard Jay, and Eric N. Bamberger. "Effect of carbide distribution on rolling-element fatigue life of AMS 5749." in *NASA Technical Paper* (1983).

37. Ooi, Steve, and Bhadeshia HKDH. "Duplex hardening of steels for aeroengine bearings." *ISIJ International* 52.11 (2012): 1927-1934.

38. ASTM, B. "117, Standard Practice for Operating Salt Spray (Fog) Apparatus." *ASTM International* (2011).

39. ISO, EN. "9227: 2012 Corrosion tests in artificial atmospheres-Salt spray tests." *International Organization for Standardization, ISO* (2012).

40. Skerry, B. et al. "Environmental and electrochemical test methods for the evaluation of protective organic coatings." *Journal of Coatings Technology, 60,* 765 (1988).

41. Appleman, B. R. "Cyclic accelerated testing: prospects for improved coating performance evaluation." *Journal of Protective Coating Linings* 6.11 (1989): 71-9.

42. Townsend, H. E. "Development of an improved laboratory corrosion test by the automotive and steel industries." *Proceedings of the 4th Annual ESD Advanced Coating Conference, Dearborn, USA*. 1994.

43. LeBozec, N., N. Blandin, and D. Thierry. "Accelerated corrosion tests in the automotive industry: a comparison of the performance towards cosmetic corrosion." *Materials and Corrosion* 59.11 (2008): 889-894.

44. Trivedi, Hitesh K., David T. Gerardi, and Lewis Rosado. "Evaluation of fatigue and wear characteristics of M50 steel using synthetic ester turbine engine lubricants—Part 1." *Wear*185.1-2 (1995): 111-117.

45. Stachowiak, Arkadiusz, Przemysław Tyczewski, and Wiesław Zwierzycki. "The application of wear maps for analyzing the results of research into tribocorrosion." *Wear* 352 (2016): 146-154.

46. Rosado, Lewis, Hitesh K. Trivedi, and David T. Gerardi. "Evaluation of fatigue and wear characteristics of M50 steel using high temperature synthetic turbine engine lubricants—Part II." *Wear* 196.1-2 (1996): 133-140.

47. Rai, Amarendra K., Rabi Bhattacharya, and Hitesh K. Trivedi. "Wear resistant coatings for race land regions of bearing materials." U.S. Patent No. 7,910,217. 22 Mar. 2011.

48. Mukhopadhyay, Prantik, et al. "Microstructural developments during abrasion of M50 bearing steel." *Wear* 315.1-2 (2014): 31-37.

49. Gerardi, D. T., H. K. Trivedi, and L. Rosado. "Evaluation of fatigue and wear characteristics of M50 steel using MIL-L-7808K." *International Journal of Fatigue* 18.3 (1996): 191-196.

50. Dalmau, A., et al. "Tribocorrosion behavior of new martensitic stainless steels in sodium chloride solution." *Wear* 368 (2016): 146-155.

51. Celis, J-P., P. Ponthiaux, and F. Wenger. "Tribo-corrosion of materials: interplay between chemical, electrochemical, and mechanical reactivity of surfaces." *Wear* 261.9 (2006): 939-946.

52. Adachi, Shinichiro, and Nobuhiro Ueda. "Combined plasma carburizing and nitriding of sprayed AISI 316L steel coating for improved wear resistance." *Surface and Coatings Technology* 259 (2014): 44-49.

53. Nygaard, J. R., et al. "Bearing steel microstructures after aircraft gas turbine engine service." *Materials Science and Technology* 30.15 (2014): 1911-1918.

54. Zhang, Yue, et al. "Influence of microstructure evolution on tribocorrosion of 304SS in artificial seawater." *Corrosion Science* 88 (2014): 423-433.

55. Xing'an, Wang, et al. "Effect of rare earth addition on microstructure and corrosion behavior of plasma nitrocarburized M50NiL steel." *Journal of Rare Earths* 34.11 (2016): 1148-1155.

56. Vignal, V., et al. "Influence of the microstructure on the corrosion behaviour of low-carbon martensitic stainless steel after tempering treatment." *Corrosion Science* 85 (2014): 42-51.

57. Anantha, Krishnan H., et al. "Correlative microstructure analysis and in situ corrosion study of AISI 420 martensitic stainless steel for plastic molding applications." *Journal of the Electrochemical Society* 164.4 (2017): C85-C93

58. Sedriks, A.J., *Corrosion of stainless steel, 2. Edition*. United States: 1996.

59. Budinski, Michael K. "Failure analysis of a bearing in a helicopter turbine engine due to electrical discharge damage." *Case Studies in Engineering Failure Analysis* 2.2 (2014): 127-137.

60. Davies, D. P., S. L. Jenkins, and F. R. Belben. "Survey of fatigue failures in helicopter components and some lessons learnt." *Engineering Failure Analysis* 32 (2013): 134-151.

61. Yagita, Kazuhiro, and Chikara OHKI. "Plasma nitriding treatment of high alloy steel for bearing components." *NTN Technical Review* 78 (2010).

CHAPTER TWO: ELECTROCHEMICAL CORROSION TEST METHODS FOR

RAPID ASSESSMENT OF AEROSPACE BEARING STEEL PERFORMANCE

This chapter is published by ASTM International in the book *Bearing Steel Technologies: 11th Volume, Advances in Steel Technologies for Rolling Bearings*.

Electrochemical Corrosion Test Methods for Rapid Assessment of Aerospace Bearing Steel Performance

Armen Kvryan[a]

Emma Faulkner[a]

Drew Lysne[a]

Nicholas Carter[a]

Sanjeev Acharya[a]

Veronica Rafla[a]

Hitesh K. Trivedi[b]

Michael F Hurley[a]

[a] Micron School of Materials Science & Engineering, Boise State University, Boise, ID 83725-2090

b UES Inc, Dayton, OH 45432

Author Roles

Author Contributions: Armen Kvryan, Michael F. Hurley, Drew Lysne, Veronica Rafla, and Sanjeev Acharya conceived and designed the experiments; Armen Kvryan and Nicholas Carter performed the experiments; Armen Kvryan, Emma Faulkner and Michael F. Hurley analyzed the data; Hitesh K. Trivedi contributed reagents, materials and analysis tools. All authors contributed to writing the paper.

Abstract

High-performance mechanical systems (bearings and gears) in advanced gas turbine engines are required to operate at ever increasing operating speeds, temperatures, and loads. Premature failure by corrosion pitting is a major concern in aerospace systems operating in marine environments. To effectively assess the corrosion resistance of candidate heat treatments, a rapid screening test is needed. Electrochemical corrosion testing was performed to rank the relative performance of conventional bearing steels including 440C, American Iron and Steel Institute vacuum induction melting vacuum arc remelting 52100, M50, and M50NiL.Other steels in this study include Pyrowear 675, T15, CSS-42L, Cronidur 30, XD15N, and steels with various heat treatments. Existing corrosion testing methods such as the ASTM standards ASTM B117, *Standard Practice for Operating Salt Spray (Fog) Apparatus*, ASTM G31, *Standard Guide for Laboratory Immersion Corrosion Testing of Metals*, and ASTM G5, *Standard Reference Test Method for Making Potentiodynamic Anodic Polarization Measurements*, lack sensitivity or have too much variability to adequately determine differences in corrosion performance among bearing steels with elevated chromium content. Testing for this study utilized anodic polarization scans and electrochemical impedance spectroscopy scans in simulated

synthetic seawater to provide a way to rapidly screen the corrosion resistance. All testing

was conducted in aqueous solutions at the free corrosion potential. Electrochemical

testing in aviation lubricants is ineffective due to the very high solution resistivity.

However, an aqueous solution provided a method to accelerate corrosion initiation that is

similar to the processes that occur in-engine and was determined to be an effective

method to rapidly obtain a relative ranking of corrosion resistance of the bearing steel

variants considered. A ranking of bearing steels was developed, with CSS-42L and 52100

having the highest corrosion rate while the steels 440C, CR30, XD15N, and Pyrowear

675 (CN-A) had the lowest corrosion rates.

Introduction

Bearing steels are a category of low carbon steels that are used for bearings in

mechanical applications. A ball bearing, for example, is comprised of two differently

sized concentric rings with spherical balls between them [1]. The smaller ring is the inner

raceway, and the larger ring is the outer raceway. Steel bearings have a variety of

applications within the aerospace industry, both as rolling elements and raceways of

bearings [1–3]. The geometry of bearings allows the component to support a greater load

than a simple wheel [1]. Given demand for high performance steels for aerospace

applications, it is advantageous to have a comprehensive knowledge of all aspects of

bearing steels. This paper works toward understanding the corrosion properties of bearing

steels. By possessing a robust knowledge of bearing steels, informed decisions for

material selection and further research can be made.

By the early 1900s, steels rich in chromium and carbon were widely used in

bearings [4]. The AISI 52100 steel was created soon after and, along with the

compositionally similar SAE 52100 steel, remains one of the most common bearing steels in use today [1,4]. M50 steel was developed and became commonplace in high-temperature applications [4]. Cronidur 30, a high nitrogen steel, and M50 NiL, a case-hardened variant of M50 (Ni for nickel and L for low carbon content), are also commonly used [2,4].

Contemporary bearing steel improvement is driven in part by the demands of the aerospace industry. Increasing demands on bearing steels for this application require that they be able to withstand higher operating speeds and temperatures, greater impact strength, and a resistance to corrosive environments [1,2]. Unanticipated failures through corrosion are a concern in aerospace applications, particularly those operating in marine environments [5]. Such failures have precedent, with corrosion-related bearing failure being observed in helicopters [6,7]. One survey of aerospace bearing failures found that 11.7 % of failures were due to corrosion [7]. Pitting corrosion is the predominant form of corrosion observed in bearing steels [1,5].

There is ample motivation to design superior steels: In addition to safety concerns, bearing longevity also offers economic incentives in reduced maintenance and repair costs [5,8,9]. Among tested bearing steels, a hierarchy has been observed with regard to corrosion resistance—from greatest corrosion resistance to least: Cronidur 30, 440C, Pyrowear 675 (P675), M50Nil, and M50 [3,5]. Cronidur 30 has superior corrosion resistance compared to 440C, but it has lower fatigue and impact resistance relative to the other steels mentioned [9]. Several factors have been shown to influence corrosion rates in steels: alloying elements, microstructure and carbide properties, and heat treatment [1,3–5,9–12].

Alloying for Corrosion Resistance

Chromium has long been known to prevent corrosion, and alloys with a chromium content exceeding 12% are considered corrosion resistant [1,4]. It is high chromium content that makes stainless steel "stainless"; chromium creates a fine oxide layer over the surface that passivates the steel [1]. The influence of chromium values on corrosion resistance can be seen by considering the relative compositions of the bearing steels previously listed (Table 2.1). M50 has the lowest chromium content, while Cronidur 30 has the highest.

Other alloying elements have been seen to affect corrosion rate [1,13,14]; 440C has a high chromium content and includes molybdenum, which has been proven to inhibit pitting corrosion in saltwater solutions [1,13,14]. The exact mechanism is not well understood, but chromium-enriched molybdenum phases have been viewed at the surface of similar compositions [13]. One possibility is that the presence of $Mo6^+$ at the passivating layer blocks chloride attack across the material, or that molybdenum-rich carbides are insoluble when faced with chlorides and thus block potential pitting sites [14]. Cronidur 30 was developed to include a high nitrogen and chromium content that bolster the overall corrosion resistance of the steel. This also reduces the activity of the nitrogen by forming a secondary phase. A proposed mechanism is that the nitrogen forms compounds at potential pitting sites, thus preventing corrosion [1].

Studies have shown that coarse carbides are associated with poor fatigue performance [1,2]. Therefore, for superior corrosion resistance, a finer microstructure is preferred in bearing steels [1]. Hardened and tempered SAE 52100 has a micro- structure comprised of tempered martensite and small, uniformly dispersed $(Cr,Fe)_3C$ particles

[10]. Due to a low alloying amount relative to more recent bearing steels, and through hardening, SAE 52100 can be expected to have a finer microstructure than case-carburized bearing steels [3]; 440C has a number of large primary carbides due to its relatively high alloying content [10]; and M50 is a martensitic steel, forming carbides that are typically molybdenum, chromium, and vanadium rich [10,15]. M50NiL contains primarily vanadium rich carbides including VC or V_7C_8 [10]. Carbides present in P675 are either $M_{23}C_6$, a globular carbide, or M_7C_3, a rod-like carbide [11]. Cronidur 30 has a finer microstructure compared to 440C, due to its low carbon concentration; XD15N is similar to Cronidur 30 both in composition and its fine microstructure [1].

Heat Treating

Although the relative corrosion behavior of the untreated alloys previously discussed has been investigated, the effects of heat treating on corrosion behavior remain to be studied more thoroughly [1,3,5,9,12]. Several heat treatments were applied to P675 and studied in this work; P675 was treated at a high temperature temper (HTT) of 496°C and a low temperature temper (LTT) of 316°C. Other samples, designated with PN, underwent a duplex treatment: Carburization followed by low-temperature plasma nitriding [3,5]; PPN indicates that pulse plasma nitriding was used. In both PN and PPN, the bearing steels were tempered at HTT condition followed by nitriding treatment. Carbonitrided P675 is designated with CN. Carbonitriding is a process of introducing both carbon and nitrogen into the surface of a metal with the effect of producing a case-hardened metal [5].

Through-hardened bearing steels are those with a consistent hardness through- out the entire material, with the term generally implying a martensitic structure [1]. In some

situations, a greater surface hardness may be required that through hardening cannot provide or that would not be practical due to scaling issues [1]. Case-hardened bearing steels have been treated in such a manner that the exterior of the part has a greater hardness than the interior. This is achieved through carburization where carbon is diffused into the surface, where the higher carbon concentration creates a harder, martensitic steel [1]. A steel with a bulk carbon content of 0.2 % will achieve a carbon content as high as 1 % at the carburized region [16]. This causes a significant difference in hardenability between the case and the core. A hardened surface over the softer interior has the benefit of introducing compressive stresses at the surface, reducing the potential for crack initiation [16].

Nitriding is a heat treatment applied to bearing steels that introduces nitrogen into the surface of the steel [1,5,12,16]. The nitrogen penetrates to a certain depth, again referred to as the case [16]. This acts as any other case in that it creates a series of compressive residual stresses just beneath the hardened layer [15]. The nitrogen interacts with steel and other elements to form compounds at the surface. A higher alloying content will cause a shorter case depth, and nitriding requires greater cycle times than carburizing to achieve a comparable case depth. Nitriding has been seen to improve corrosion resistance in salt spray testing [16]. Common steel alloying elements such as molybdenum, chromium, and vanadium tend to form nitrides [15,16].

Duplex-hardened materials have undergone a twofold heat treatment process: traditional case or through hardening, then a surface nitriding [15,17]. Duplex hardening for bearing steels has been evaluated for mechanical properties, though the corrosion behavior of duplex-hardened steels has not been well documented [5,12,15].

Corrosion Testing

Two methods were used to characterize the corrosion rates: anodic polarization (AP) and electrochemical impedance spectroscopy (EIS). Given the prevalence of pitting as a corrosion mechanism in bearing steels, it is valuable to have an understanding of pitting behavior. This can be measured by the pitting potential or the voltage at which the material begins to pit. The pitting potential can be obtained using AP and analyzing the resulting polarization curve. EIS, alternatively, gives an understanding of the change of corrosion behavior over time [12].

Experimental Details

Material Preparation

Samples used for corrosion testing were cylindrical (9.5 mm in diameter by 12.7 mm long) in shape. These cylinders were subjected to surface heat treatments and thus physical manipulations of the geometry of the samples was not an option. Testing in a standard electrochemical flat cell would not work as it would not form a watertight seal on the sample. In order to achieve a watertight seal with a defined area for electrochemical testing, the following procedure was developed. The first step was to spot-weld an electrical lead from the sample. This was achieved by spot-welding a flat nickel ribbon onto the top of the cylindrical sample and then wrapping the ribbon with heat-shrink tubing. The bottom of the sample was engraved with sample information such as the type of metal and its heat treatment, if applicable. Cylindrical samples were prepared for electrochemical testing by cutting a piece of electrochemical masking tape and punching a hole within the tape with a standard hole punch (diameter 6.6 mm). Once samples were wrapped with the tape, epoxy was poured over the top and bottom of the

sample. The epoxy limited electrolyte exposure to the sample to only the designated area of testing (the hole in the tape) as well as encapsulated the nickel ribbon connections to the sample, which formed a stronger bond to the sample. Images of the sample before and after preparation are shown below in Fig. 2.1.

The sample was placed in a modified flat cell with an extra hole in the body of the cell to allow the cylindrical sample to hang in the electrolyte solution. A saturated calomel electrode fitted with a Luggin probe was used as the reference electrode to ensure good transfer of charge. The Luggin probe is seen in the image of the electrochemical cell used (Fig. 2.2). The counter electrode chosen for this experiment was a platinum mesh as it is inert in this system.

Electrochemical Testing

Electrochemical testing was performed in order to obtain quick, yet accurate, corrosion behavior data [18]. Bio-Logic (Model # SP-300) and Gamry (Model # 1000E) potentiostats were used. Most samples were tested with synthetic seawater (Ricca Chemical Co.) as the electrolyte, according to ASTM D1141, Standard Practice for the Preparation of Substitute Ocean Water [19]. Some steels were also tested in 0.6-M sodium chloride (NaCl) solution to observe the effect of an electrolyte solution on the corrosion behavior of the steels. The two main methods of electrochemical testing used were AP and EIS, which provided corrosion rates and overall behavior of the steels as a function of time. Although it is standard practice in corrosion rate calculations to account for area tested, it should be noted that all corrosion rates were obtained by normalizing current density over the entire surface area that was exposed to the electrolyte solution [20].

<u>Anodic Polarization Testing</u>

Bearing steel samples were polarized anodically, in accordance to ASTM G5,

Standard Reference Test Method for Making Potentiodynamic Anodic Polarization

Measurements [21], to obtain pitting potential and overall corrosion behavior. Data of the

open circuit potential (OCP) was extracted initially, then a scan rate of 0.5 mV/s was

used to polarize the sample starting with -0.1 V versus OCP. AP testing ended when the

potential reached 0.25 V of the initially measured OCP. Each material was tested

multiple times to ensure accuracy and replicability. Parameters including corrosion

current density (i_{corr}), corrosion potential (E_{corr}), and both anodic and cathodic Tafel fit

constants (β_a and β_c, respectively) were determined by using the Stern-Geary model and

fitting software included in the potentiostat software [22]. A corrosion rate was

determined for each sample using this data and the formula shown in Eq 1, where MPY is

mils per year [18].

$$i_{corr}\left(\frac{\mu A}{cm^2}\right) = 0.46 MPY \tag{1}$$

<u>Electrochemical Impedance Spectroscopy Testing</u>

EIS testing was conducted at OCP, or free corrosion potential, over a period of

time (approximately 60 h) with an EIS scan conducted every 2 h for a total of 25 separate

scans on each test sample. A corrosion rate was determined for each EIS scan, yielding

data capturing the evolution of corrosion during the entire exposure period. To calculate

the corrosion rate from each EIS scan, the formula shown in Eq 2 was used [18].

$$i_{corr}(\frac{A}{cm^2}) = \frac{B}{R_p} \ where \ B = \frac{(\beta_a \beta_c)}{(\beta_a + \beta_c)}$$

$$i_{corr}\left(\frac{\mu A}{cm^2}\right) = 0.46 MPY \tag{2}$$

The corrosion rate i_{corr} (A/cm^2) is equal to a constant B divided by the polarization resistance (R_p). The constant B is a function of the anodic and cathodic Tafel slopes (β_a and β_c) near the open circuit. To convert to the corrosion rate, the Tafel slopes were assumed to be the same for all materials and all tests for the samples that underwent EIS testing. The value of R_p was the impedance at low frequency (specifically 10.006 mHz), which is equivalent to a direct current resistance and has been shown to predict overall corrosion behavior [20,23]. As with earlier samples, these samples were tested multiple times to ensure replicability and accuracy of the testing method.

Results and Discussion

Results

AP Testing

AP testing was performed in order to obtain a pitting potential for each steel. This is of particular importance because pitting corrosion is the main method of attack experienced by bearing steels made of stainless steels [12]. Each sample was tested a minimum of three times to ensure replicability within the system. Fig. 2.3 contains three sets of polarization scans from the 52100 steel showing system replicability.

An acceptable deviation of approximately 80 mV is observed for different E_{corr} values of each replicate test. This shows consistency with both the system and sample preparation. Anodically polarizing the samples yielded scans from which data were extracted via modeling and fitting tangent lines to the anodic and cathodic portion of the graph. A representative graph is shown in Fig. 2.4 that illustrates this method.

Parameters such as E_{corr}, i_{corr}, β_a, and β_c were of particular interest because these are linked to overall corrosion behavior [22]. Using these parameters, corrosion rates were determined from AP testing and are shown in Fig. 2.5.

EIS Testing

Electrolyte Solution

EIS testing of bearing steels gave insight into the interfacial reaction between the electrolyte and the steel. The electrolyte chosen is critical in determining a corrosion rate and subsequently a relative ranking. Fig. 2.6 shows comparisons among three steels tested via EIS with two different electrolytes.

For this study, synthetic seawater was chosen as the electrolyte because it replicates the environment that these bearing steels would be exposed to more accurately than 0.6-M NaCl. Details on the differences in corrosion rates are addressed in the discussion section.

Analysis and Corrosion Rate Calculation

A Nyquist plot shows the negative imaginary impedance as a function of real impedance. By modeling the data in a Nyquist plot, to a given circuit, it is possible to extract individual parameters of that circuit, including polarization resistance (R_p) and ohmic resistance. Of special importance was the low-frequency (LF) impedance magnitude (approximately 10 mHz), which has been shown to approximate the R_p value and help forecast the long-term performance of the sample [20,23]. This was the approach taken in this study. Fig. 2.7 is an example of Nyquist plots obtained as a function of time.

To calculate corrosion rates from EIS data, the magnitude of LF impedance was taken to be representative of the Rp. Initially, LF impedance values from all cycles were obtained and corrosion rates were determined. Unfortunately, this made it difficult to provide a quantitative ranking of the steels. Therefore, the LF magnitude impedance values in the approximately 10-h to 40-h span for each test were chosen as the values used to calculate the overall corrosion rate. This reasoning is discussed in greater detail in the discussion section. Using this method, the corrosion rates were calculated and presented in Fig. 2.8. CSS-42L, 52100, and T15 performed the worst, with corrosion rates exceeding 15 mils per year. CR30, XD15N, P675 (CN-A), and 440C performed the best, with corrosion rates below 3 mils per year.

Discussion

Analysis of the AP and EIS data concluded with relative rankings of the steels' corrosion rates. The resulting graph, shown in Fig. 2.9, compares corrosion rates of steels obtained by AP and EIS testing. When comparing the two data sets, a difference is seen in the values for corrosion rates. However, the general trend of steels stays the same and is comparable for qualitative ranking. This trend can also be seen in Fig. 2.10, which compares the two testing methods as a function of OCP.

The data from both methods of electrochemical testing seem to be precise while not necessarily accurate. Due to this type of relationship, the study proceeded by only utilizing one method of testing—EIS. This was chosen due to several reasons. First, EIS simply yielded more conservative values for corrosion rates. This would only return a safer assessment and overall ranking of the steels. Also, a typical EIS scan spanned a little more than two days and consisted of 25 cycles. This produced more data that helped

minimize errors. Finally, EIS has the ability to provide corrosion behavior data as a

function of time, giving insight into how the steel is changing as it corrodes as well as a

better overview of the response of the sample to the system [20].

Low Frequency Impedance

Initially, corrosion rates were determined for EIS testing by obtaining the

magnitude of LF impedance for each cycle and treating that as the R_p value. The graph

shown in Fig. 2.11 was constructed using this method. A general trend for most steels

tested suggests that the corrosion rate increases as time goes on. This could be due to the

nature of how these bearing steels are produced. Most steels evaluated are case-

carburized and have high surface hardness (HRc greater than 62). The case-carburized

steels have a graded alloy composition and microstructure and hence graded hardness

[5,12]. Therefore, once the surface layer is compromised, the sample begins to corrode, at

an accelerated rate, with no protection. However, with the best performing (lowest

corrosion rate) steels, this is not the case. As seen in Fig. 2.11, the steels CR30, XD15N,

P675 (LTT), and P675 (CN-A) not only have generally lower corrosion rates, but they

also have stable corrosion rates.

Although EIS this provides insight into the corrosion behavior of the steels over

time, this makes it difficult to provide a quantitative relative ranking among the steels.

More importantly, from the impedance values obtained at LF, it was evident that the

system usually stabilizes around the 10-h mark and continues the same behavior until the

end of the test. To illustrate this behavior, Fig. 2.12 shows corrosion rates as a function of

time for nine separate EIS tests of P675 (LTT). Therefore, corrosion rates were averaged

between 10-h to 40-h to obtain a single representative corrosion rate

Electrolyte

Bearing steels chosen in this study are primarily used for aviation applications—specifically, military aircraft that might be on an aircraft carrier for months at a time. Initially, two electrolyte solutions were explored: 0.6-M NaCl and synthetic seawater (ASTM D1141 [19]). When testing in 0.6-M NaCl solution, corrosion rates for some of the same steels are exponentially higher while others increase very slightly when compared to synthetic seawater (Fig. 2.6). For example, for CR30, the corrosion rate increases approximately tenfold when switching from synthetic seawater to 0.6-M NaCl. However, for P675 (LTT), the corrosion rate increased well over 100 times. Synthetic seawater has a higher amount of chlorine and a lower pH than 0.6-M NaCl solution and is still less corrosive. This less corrosive behavior is believed to be from the other constituents in the synthetic seawater. Also, the electrolyte solution affects overall ranking among the steels as P675 (LTT) and P675 (HTT1) seem to switch in ranking when the electrolyte is changed. However, because the point of electrochemical testing is to rapidly simulate the in-use environment of the steels, data from the most representative electrolyte are considered to be most accurate. Therefore, basing decisions for material selection solely on electrochemical data must be checked to see if the electrolyte solution is similar to that of its application. For this reason, synthetic seawater was chosen as the electrolyte as it replicates the anticipated environment of the steels most accurately.

Heat Treatment

The bearing steels are subjected to heat treatment based on alloying elements in order to obtain desired properties. For aerospace mechanical system applications, the primary objective of heat treatment is to improve tribological performance in terms of

fatigue life and wear resistance. The effect of heat treatment on corrosion resistance has been given some consideration. Generally, higher annealing temperatures yield lower corrosion resistance as seen in Fig. 2.13.

The P675 alloy with different tempering temperature (LTT and HTT1) showed a significant difference in corrosion behavior. Corrosion rates were averaged from a minimum of eight replicate tests. P675 tempered at low temperature inhibits corrosion and provides good corrosion resistance for a prolonged period of time. Conversely, P675 tempered at a higher temperature has a higher corrosion rate, and the corrosion rate increases at a constant rate as a function of time. This difference in behavior suggests that the P675 (LTT) has a desirable microstructure that protects the material from the electrolyte solution.

Pitting Resistance Equivalency Number

The pitting resistance equivalency number (PREN) is a quick empirical method, based on alloy composition, to determine a pitting resistance ranking among metals. The equation (Eq 3) for calculating the PREN is shown here [24]:

$$PREN = \%Cr + 3.3(\%Mo) + 16(\%N) \text{ (3)}$$

The formula implies that nitrogen has a significant influence on overall pitting resistance. It has generally been thought that higher PRENs correlate to improved resistance. To test this theory, corrosion rates obtained were compared to their respective PRENs. Note that the PRENs were calculated using the median values for each respective steel from Table 2.1. The resulting graph is displayed in Fig. 2.14.

As seen from the graph, there is no correlation between PREN and the corrosion rate for highly alloyed carburized/nitrided steels. Although, generally, PREN values are

used to only compare stainless steels, the data proves that even among those steels PREN is not a valid protocol to design by. CSS42L has a higher PREN than XD15N but has a significantly higher corrosion rate. Therefore, PREN is not a suitable method for ranking pitting behavior of bearing steels. The corrosion rate and corrosion behavior should be verified experimentally.

Conclusions

Bearing steels, with various heat treatments, were successfully electrochemically tested and characterized for corrosion using two independent processes: AP and EIS. A relative quantitative ranking of steels was developed using these two methods.

1. A procedure was developed to successfully prepare cylinder samples for electrochemical testing.

2. Replicability of AP testing was demonstrated by conducting at least three scans on each material tested.

3. A correlation was shown between OCP values and corresponding corrosion rates determined using both electrochemical testing methods.

4. A ranking system of the steels was developed with CSS42L steel having the highest corrosion rate while the steels 440C, CR30, XD15N, and P675 (CN-A) had the lowest corrosion rates.

5. Bearing steels were tested using two different methods of electrochemical testing:

   a. Corrosion rates of steels tested using both AP and EIS testing methods were observed to show validity and precision in both testing methods.

   b. It was determined that EIS testing is superior to that of AP because EIS yielded more conservative (higher) corrosion rates, gave insight to the

corrosion behavior over time, and ultimately contained more scans (more data), which helped minimize errors.

6. A general trend of increasing corrosion rates with time was observed with most steels evaluated. The best-performing steels had stable corrosion rates. This is due to material alloying elements, heat treatment, and the formation of a passive layer.

7. The electrolyte medium used in corrosion testing has a significant effect on the corrosion rate. EIS testing was done in two separate electrolyte mediums: 0.6-M NaCl and synthetic seawater; 0.6-M NaCl resulted in much more damage to the samples and yielded corrosion rates much higher than those in synthetic seawater. This behavior is based on several constituents found in synthetic seawater that act as corrosion inhibitors; 0.6-M NaCl also changed some of the relative rankings of the steels tested.

8. Tempering temperature significantly influences the overall corrosion behavior of P675.

9. Empirical calculations of PRENs were compared to corrosion rates obtained via EIS testing and were determined to be poor predictors of corrosion rates.

References

1. Bhadeshia, H. K. D. H. "Steels for bearings." *Progress in materials science* 57.2 (2012): 268-435.

2. Ebert, Franz-Josef. "An overview of performance characteristics, experiences and trends of aerospace engine bearings technologies." *Chinese journal of aeronautics* 20.4 (2007): 378-384.

3. Ragen, Mark A., Donald L. Anthony, and Ronald F. Spitzer. "A comparison of the mechanical and physical properties of contemporary and new alloys for aerospace bearing applications." *Bearing steel technology*. ASTM International, 2002.

4. Zaretsky, Erwin V. "Rolling bearing steels–a technical and historical perspective." *Materials Science and Technology* 28.1 (2012): 58-69.

5. Trivedi, Hitesh K. and Monahan, Ray, "Low Temperature Plasma Nitriding of Pyrowear 675." *Bearing steel Technologies: 10th Volume, Advances in Steel Technologies for Rolling Bearings, STP 1580*, John M. Beswick, Ed., pp 444-464, doi:10.1520/STP158020140062 ASTM International: West Conshocken, PA, USA, 2015

6. Budinski, Michael K. "Failure analysis of a bearing in a helicopter turbine engine due to electrical discharge damage." *Case Studies in Engineering Failure Analysis* 2.2 (2014): 127-137.

7. Davies, D. P., S. L. Jenkins, and F. R. Belben. "Survey of fatigue failures in helicopter components and some lessons learnt." *Engineering Failure Analysis* 32 (2013): 134-151.

8. Yagita, Kazuhiro, and Chikara Ohki. "Plasma nitriding treatment of high alloy steel for bearing components." *Technical Review* (2010).

9. Hurley, Michael F., et al. "Corrosion assessment and characterization of aerospace-bearing steels in seawater and ester-based lubricants." *Corrosion* 68.7 (2012): 645-661.

10. Hetzner, Dennis W., and William Van Geertruyden. "Crystallography and metallography of carbides in high alloy steels." *Materials Characterization* 59.7 (2008): 825-841.

11. Klecka, Michael A., Ghatu Subhash, and Nagaraj K. Arakere. "Microstructure–property relationships in M50-NiL and P675 case-hardened bearing steels." *Tribology Transactions* 56.6 (2013): 1046-1059.

12. Trivedi, Hitesh K., Otto, Frederick, McCoy, Bryan, Bhattacharya, Rabi S., Piazza, Timothy, "Heat Treatment Process for Martensitic Stainless Steel Pyrowear 675 for Improved Corrosion Resistance." *Bearing Steel Technologies: 10th Volume, Advances in Steel Technologies for Rolling Bearings, STP 1580*; John M. Beswick, Ed., pp 465-484, doi:10.1520/STP158020140061, ASTM International: West Conshocken, PA 2015

13. Mottu, N., et al. "Structure and composition effects on pitting corrosion resistance of austenitic stainless steel after molybdenum ion implantation." *Surface and Coatings Technology* 200.7 (2005): 2131-2136.

14. Mesquita, T. J., et al. "Lean duplex stainless steels—The role of molybdenum in pitting corrosion of concrete reinforcement studied with industrial and laboratory castings." *Materials Chemistry and Physics* 132.2-3 (2012): 967-972.

15. Ooi, Steve, and Bhadeshia HKDH. "Duplex hardening of steels for aeroengine bearings." *ISIJ international* 52.11 (2012): 1927-1934.

16. Schneider, M. J., Chatterjee, M.S., and The Timken Company "Introduction to surface hardening of steels." *ASM Handbook, Steel Heat-Treating Fundamentals and Processes* 4 (2013).

17. Gloeckner, Peter, and Franz-Josef Ebert. "Micro-sliding in high-speed aircraft engine ball bearings." *Tribology Transactions* 53.3 (2010): 369-375.

18. Jones Denny, A. "Principles and prevention of corrosion." *Upper Saddle River, NJ, USA, Pearson-Prentice Hall* (1992).

19. Standard, A. S. T. M. "D1141-98: Standard Practice for the Preparation of Substitute Ocean Water." *ASTM International, West Conshohocken* (2013).

20. Frankel, Gerald S. "Electrochemical techniques in corrosion: status, limitations, and needs." *Journal of Testing and Evaluation* 42.3 (2008): 517-538.

21. American Society for Testing and Materials (Philadelphia, Pennsylvania). "ASTM G5-14: Standard Reference Test Method for Making Potentiodynamic Anodic Polarization Measurements." ASTM, 2014.

22. Stern, Milton, and Al L. Geary. "Electrochemical polarization I. A theoretical analysis of the shape of polarization curves." *Journal of the electrochemical society* 104.1 (1957): 56-63.

23. Scully, J. R., and S. T. Hensley. "Lifetime prediction for organic coatings on steel and a magnesium alloy using electrochemical impedance methods." *Corrosion* 50.9 (1994): 705-716.

24. Schweitzer, Philip A. *Corrosion Engineering Handbook*. CRC, 2007

Figures

(a)   (b)
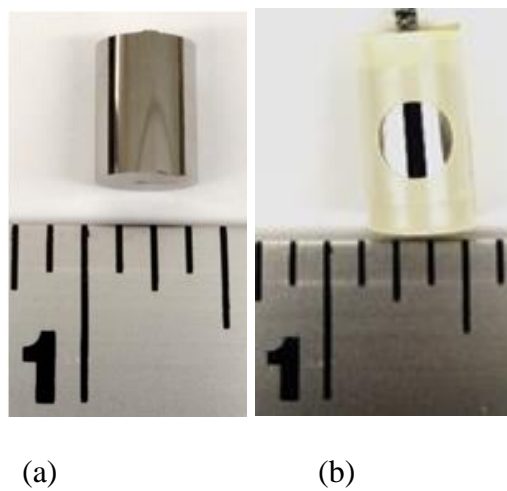
Figure 2.1   Macro image of (a) samples as received and (b) samples after preparation for electrochemical testing.
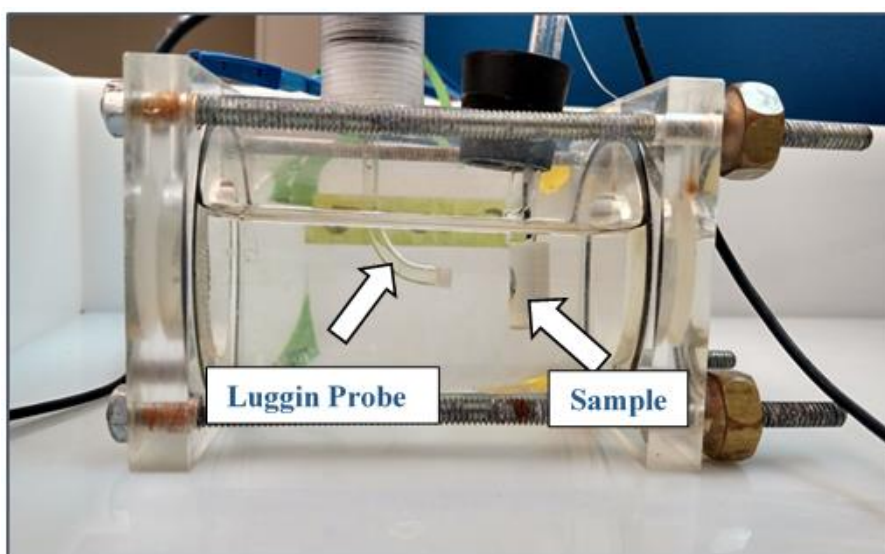
Figure 2.2   Electrochemical test cell for corrosion testing.
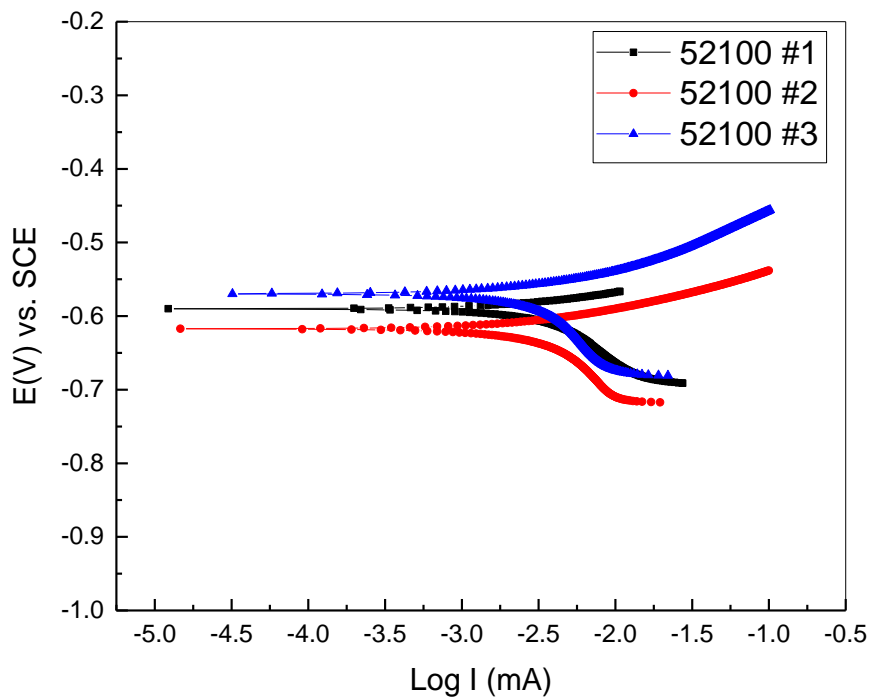
Figure 2.3   A set of three polarization scans of 52100 steel.
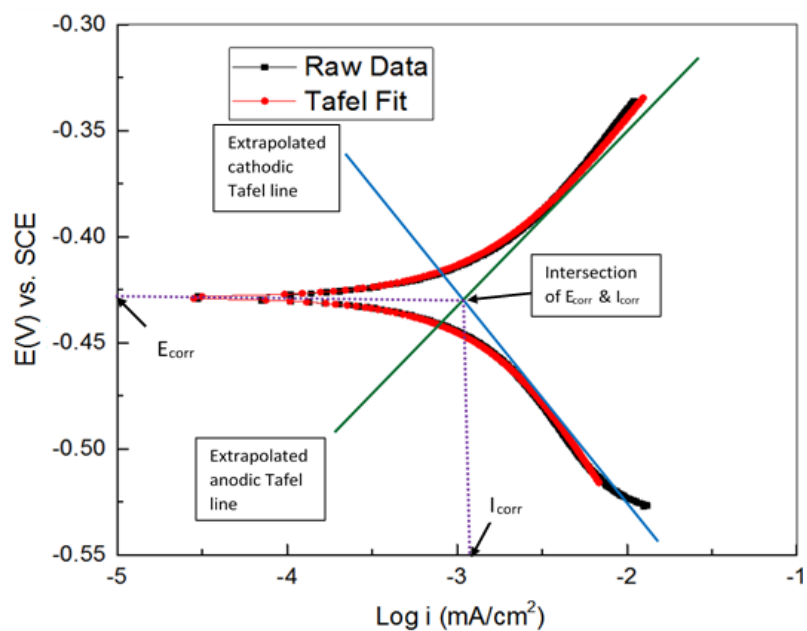
Figure 2.4   Image illustrating Tafel fitting procedure used for this study.
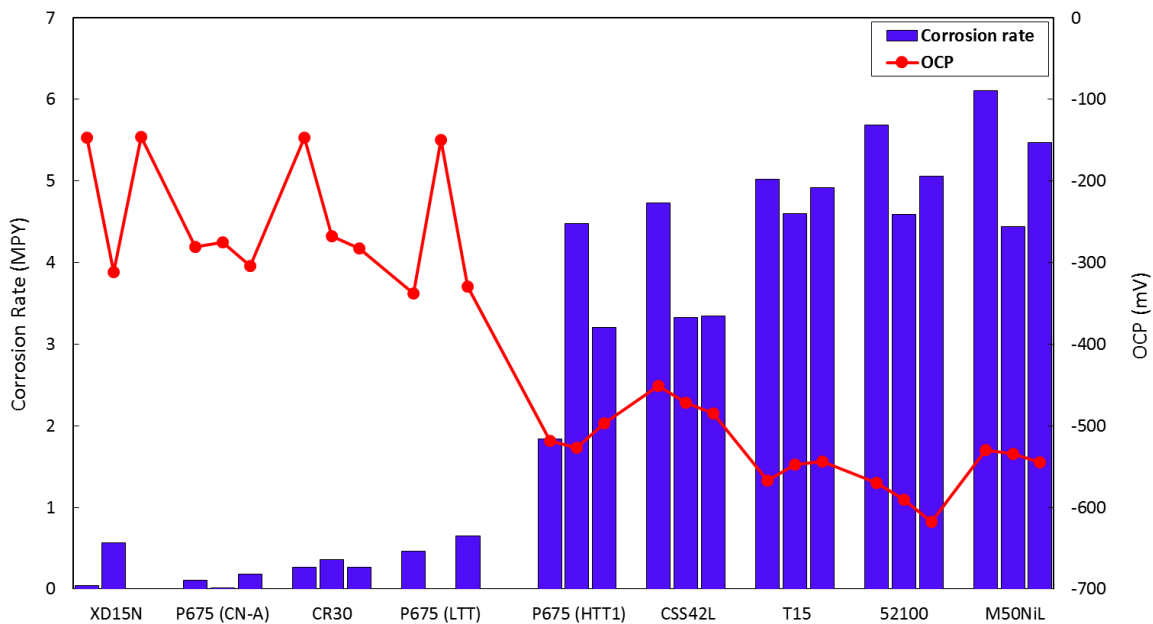
Figure 2.5   **Corrosion rate and open circuit potential (OCP) as a function of each steel tested calculated from anodic polarization (AP) testing.**
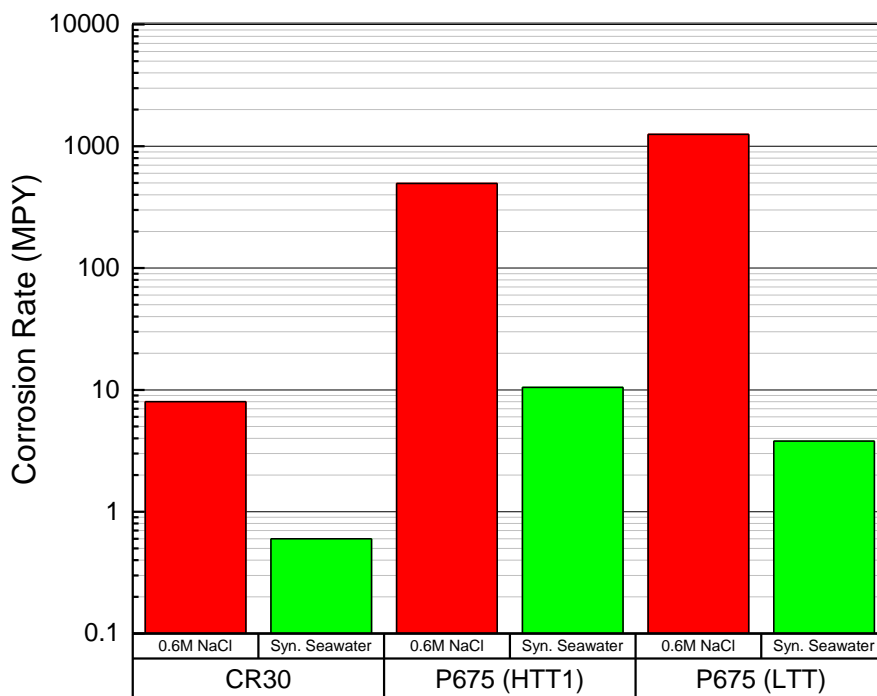
Figure 2.6   **Graph comparing corrosion rates of three different steels tested in 0.6M NaCl and synthetic seawater.**
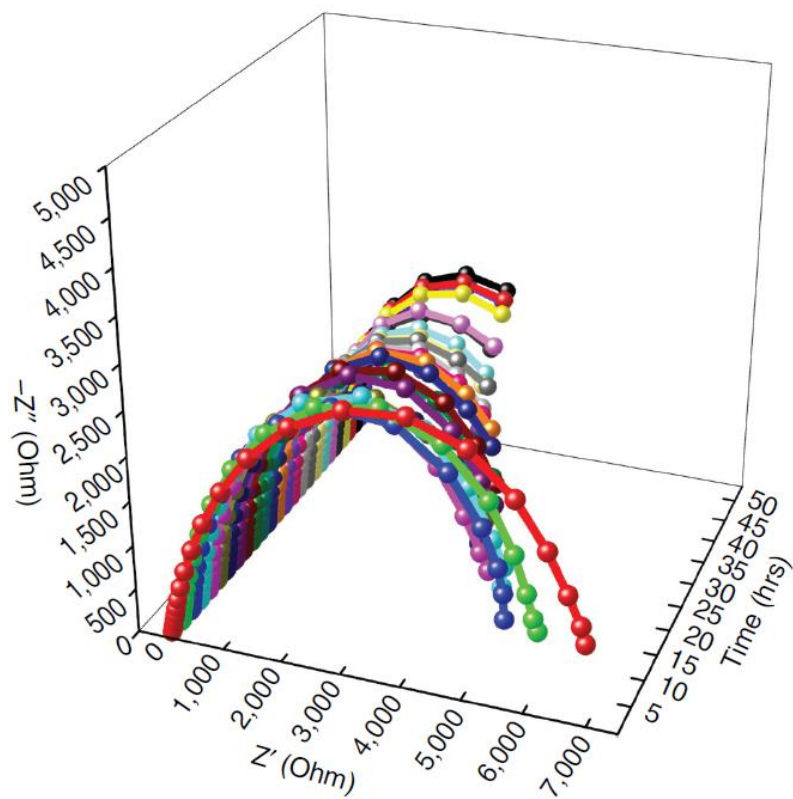
Figure 2.7   3D Nyquist impedance plot as a function of time for T15.
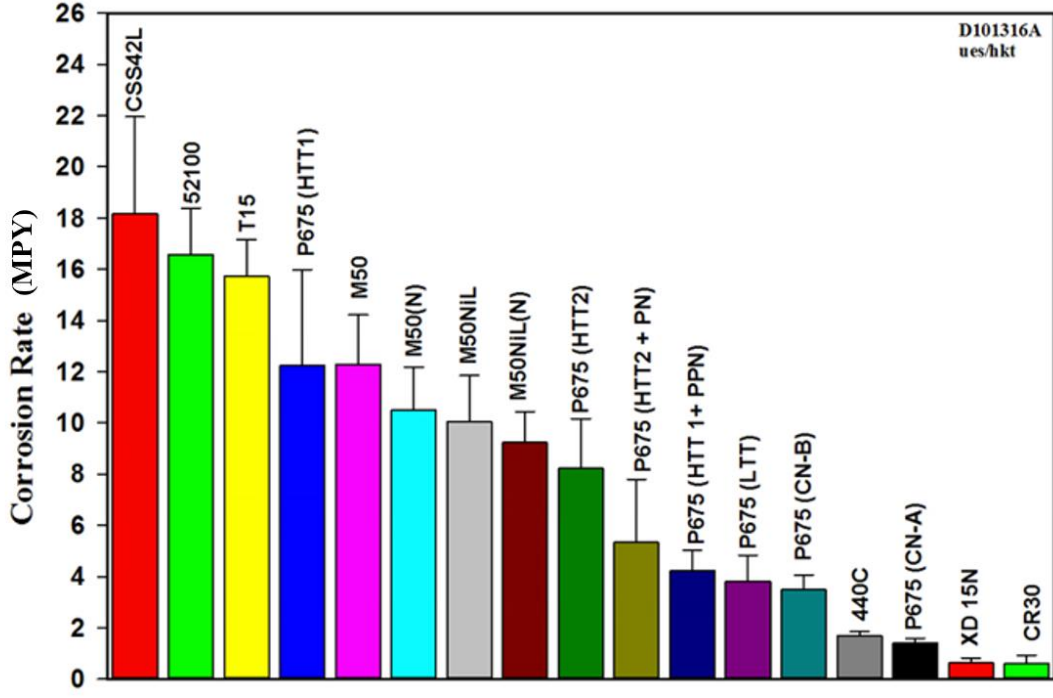
Figure 2.8 **Relative ranking of bearing steels in regards to corrosion rates acquired ~10-40 hours of testing using the EIS method.**
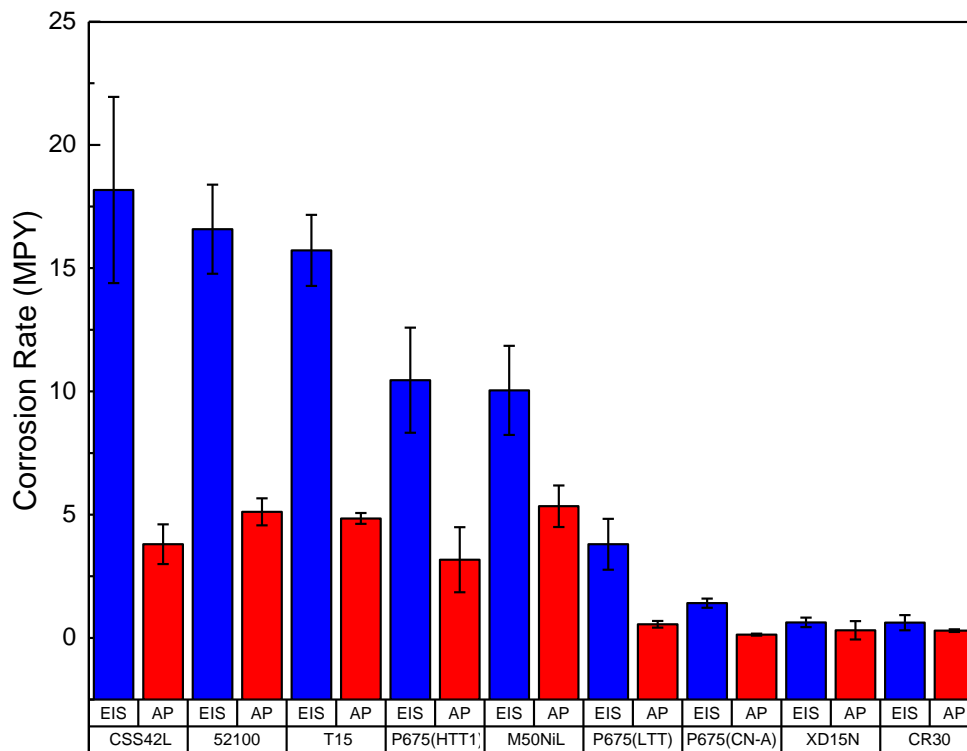
Figure 2.9   Graph comparison of corrosion rates of steels derived from electrochemical impedance spectroscopy (EIS) testing and AP testing.
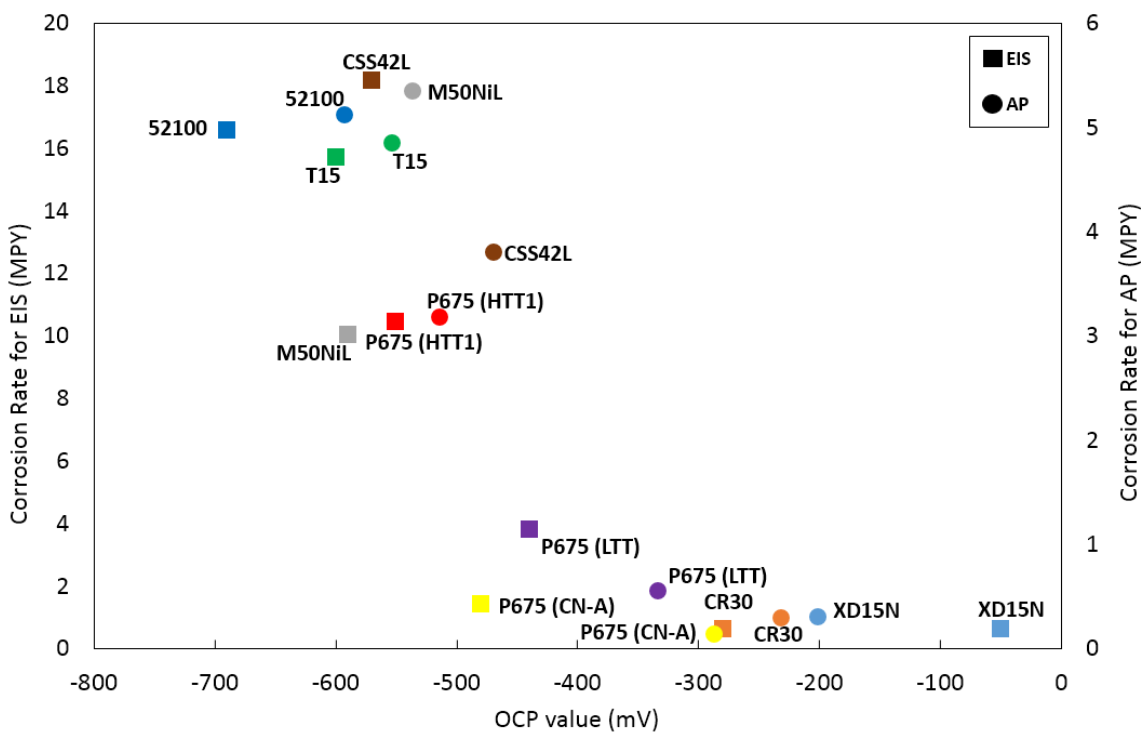
Figure 2.10 **Graph of corrosion rates calculated via EIS (Y1 axis) and AP (Y2 axis) as a function of OCP value.**
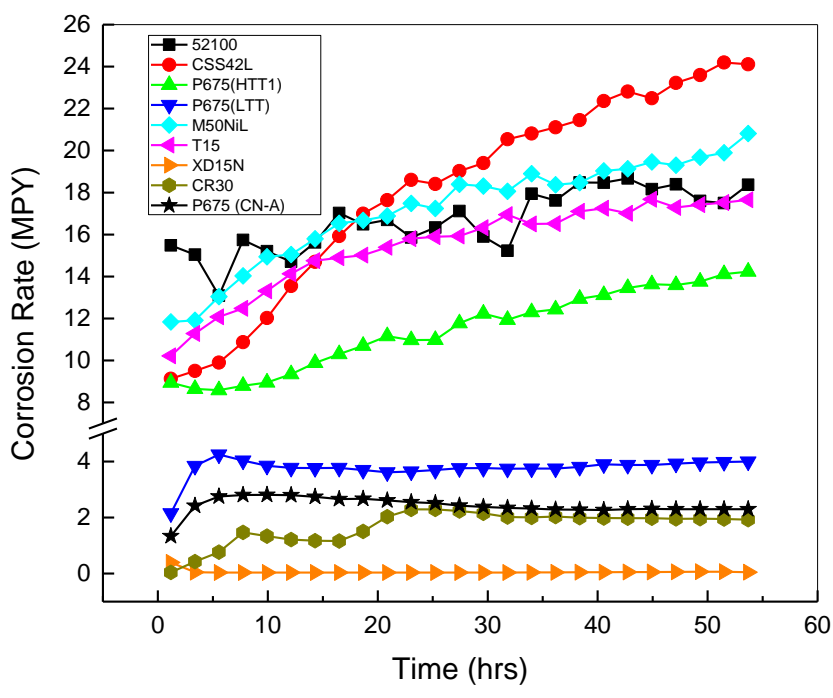
Figure 2.11 **Corrosion rate as a function of time for select steels tested using EIS.**
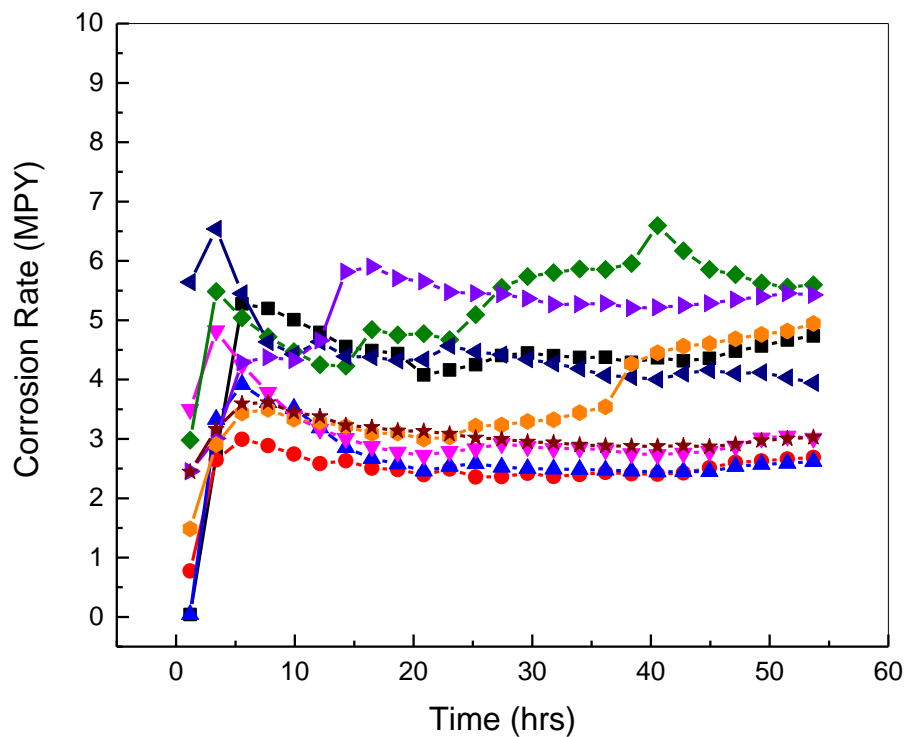
Figure 2.12   Corrosion Rate as a function of time for P675 (LTT) for nine individual EIS tests.
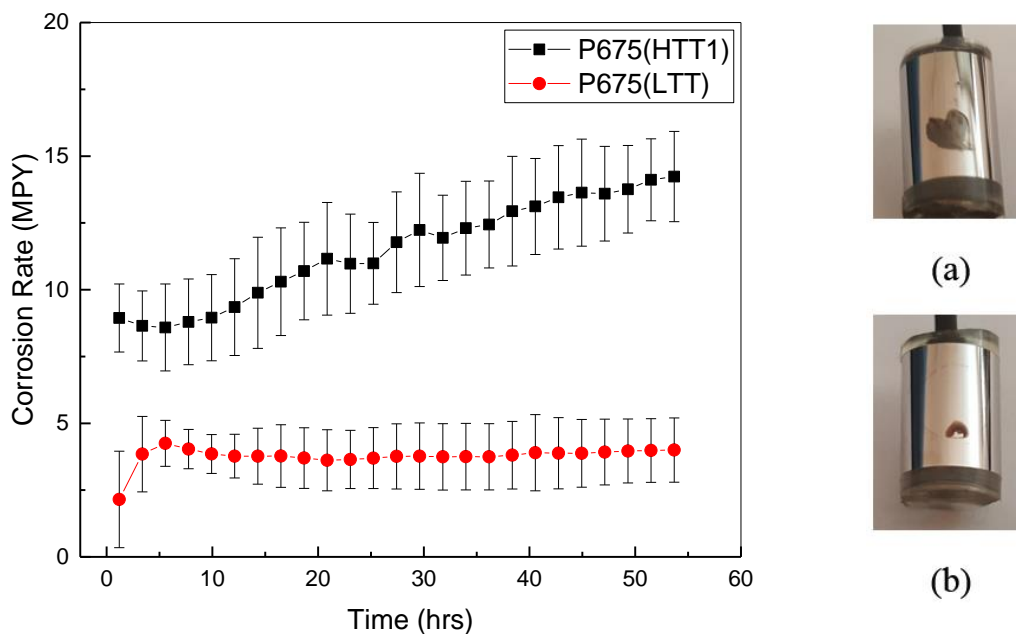
Figure 2.13   Corrosion rate as a function of time for P675 (HTT1) and P675 (LTT). Photograph of corrosion tested samples (a) P675 (HTT1) and (b) P675 (LTT).
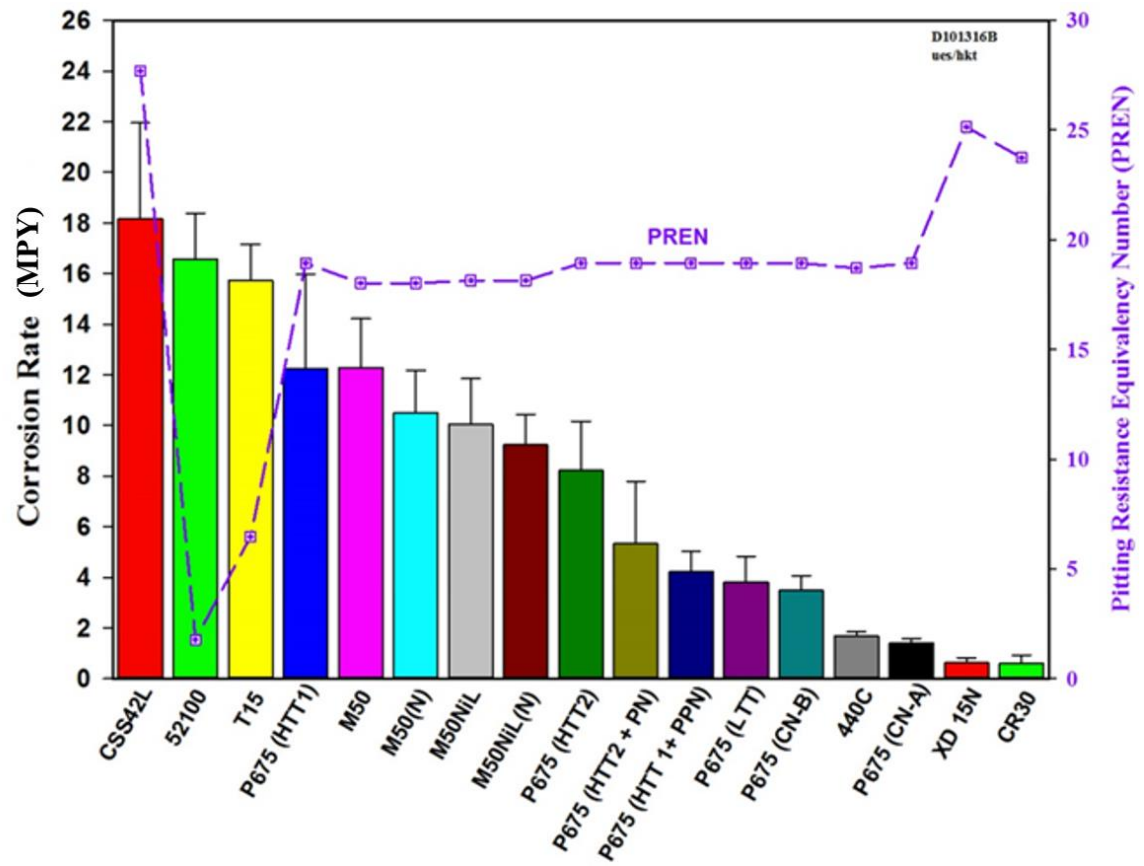
Figure 2.14   Corrosion rate (Y_1 axis) and pitting resistance equivalency number (PREN) (Y_2 axis) as a function of steel.

Tables

Table 2.1   **Compositions of bearing steels (wt. %).**

Composition	C	Mn	Si	Cr	Ni	Mo	V	S	P	Others
AISI 52100	0.95–1.10	0.20–0.50	< 0.36	1.30–1.60	-	-	-	< 0.026	-	Cu: 0.026
SAE 52100	0.97–0.98	0.31–0.38	0.16–0.32	1.39–1.43	< 0.07	< 0.02	-	-	-	Cu: 0.12
M50	0.77–0.85	< 0.35	< 0.25	3.75–4.25	< 0.15	4.00–4.50	0.9–1.1	< 0.015	< 0.015	Cu: < 0.1 W: < 0.25 Co: < 0.25
M50 Nil	0.11–0.15	0.15–0.35	0.10–0.25	4.00–4.25	3.20–3.60	4.00–4.50	1.13–1.33	< 0.015	< 0.015	W: < 0.15 Co: < 0.25
440C	0.95–1.20	< 1.00	0.40	17.0	< 1.00	< 0.75	-	< 0.020	< 0.010	Cu: < 0.50
P675	0.05–0.09	0.50–1.0	0.10–0.70	12.0–14.0	2.0–3.0	1.50–2.50	0.40–0.80	0.003	0.005	Co: 4.0–7.0
Cronidur 30	0.20–.034	0.30–0.60	0.30–0.80	14.50–16.0	< 0.30	0.95–1.10	-	< 0.010	< 0.020	N: 0.36
XD15N	0.37–0.45	< 0.60	< 0.60	15–16.5	< 0.30	1.50–1.90	0.20–0.40	< 0.005	< 0.020	N: 0.16–0.25
T15	1.50–1.60	0.15–0.40	0.15–0.40	3.75–5.0	-	-	4.50–5.25	< 0.30	< 0.30	Co: 4.75–5.25 W: 11.75–13.00
CSS-42L	0.10–0.25	< 1.0	< 1.0	13.0–16.0	1.75–2.75	3.0–5.0	0.40–0.80	< 0.010	< 0.020	Co: 12.5 Nb: 0.02

Note: C = carbon; Mn = manganese; Si = silicon; Cr = chromium; Ni = nickel; Mo = molybdenum; V = vanadium; S = sulfur; P = phosphorus; Cu = copper; W = tungsten; Co = cobalt; N = nitrogen; Nb = niobium

CHAPTER THREE: CORROSION PROPAGATION ON CARBURIZED LOW

CARBON 13CR MARTENSITIC STAINLESS STEELS CONTAINING 2.5Ni-5.5Co-

2Mo-0.6V ENGINEERED FOR AEROSPACE GAS TURBINE ENGINE BEARINGS.

Corrosion Propagation on Carburized Low Carbon 13cr Martensitic Stainless Steels Containing 2.5Ni-5.5Co-2Mo-0.6V Engineered for Aerospace Gas Turbine Engine Bearings

Armen Kvryan[a]

Nicholas Allen Carter[a]

Hitesh K. Trivedi[b]

Michael F. Hurley[a]

[a]Micron School of Materials Science & Engineering, Boise State University, Boise, ID 83725-2090

[b]UES, Inc., Dayton, OH 45432

Author Roles

Author Contributions: Armen Kvryan and Michael F. Hurley conceived and designed the experiments; Armen Kvryan and Nicholas Carter performed the experiments; Armen Kvryan, Nicholas Allen Carter, and Michael F. Hurley analyzed the data; Hitesh K. Trivedi contributed reagents, materials and analysis tools. All authors contributed to writing the paper.

Abstract

Carburizable martensitic stainless steels (MSS) are attractive candidates for bearings due to their high corrosion resistance, high hardness, and high temperature performance. Wear performance in tribo-corrosion applications is strongly influenced by the surrounding environment. Electrochemical testing was used to evaluate three different surface treatments developed for advanced gas-turbine engine bearing applications; low temperature (LTT), high temperature (HTT), and carbo-nitrided (CN). HTT had a higher corrosion rate that increased with time while LTT and CN had lower corrosion rates that were stable over time. Accelerated testing revealed that surface treatment significantly influenced how corrosion propagated, HTT was more uniform, conversely, LTT and CN showed localized attack. Degradation mechanisms developed from electrochemical methods provide rapid insight into long term wear behavior.

Introduction

As aircraft engines operate at greater speeds and temperatures for improved efficiency, the demands on mechanical components are limited by materials performance (1, 2). For military and commercial aircraft engines operating in aggressive environments, including near sea and coastal regions, corrosion is a critical concern. In

aircraft engines, corrosion plays a significant factor limiting the lifetime of tribo-mechanical systems (3-5). Recent analysis of aviation engine maintenance activities found that historically, a leading cause for jet engine bearing removed from service has been attributed to corrosion (3-5). Although more current aircraft maintenance data does not exist in the literature, it follows that corrosion resistance should be considered as an important factor in any effort to maximize bearing wear performance.

Bearing steels have a variety of applications within the aerospace industry, both as rolling elements and raceways of bearings (6-8). For more than a century, advances in processing and alloy development have progressively led to increased performance of rolling bearings (6, 9, 10). Corrosion susceptibility is an integral part of bearing performance evolution since it can determine component lifetime and accelerate wear damage in tribo-corrosion conditions (3, 11-13). Hence, there is ample motivation to design steels with superior corrosion resistance: in addition to safety concerns, bearing longevity offers economic incentives in reduced maintenance and repair costs (14-16). For M50, a current bearing steel used in gas-turbine engines, corrosion resistance is a system limiting constraint (7, 17-20). UNS 42670, or AMS 5930 (tradename Pyrowear® 675 (P675)), was developed as a cost-effective martensitic stainless steel (MSS) candidate for aerospace bearings, with the goal of improving wear lifetime by achieving the corrosion resistance of 440C steel whilst maintaining a fracture toughness higher than that of M50 or M50NiL (a low-carbon variant for use in elevated temperatures) (21).

P675 is a carburizable MSS that requires tailored surface treatments to meet specific aerospace performance requirements via case-hardening (17, 22, 23). With a chromium content exceeding 12%, P675 is considered "stainless" due to spontaneous

oxide film formation which passivates the steel (24, 25). During carburization inward

carbon diffusion causes the formation of intermetallic carbides to precipitate in the case

region (26-28). Case hardening introduces compressive stresses in the surface and allows

the bearings to perform under higher loads and rotational speeds and suppresses surface

crack opening (6, 29, 30). However, coarse carbides and nitrides are also associated with

poor fatigue performance and premature fatigue spalling (6, 7, 31). The resulting

performance characteristics of P675 are determined by the specific heat treatment

schedule to, in part, optimize the type and manner of carbide population present in the

case region.

Substantial work has been done to optimize P675 steel to increase resistance to

wear and fatigue by various surface and heat treatments implemented post production

(14, 29, 32-37). The primary carbides found in P675 are M_7C_3 (orthorhombic) and

M23C6 (face-centered cubic) (29, 38). $M_{23}C_6$ forms after the precipitation of M_7C_3 (39)

and because carbon content decreases as a function of depth within the steel, M_7C_3 is

predominate near the surface, whereas $M_{23}C_6$ is more abundant deeper within the steel

(38). Similar to carburization, during carbo-nitriding (CN) nitrides including α-N, ε-Fe_{2-3N}

and γ'-Fe_4N are precipitated in addition to carbides, producing a case hardened surface

with significantly improved corrosion resistance (1, 6, 14, 20, 35, 40, 41). It is well

known that CN degrades corrosion properties at high processing temperatures with high

carbon steels (i.e. duplex hardening process). However, CN (duplex hardening and

combined cycle) of P675 has been shown to increase corrosion resistance, most likely

due to its low carbon and high chromium elemental composition (20, 35). However, the

corrosion resistance of P675 is primarily determined by the carbide network formed as a result of the heat treatment schedule (20).

Steels tempered at higher temperatures typically experience greater carbide growth, and thus a larger depletion of chromium within the surrounding steel matrix adjacent to carbide edges, due to sensitization (26, 42-44). Chromium depleted zones can prevent the formation of an effective passive oxide film on the surface and yield a reduced corrosion resistance. Conversely, lower tempering temperature provides greater chromium homogenization in the matrix and smaller martensitic lathe width, promoting overall corrosion resistance (28, 39, 45-47). There is a small amount of research published on bearing steel microstructure and its effects on corrosion behavior (2, 44, 48-51). Localized corrosion is expected to be the dominant form of corrosion observed in corrosion-resistant bearing steels due to their stainless nature (6, 10) Attempts to predict localized corrosion behavior of stainless steels through empirical (elemental composition based) corrosion performance metrics such as the pitting resistance equivalency number (PREN), are largely ineffective may not accurately correlate with measured corrosion rate because of the strong influence of the near-surface microstructure on corrosion behavior. (20, 52-54).

Surface treatments designed to improve fatigue life often reduce corrosion resistance and overall wear life. Wear life is strongly influenced by corrosion attack, which has not been studied with this generation of martensitic bearing steels. To address this knowledge gap, the aim of this study is focused on assessing the corrosion behavior of processing parameters for P675 that possess the greatest promise for wear performance optimization. Recent work done by Trivedi et al. showed that P675-HTT outperformed

P675-LTT and P675-CN in L_{50} life comparison for rolling contact fatigue (RCF) testing of bearings with Si_3N_4 rolling elements (34). However, LTT and CN treated surfaces have higher corrosion resistance compared to HTT. Better understanding the connection between corrosion behavior, tribological performance, and wear life of the steels will support alloy development and tailoring of processing parameters to achieve desired performance specific to the operating environment conditions (11). This study provides a new application of electrochemical methods to characterize differences in corrosion evolution and contributes to a more comprehensive understanding of the wear behavior of martensitic bearing steels designed for advanced gas-turbine engines in aggressive environments.

Experiment

The steels considered for this work are classified as carburizable martensitic stainless steels. Prior to heat and surface treatment, all steel samples possessed a nominal bulk composition as listed in Table 3.1.

To obtain a balance of desired properties, a proprietary set of heat treatments were applied to P675 during which samples were case carburized followed by quenching and tempering. All samples were melted using vacuum induction melting-vacuum arc re-melting (VIM-VAR) to ensure production cleanliness and increase fatigue life (36). The main difference between the steels considered is the final tempering temperature and composition of diffusing solute atoms in the tempering atmosphere. P675-HTT samples were tempered at a temperature of 496°C while LTT samples at 316°C. The P675-CN samples were processed via low pressure vacuum carbo-nitriding. By introducing acetylene as well as nitrogen (via ammonia gas) within the atmosphere, the CN sample is

able to obtain a carbo-nitrided surface (35). For all samples, case depth ranges from 750-1250 µm (35).

Samples were prepared by heat treating rods that were finish ground by a machine shop, and then polished and sliced in to small cylinders (9.5 mm diameter x12 mm height). This produced a uniform treatment on the circumferential surface of the cylinders that decreased radially inward to the unaffected core. To investigate comparable case regions, each test was only conducted on a single pristine steel surface which had not been tested previously. Replicate testing utilized identical samples from the same heat treatment. There was no instance where a sample was re-polished for additional testing to avoid testing a surface further into the case depth.

<u>Electrochemical Testing</u>

Anodic polarization (AP) and electrochemical impedance spectroscopy (EIS) testing was performed using a custom built 3-electrode electrochemical cell and a research grade potentiostat (Bo-Logic SP300). A saturated calomel electrode (SCE) (Fisherbrand™ accumet™) fitted with a Luggin probe was used as the reference electrode and platinum mesh as the counter electrode. Electrochemical testing was conducted in 0.01 M NaCl solution prepared with DI water (AP testing) or synthetic seawater (Ricca Chemical) to ASTM D1141 standards (EIS testing). For polarization scans the open circuit potential (OCP) was monitored for 30 minutes then a scan rate of 0.5 mV/s was used to polarize the sample starting at -0.1V vs OCP. AP testing ended when the potential reached 0.25V from the initial OCP. For EIS testing, samples were non-polarized (at OCP) allowing non-accelerated corrosion evolution and scans were executed every 2 hours following an initial 30-minute period at OCP. A total of 25 EIS

scans (or cycles) were completed for each individual sample, with a minimum of 5 samples from each heat treatment. EIS scans were conducted from 0.01 Hz to 1 MHz with a ±10 mV amplitude sinusoidal signal. All samples were only tested once on the exposed surface due to the graded microstructure of the carburized steels.

<u>Surface Characterization</u>

An analytical scanning electron microscope (SEM)(Hitachi S-3400N-II) coupled with an electron dispersive spectroscopy (EDS)(Oxford X-Max) unit was utilized to characterize the surface of the steels. Carbide and microstructure analysis was conducted using image analysis software (ImageJ). SEM micrographs were analyzed for carbide size, frequency, and area fraction of the matrix by converting images into an 8-bit image and then executing a particle analysis on a ~6000 μm^2 area square. Stylus profilometry was conducted using a high resolution benchtop stylus profilometer (Bruker DektakXT). Prior to profilometry, samples were mounted on a 10 mm metal specimen disc in order to add stability to the cylinder shaped samples. All images acquired used a 60 second scan duration and a stylus force of 3 mg. The probe radius was 2µm and had a scan range of 524 µm. This analysis yielded 120,000 points per scan with a scan resolution of ~0.17µm.

Results

<u>Microstructure Evaluation</u>

Cross-sectional SEM backscatter electron (BSE) micrographs were taken of each of the steels. Figure 3.1 shows micrographs of the carburized area as well as a magnified image of surface carbides of each of the steels. The three different heat treatments produced differences in both carbide size and morphology, in agreement with existing

reported results (55). Image analysis was done on a ~6000 μm^2 area approximately 50

μm into the sample surface, Figure 1. P675-HTT had the largest average carbide size

(4.17 ± .83 μm^2), followed by P675-LTT (1.73 ± .21 μm^2), and P675-CN (1.02 ± .19

μm^2). Similarly, P675-HTT had the highest area fraction of carbides relative to the matrix

at 27%, while P675-LTT (15%) and P675-CN (13%) had lower area fractions of carbides

in the analyzed area. P675-CN did not possess a distinct nitride layer due to the surface

grinding and polishing during surface preparation and precipitates were similar in

appearance to the LTT sample. N-containing precipitates were indistinguishable from

carbides in P675-CN as investigated herein. In previous related work it was shown that

P675-CN had elevated amounts of nitrogen (~0.5 atom wt.%) and nitrides in the near

surface region (≤ 250 μm) (35). Carbides in P675-HTT were the largest and showed the

most interconnectivity between globular shaped carbides. Conversely, P675-LTT and

P675-CN had smaller carbides that had a larger separation between each other, with

P675-CN, carbides were slightly more circular and evenly distributed.

Electrochemical Testing

The difference in electrochemical behavior of the active case—hardened surface

and passive unaffected core region of P675 can be seen in Figure 3.2. Testing was

conducted in 0.01M NaCl solution to promote passive behavior on the inner core of the

sample and highlight the change in corrosion resistance between the surface and core.

The P675 core displayed passive behavior from -0.12 to 0 V vs SCE with a passive

current density of 1.48e-4 mA/cm^2. Breakdown of passivity is seen at ~0 V vs SCE

indicated by a rapidly increasing current with potential. The surface for all three surface

treatments did not show passive behavior, but instead displayed typical activation

controlled corrosion behavior. To assess the nature of active corrosion in a simulated

working atmosphere, subsequent electrochemical testing was conducted in synthetic

seawater (20). Corrosion density rates were extracted from AP scans and averaged from

six replicate tests using Tafel fitting procedures reported previously (56) (Figure 3.3),

where P675-HTT had the largest current density (6.9e-6 $\pm$ 2.8e-6 A/cm^2), followed by

P675-LTT (1.2e-6 $\pm$ 2.8e-7 A/cm^2) and P675-CN (3.2e-7 $\pm$ 1.0e-7 A/cm^2); results were

compared to corrosion resistant benchmark materials M50 NiL and Cronidur 30. Scatter

in the data observed for HTT seen in Figure 3.3 was typical and in agreement with

previous studies (20). Polarization scans shown in Figure 3.3 offer a rapid method of

corrosion rate ranking between the three surface treatments but offers only a "snapshot"

of the corrosion behavior. To distinguish the form of corrosion and damage evolution

with time, EIS testing with no applied polarization to artificially accelerate damage was

implemented.

OCP monitoring during EIS testing showed that the potential for all steel surface

treatments initially decreased rapidly, then stabilized (see Figure 3.4). P675-HTT had the

lowest average OCP and then became stable at -0.58 +/- 0.02 V vs SCE after

approximately 4.5 hours in the solution. P675-CN continued to decrease throughout the

duration of the test. OCP behavior of P675-LTT was in-between the two other steels

where it's OCP initially decreased, but remained relatively stable after the ~30 hour

mark. However, both P675-LTT and P675-CN maintained an OCP ~ 0.2 V higher than

P675-HTT.

Representative EIS data (Nyquist and Bode Impedance) for each steel obtained

during ~54 hours immersed in solution can be seen in Figure 3.5. Nyquist plots for all

steels typically exhibited two partial semi-circles. Differences were observed between the surface treatments in regards to the magnitude and period when the partial semi-circle arcs emerged. At high frequencies the first arc on P675-HTT typically developed with relatively lower impedance (~20-150 Ω), whereas P675-LTT and P675-CN were much higher, near 5000 Ω. The second partial semi-circle arc emerged at low frequencies and showed higher impedances of approximately 7500, 17000, and 35000 Ω for P675-HTT, P675-LTT, and P675-CN respectively. Bode plots in Figure 3.5b showed a slope change in the mid frequency range indicating two distinct reactions occurring on the sample surface supporting an equivalent circuit model for the system with two time-constants (57).

The low frequency impedance magnitude at 10 mHz was used to approximate the overall effective polarization resistance (Rp*) and provide an initial assessment of the corrosion behavior of the sample (24). Rp* is inversely proportional to corrosion rate and can be used to infer overall corrosion rates and provide a relative ranking (58, 59). The resulting data plotted in Figure 3.6 was the average amongst a minimum of 5 replicate tests with errors bars representing one standard deviation and is plotted as 1/Rp* to correlate directly with corrosion rate. From the low frequency impedance, it is observed that P675-LTT and P675-CN have lower overall corrosion rates that became steady earlier (~10 hrs) during the test. In contrast, P675-HTT had a higher corrosion rate, and progressively increased with time. A representative image for each steel post-testing is provided in Figure 3.6b-d. From post-testing visual examination, P675-LTT and P675-CN were similar and both displayed areas of isolated, high-aspect ratio localized corrosion attack that typically presented as small circular openings of damage on the

surface. In contrast P675-HTT showed more general attack that affected a significantly larger relative percentage of the surface area with lower-aspect ratio attack (Figure 3.5).

To quantify differences in corrosion attack behavior between the heat treatments a visual assessment was done to capture the pitting and general corrosion probabilities following EIS testing (Table 3.2). Probabilities were measured using Equation 1, where n was equal to the number of samples that corrosion typically exhibited either localized or general attack, and N was the total number of electrochemical tests conducted on each type of steel.

$$Probability\ of\ localized\ or\ general\ attack = \left(\frac{n}{1+N}\right) \text{Equation 1}$$

Localized corrosion was chosen for samples that had a single (or several) isolated circular pit openings on the test surface, post electrochemical testing. General corrosion was chosen for samples that had been attacked in a more uniform manner across the test surface, and did not contain discernable isolated circular areas of attack. P675-LTT and P675-CN show a much higher probability of localized attack (90%) than P675-HTT (1%). For general corrosion, P675-HTT has a much higher probability (90%) than P675-LTT (30%) and P675-CN (25%). In addition to the exposed surface corrosion, some samples also experienced minor crevice attack on the edges of the test surface masking. It is likely that the minor instances of crevice attack were triggered by existing surface corrosion that grew to the edge of the exposed surface and hence crevice corrosion was not separately classified.

Post-electrochemical Testing Characterization

Stylus profilometry provided a quantitative assessment of the surface topography at corroded regions and SEM provided high magnification observation of corrosion

damage sites with compositional contrast (not shown) to help reveal the nature of carbide

interaction with corrosion damage. Representative damage site analysis of each heat

treatment are shown in Figure 3.7. Corrosion on P675-HTT typically appeared to be

general, affecting a significant portion of the test area. The most severe attack was in

regions that were several mm's wide and displayed a few plateaus of material that

remained (Figure 3.7a-HTT). Adjacent areas also showed a lesser degree of attack that

extended across most of the sample (e.g. Figure 3.7b-HTT). SEM imaging showed that

the carbides were generally not affected while the matrix was uniformly corroded (Figure

3.7c-HTT). In the areas of severe attack (~30µm deep), the matrix was completely

dissolved, leaving behind a collection of carbides. In the less severe areas of attack

(≤10µm deep) carbides are elevated from the surrounding matrix that was uniformly

attacked.

P675-LTT and P675-CN both showed localized corrosion that typically consisted

of a single large pit with a circular pit opening approximately 300-400µm in diameter

(Figure 3.7a,b-LTT & CN). Surrounding the pits were regions of corrosion product

buildup that were the preserved edge remnants of an apparent "umbrella" cap over the pit

with a span of approximately 500-1000µm beyond the pit edge. The bottom surface of

the pits was significantly enriched with undissolved carbides. Outside of the pitted area,

both P675-LTT and P675-CN showed distinct attack at the chromium depleted matrix

adjacent to carbide boundaries, with P675-CN showing slightly less attack (Figure 3.7c-

LTT & CN). Areas of passivity are indicated as well to highlight an important finding;

quantitative corrosion rate data from electrochemical techniques does not distinguish how

much of the sample is actively corroding. That is, a passive region was not seen in

electrochemical polarization scans but instead exhibited active, Tafel type behavior. The active corroding regions within the large pits thus dominated the resultant polarization curve obscuring contributions from the passive regions. This was the motivation to utilize EIS testing and obtain information about multiple reactions occurring on the entire surface. Through this analysis the manner with which corrosion evolves can be used to aid understanding of the wear performance of these steels in a corrosive tribological setting.

Discussion

<u>Microstructural Analysis</u>

Since the final tempering temperature duration is identical for P675-HTT, P675-LTT, and P675-CN the resultant carbide size after heat treating is directly related to tempering temperature. Locally, the degree of sensitization is correlated with carbide size because during carbide formation chromium is depleted from the areas adjacent to the carbide boundaries as the carbide grows. P675-HTT likely had a higher degree of depletion of chromium in its matrix as evidenced by its larger carbide size. Greater depletion of chromium leads to a less effective oxide layer, lower corrosion resistance, and can also hinder re-passivation (60). P675-HTT had the highest carbide area fraction (27%) compared to P675-LTT (15%) and P675-CN (13%) which also had smaller carbide size and a likely lower degree of micro-sensitization. For P675-LTT and P675-CN the carbide size and distribution likely leads to better corrosion resistance due to greater amount of solid solution chromium within the matrix. Although characterization of specific nitrides was not in the scope of this study, previously reported surface analysis on P675-CN confirmed the presence of nitrogen within the matrix and precipitated

nitrides, though at a much lower amount compared to chromium carbides (29, 35).

Addition of nitrogen to low carbon stainless steels containing molybdenum and silicon

enhances corrosion resistance and pitting resistance (61-65) and its presence in the case

layer of P675-CN similarly contributes to its superior corrosion resistance.

Electrochemical Characterization

Although bearings are typically in contact with aviation grade lubricants during

service, electrochemical testing in ester-based lubricants is ineffective due to very high

solution resistivity (16). Corrosion develops in-service due to water-in-oil contamination

and lubricant degradation which reduces the solution resistance and enables

electrochemical reaction to proceed. Since corrosion is an aqueous process, accelerated

testing was conducted in aqueous solutions to avoid complications testing in oil while

still simulating the corrosive electrolyte bearings encounter in service.

For all surface treatments, initial polarization testing of the core region,

unaffected by the carburizing atmosphere, displayed passive behavior with a current

density that remained low with increasing applied potentials, while the carburized surface

showed active corrosion behavior. This difference in behavior was due to the formation

of carbides in the near-surface region of the steels. The drastically different

microstructure between the carbide decorated case layer and carbide free core provides

for exceptional wear resistance by increasing toughness. Compressive stresses found in

the case are developed during quenching when the austenite transforms into martensite

and is constrained by the more ductile core. The resulting microstructure increases

hardness and prevents surface cracking by suppressing crack initiation and propagation.

For optimized bearing performance the effect of tempering on corrosion behavior is critical since historically, corrosion of bearings in aerospace applications is the most frequent and earliest cause of bearing life degradation (3, 14, 34, 35). Following carburizing all surface treatments exhibited active corrosion when exposed to simulated seawater, and reduced corrosion resistance compared to the core. This differs with findings by Wang et al where carbon implantation on the surface increased corrosion resistance of M50Nil (66). This can be explained by the significantly lower chromium content of M50Nil (~4% as compared to ~13% for P675). In the current study, the rates and appearance of samples post-testing, were dissimilar and varied with the final tempering temperature and carburized atmosphere of the surface treatment. Moreover, the addition of nitrogen to P675-CN significantly increased corrosion resistance in agreement with findings by Laurent et. al. (67).

EIS data was modeled as an equivalent circuit to extract information on the corrosion processes and reactions occurring on the surface of the test samples. Impedance scans conducted over a large frequency range contain information on the contribution of each element within the modeled circuit. This quantitative assessment can be applied to help explain why samples with identical overall composition, but different surface treatments, behaved differently from one another. For this study, a modified Randles circuit with two parallel resistor-capacitor elements was used (Figure 8a) to model the EIS response of the actively corroding surfaces. R1 represents the resistance of the bulk electrolyte, R2 represents the oxide layer resistance, and R3 represents the charge transfer resistance. Constant phase elements (CPE), denoted here as Q1 and Q3, were utilized

instead of capacitors since real reacting surfaces of solids are never completely homogenous, and therefore do not behave as ideal capacitors (42, 68, 69).

Q1 represents the effective oxide layer capacitance and trends with film thickness and quality (69) while Q3 represents the double-layer capacitance at the metal surface.

Equation 2 defines the CPE:

$$Z_{CPE} = \frac{1}{Q(j\omega)^a} \quad \text{Equation 2}$$

Where the constant Q (F.s(a-1)) represents properties associated with the surface of the test sample as well as the electroactive species found near the sample (71). In $j\omega$, $\omega = 2\pi f$ where j is the variable for the complex sinusoidal perturbations and f is the frequency in Hz (71) and α determines how closely the element resembles an ideal capacitor ($\alpha = 1$) or a pure resistor ($\alpha = 0$) (42, 70).

Modeling of the EIS scan data was performed by fitting the Nyquist impedance graphs to a predetermined equivalent circuit (Figure 3.8) using the fitting software provided by the potentiostat manufacturer. Fitting parameters were obtained to provide values for all elements in the equivalent circuit. Values for each of the circuit elements averaged over the entire test duration are shown in Figure 3.8; values displayed represent a minimum of 5 replicate tests, each containing 25 EIS scans/cycle.

Figure 3.9 shows 3-dimensional Nyquist and Bode plots as a function of time coupled with the model fit to highlight the effectiveness of the model and showcase the differences amongst the behaviors of the steels.

Figure 3.10a shows Q1 averaged values of each scan or cycle for each of the three steels. P675-HTT has a much larger Q1 value than the other two steels and increased as a function of time, while the other two steels show lower values that initially increase and

then stay constant for the remainder of the test. When comparing to Figure 3.6a, the behavior of the Q1 graph tracks the corrosion behavior well. Previous work has shown that Q1 is a good predictor of oxide film thickness and is inversely related to film thickness (42, 43, 72). Therefore, the oxide film on P675-HTT is likely thinner or has less effective coverage than those of P675-LTT and P675-CN.

Q3 is representative of a depassivated area where active corrosion is occurring. Q3 is dependent on Q1, and so shows the same ranking of steels as Q1 (Figure 3.10b). Q3 provides an indication of the oxide layer effectiveness in preventing corrosion as well as the corrosion behavior once the oxide layer is compromised. If the oxide layer was completely intact active corrosion would not be present and any effect of the representative Q3 element would be diminished. Therefore, a higher Q3 value, indicates a lower oxide layer effectiveness and a lower corrosion resistance of the bulk matrix of the steel. Fluctuations in the first few of scans for P675-LTT and P675-CN can be explained by the oxide layer initially being penetrated (leading to a larger Q3 value) and the matrix attempting to repassivate and eventually reforming an oxide layer (lowering the Q3 value), see Figure 3.10b. P675-HTT had the highest Q3 values from all steels tested followed by P675-LTT and P675-CN. From this analysis it was determined that the bulk matrix of P675-HTT was not able to effectively protect itself from corrosion attack. Subsequently, this trend confirms findings for Q1 and validates the ineffectiveness of the oxide layer and higher corrosion rate observed on P675-HTT. Similar data from P675-LTT and P675-CN indicate that the bulk matrix of these two steels were able to more effectively protect the steel compared to P675-HTT.

The α values for each of the steels showed similar grouping (Figure 3.11). $\alpha 1$ values were much lower for P675-HTT than for P675-LTT and P675-CN meaning the oxide layer of P675-LTT and P675-CN act as better capacitors and therefore provide better corrosion resistance to the underlying steel by separating charge and blocking current flow across the oxide layer. However, for $\alpha 2$ values, the ranking is reversed; P675-HTT is much higher than P675-LTT and P675-CN. Recall that $\alpha 2$ represents the unprotected matrix of the steel and thus P675-HTT behaves more like a capacitor in the active corrosion cell of the non-protected (or penetrated oxide layer) portion of the sample interface than that of the other steels. Simply put, P675-HTT's oxide layer acts less like a capacitor and does not block current flow while its underlying matrix allows more current flow into the unprotected matrix of the steel, and yields more corrosion damage. The matrix of P675-LTT and P675-CN behave less like a capacitor and allow less current flow to the bulk of the material because most of the current is already absorbed by the more effective oxide layer mentioned above.

R1 is the resistance associated with the electrolyte solution (synthetic seawater) and was nearly identical for all three steels, as expected. R2 is an order of magnitude higher for P675-LTT and P675-CN as compared to P675-HTT (Figure 3.12a). The R2 values are directly correlated to oxide layer performance, and the oxide layer of P675-HTT was significantly less resistive than the other two surface treatments. The lower electrical resistance across the oxide layer will lead to easier current flow and overall less robust or protective oxide film; as is observed via current density measurements. For R3, the charge transfer resistance in active corrosion regions, P675-HTT is an order of magnitude lower than P675-LTT (Figure 3.12b).

P675-HTT is tempered at a higher temperature and higher degree of chromium depletion within the matrix is present. To recall, the microstructural analysis (see Figure 3.1) showed that the area fraction of carbides of HTT was the highest of the three surface treatments considered, at 27%. For HTT a larger carbide size coupled with a significant presence of carbides within the matrix makes passivation less protective in the matrix and depassivation more likely. Moreover, in areas undergoing active dissolution, the rate is higher due to lowered charge transfer resistance compared to the other surface treatments. Interestingly, the microstructural features that cause lower corrosion resistance for HTT also provide better bearing performance in non-corrosive conditions.

Corrosion Mechanism

In summary, based on the microstructural analysis, electrochemical testing, fitting parameters, and stylus profilometry, a corrosion mechanism has been proposed to better understand the method of attack for each type of surface treatment. Previous work by Jiang et. al. on 30Cr15Mo1N steel show two mechanisms of corrosion attack; general corrosion attack with a lacy cover (i.e. where the surface is covered in pits) and localized attack (17). In our generation of steels, we see similar corrosion attack with differences in stoichiometry and precipitate composition. In Figure 3.13 a schematic of a corrosion mechanism is shown of the three steels tested in this study. When observing the schematic, it is shown that the P675-HTT sample begins with a similar microstructure as the P675-LTT except with larger carbides, encompassing a larger portion of the matrix, and a thinner oxide layer. These larger carbides cause more depletion of chromium from the surrounding matrix. This depletion of chromium induces a potential difference between the phases (73) and leads to attack by chlorine ions (found in electrolyte

solution) at the carbide boundaries due to microgalvanic coupling (17, 60, 73). Another source of potential difference could be due to breaks in the oxide film that create sites for pit nucleation (60, 74). Once this nucleation occurs, the surface depassivates and corrosion easily spreads along the surface. When the oxide layer breaks, the sample begins to have a lacy cover while the matrix is consumed due to corrosion. As the sample continues to be attacked the corrosion propagates across the surface, while the lacy cover diminishes, to form one shallow crater-like damage site. For P675-LTT the steel is initially attacked in a similar fashion to P675-HTT, however once corrosion initiates, the matrix of the P675-LTT is able to re-passivate most of its surface because of the more homogenous chromium distribution, due to the lower degree of sensitization. Chloride ions will still preferentially interfere with oxide layer growth of these areas but the surface of LTT more readily passivates compared to HTT. The more protective oxide layer is more resistant to lateral corrosion spreading and instead causes pits to grow deeper with time. In the case of the P675-CN, the corrosion mechanism is similar P675-LTT but dissolved nitrogen and nitrides on the surface from carbo-nitriding further enhances passive film protectiveness.

<u>Corrosion Behavior Influencing Wear</u>

In aggressive environments, synergistic effects of tribo-corrosion reduce wear life and lead to premature failure of the part (75). Corrosion testing in static conditions can provide insight on expected wear performance in a corrosive environment. Compared to lengthy wear testing, electrochemical corrosion testing is much shorter in duration; typically on the order of hours as opposed to months.

In aerospace applications, the steels studied are prone to failure via RCF, where surface initiated cracks or corrosion pits lead to spalling (36, 76, 77). Ball-on-Rod RCF testing and 40mm bearing testing have been used to characterize wear and fatigue life performance of P675-HTT, P675-LTT, and P675-CN in laboratory non-corrosive environment (14, 34-36). In this work, modeling of EIS data provided fitting parameters (Figure 3.8) that were compared with long term wear behavior see Figure 3.14. Further, the L_{10} wear life for P675-HTT and P675-LTT ranked similarly to previously reported corrosion rates (20), and the Q1 parameter results obtained from this study (see Figure 3.8 and 3.14). The addition of nitrogen in the P675-CN samples led to both the longest L_{10} life and highest corrosion resistance even with relatively high amount of retained austenite and thus did not follow corrosion rate ranking (20, 35, 36). Therefore, it was difficult to correlate electrochemical testing with wear behavior. Future work is underway in conducting wear tests in a corrosive environment to validate findings in this study.

For P675 steels, the wear performance and corrosion resistance is controlled by type and nature of carbide precipitation resulting from the various surface treatments considered. The electrochemical methods presented in this study provide rapid testing techniques that can quickly reveal differences in surface behavior with each surface treatment. Importantly, these differences influence both wear behavior in non-corrosive conditions and corrosion propagation-mechanism in corrosive solutions. Future work is needed to determine the effects of corrosion resistance in corrosive-wear-conditions (tribo-corrosion) and the influence of corrosion morphology and pit geometry on spalling/galling by using standard ASTM G98-17 (Standard Test Method for Galling Resistance of Materials). Also corrosive wear testing must be conducted in order to

effectively connect the findings of rapid electrochemical testing techniques with long term wear testing.

Conclusions

Based on microstructural analysis, electrochemical testing, and post-testing surface observations, corrosion aspects of wear life for the three different heat treatments were studied and compared to wear data. For wear applications in corrosive conditions, the performance of aerospace bearing steels is linked with corrosion resistance. In harsh environments, optimized wear lifetime may be achieved from surface treatments that maximize corrosion resistance relative to wear and fatigue resistance. Wear performance implications of each type of surface treatment as applied to MSS in corrosive environments can be more thoroughly investigated using the accelerated methods presented herein.

1. P675-HTT process yields a microstructure that has the largest carbide size and area fraction of carbides within the case region; likely developing a thinner, less effective oxide layer that led to the lowest corrosion resistance from the steels tested, and shortest L10 life for a non-corrosive environment.

2. The lower tempering temperature of P675-LTT caused less sensitization than P675-HTT and a more homogenous distribution of chromium within the matrix; thereby increasing corrosion resistance but decreasing wear performance in a non-corrosive environment.

3. The addition of nitrogen to P675-CN yielded the smallest carbide size and ultimately superior corrosion resistance amongst the steels tested as well as the longest L10 life in non-corrosive wear testing.

4. A mechanism of corrosion attack was proposed for each of the bearing steels studied where the P675-HTT undergoes more-general corrosion attack while P675-LTT and P675-CN experience more-localized pitting corrosion.

References

1. Ooi, Steve, and Bhadeshia HKDH. "Duplex hardening of steels for aeroengine bearings." *ISIJ international* 52.11 (2012): 1927-1934.

2. Nygaard, J. R., et al. "Bearing steel microstructures after aircraft gas turbine engine service." *Materials Science and Technology* 30.15 (2014): 1911-1918.

3. Zaretsky, Erwin V., and Emanuel V. Branzai. "Rolling Bearing Service Life Based on Probable Cause for Removal—A Tutorial." *Tribology Transactions* 60.2 (2017): 300-312.

4. Davies, D. P., S. L. Jenkins, and F. R. Belben. "Survey of fatigue failures in helicopter components and some lessons learnt." *Engineering Failure Analysis* 32 (2013): 134-151.

5. Miller, Jerry L., and Duka Kitaljevich. "In-line oil debris monitor for aircraft engine condition assessment." In *2000 IEEE Aerospace Conference. Proceedings (Cat. No. 00TH8484)*, vol. 6, pp. 49-56. IEEE, 2000.

6. Bhadeshia, H. K. D. H. "Steels for bearings." *Progress in Materials Science* 57.2 (2012): 268-435.

7. Ebert, Franz-Josef. "An overview of performance characteristics, experiences and trends of aerospace engine bearings technologies." *Chinese Journal of Aeronautics* 20.4 (2007): 378-384.

8. Ragen, Mark A., Donald L. Anthony, and Ronald F. Spitzer. "A comparison of the mechanical and physical properties of contemporary and new alloys for aerospace bearing applications." *Bearing steel technology*. ASTM International, 2002.

9. Zaretsky, Erwin V. "Selection of rolling-element bearing steels for long-life applications." *Effect of Steel Manufacturing Processes on the Quality of Bearing Steels*. ASTM International, 1988.

10. Zaretsky, Erwin V. "Rolling bearing steels–a technical and historical perspective." *Materials Science and Technology* 28.1 (2012): 58-69.

11. Dalmau, A., C. Richard, and A. Igual–Muñoz. "Degradation mechanisms in martensitic stainless steels: Wear, corrosion and tribocorrosion appraisal." *Tribology International* 121 (2018): 167-179.

12. Dalmau, A., et al. "Tribocorrosion behavior of new martensitic stainless steels in sodium chloride solution." *Wear* 368 (2016): 146-155.

13. Torrance, A. A., J. E. Morgan, and G. T. Y. Wan. "An additive's influence on the pitting and wear of ball bearing steel." *Wear* 192, no. 1-2 (1996): 66-73.

14. Trivedi, Hitesh K. and Monahan, Ray, "Low Temperature Plasma Nitriding of Pyrowear 675." *Bearing steel Technologies: 10th Volume, Advances in Steel Technologies for Rolling Bearings, STP 1580*, John M. Beswick, Ed., pp 444-464, doi:10.1520/STP158020140062 ASTM International: West Conshocken, PA, USA, 2015

15. Yagita, Kazuhiro, and Chikara OHKI. "Plasma nitriding treatment of high alloy steel for bearing components." *NTN Technical Review* 78 (2010).

16. Hurley, Michael F., et al. "Corrosion assessment and characterization of aerospace-bearing steels in seawater and ester-based lubricants." *Corrosion* 68.7 (2012): 645-661.

17. Jiang, Zhouhua, et al. "Relationship between microstructure and corrosion behavior of martensitic high nitrogen stainless steel 30Cr15Mo1N at different austenitizing temperatures." *Materials* 10.8 (2017): 861.

18. Berns, Hans, Franz-Josef Ebert, and Hans-Werner Zoch. "The new low nitrogen steel LNS—A material for advanced aircraft engine and aerospace bearing applications." *Bearing Steels: Into the 21st Century*. ASTM International, 1998.

19. Popgoshev, D., and R. Valori. "Rolling contact fatigue evaluation of advanced bearing steels." *Rolling Contact Fatigue Testing of Bearing Steels*. ASTM International, 1982.

20. Kvryan, A., Faulkner, E., Lysne, D., Carter, N., Acharya, S., Rafla, V., Trivedi, H. K., and Hurley, M. F., "Electrochemical Corrosion Test Methods for Rapid Assessment of Aerospace Bearing Steel Performance," Bearing Steel Technologies: 11th Volume, Progress in Steel Technologies and Bearing Steel Quality Assurance, ASTM

STP1600, J. M. Beswick, Ed., ASTM International, West Conshohocken, PA, 2017, pp. 466–486, http://dx.doi.org/10.1520/STP1600201601503

21. Wert, David E. "Development of a carburizing stainless steel alloy." *Advanced Materials and Processes* 145.6 (1994): 89-91.

22. Chakraborty, Gopa, et al. "Study on tempering behaviour of AISI 410 stainless steel." *Materials Characterization* 100 (2015): 81-87.

23. Isfahany, A. Nasery, H. Saghafian, and G. Borhani. "The effect of heat treatment on mechanical properties and corrosion behavior of AISI420 martensitic stainless steel." *Journal of Alloys and Compounds* 509.9 (2011): 3931-3936.

24. Jones Denny, A. "Principles and prevention of corrosion." *Upper Saddle River, NJ, USA, Pearson-Prentice Hall* (1992).

25. Uhlig, Herbert H. *Uhlig's corrosion handbook*. Vol. 51. John Wiley & Sons, 2011

26. Peissl, S., et al. "Influence of chromium, molybdenum and cobalt on the corrosion behaviour of high carbon steels in dependence of heat treatment." *Materials and Corrosion* 57.10 (2006): 759-765.

27. Godec, Matjaž, et al. "Characterization of the carbides and the martensite phase in powder-metallurgy high-speed steel." *Materials Characterization* 61.4 (2010): 452-458.

28. Han, Lee-Long, Chun-Ming Lin, and Yih-Shiun Shih. "Corrosion resistance of ASSAB Stavax ESR stainless steel by heat and cold treatment." *Materials Transactions* 54.5 (2013): 833-838.

29. Klecka, Michael A., Ghatu Subhash, and Nagaraj K. Arakere. "Microstructure–property relationships in M50-NiL and P675 case-hardened bearing steels." *Tribology Transactions* 56.6 (2013): 1046-1059.

30. Smallman, Raymond E., and A. H. W. Ngan. *Physical metallurgy and advanced materials*. Elsevier, 2011

31. Parker, Richard Jay, and Eric N. Bamberger. "Effect of carbide distribution on rolling-element fatigue life of AMS 5749." *NASA Technical Paper* 2189 (1983).

32. Trivedi, Hitesh K., Vern Wedeven, and William Black. "Effect of Silicon Nitride Ball on Adhesive Wear of Martensitic Stainless Steel Pyrowear 675 and AISI M-50 Races with Type II Ester Oil." *Tribology Transactions* 59.2 (2016): 363-374.

33. Trivedi, Hitesh K., Nelson H. Forster, and Lewis Rosado. "Rolling contact fatigue evaluation of advanced bearing steels with and without the oil anti-wear additive tricresyl phosphate." *Tribology Letters* 41.3 (2011): 597-605.

34. Trivedi, H. K., Rosado, L., Gerardi, D. T., and McCoy, B., "Fatigue Life Performance of Hybrid Angular Contact Pyrowear 675 Bearings," Bearing Steel Technologies: 11th Volume Progress in Steel Technologies and Bearing Steel Quality Assurance, ASTM STP1600, J. M. Beswick, Ed., ASTM International, West Conshocken, PA, 2017, pp. 275-295, http://dx.doi.org/10.1520/STP160020170003

35. Trivedi, Hitesh K., Otto, Frederick, McCoy, Bryan, Bhattacharya, Rabi S., Piazza, Timothy, "Heat Treatment Process for Martensitic Stainless Steel Pyrowear 675 for Improved Corrosion Resistance." *Bearing Steel Technologies: 10th Volume, Advances in Steel Technologies for Rolling Bearings, STP 1580*; John M. Beswick, Ed., pp 465-484, doi:10.1520/STP158020140061, ASTM International: West Conshocken, PA 2015

36. Kirsch, M. and Trivedi, H., "Microstructural Changes in Aerospace Bearing Steels under Accelerated Rolling Contact Fatigue Life Testing." *Bearing Steel Technologies: 11th Volume, Progress in Steel Technologies and Bearing Steel Quality Assurance, ASTM STP 1600*, J.M. Beswick, Ed., ASTM International: West Conshohocken, PA, 2017, pp. 92–107, http://dx.doi.org/10.1520/STP160020170005

37. Wells, M. G. H., et al. "Rolling contact fatigue behaviour of Pyrowear 675." *Surface engineering* 15.4 (1999): 321-323.

38. Hetzner, Dennis W., and William Van Geertruyden. "Crystallography and metallography of carbides in high alloy steels." *Materials Characterization* 59.7 (2008): 825-841.

39. Dong, Ji, et al. "Carbide precipitation in Nb-V-Ti microalloyed ultra-high strength steel during tempering." *Materials Science and Engineering: A* 683 (2017): 215-226.

40. Schneider, M. J., Chatterjee, M.S., and The Timken Company "Introduction to surface hardening of steels." *ASM Handbook, Steel Heat-Treating Fundamentals and Processes* 4 (2013).

41. Li, C. X., and T. Bell. "Corrosion properties of plasma nitrided AISI 410 martensitic stainless steel in 3.5% NaCl and 1% HCl aqueous solutions." *Corrosion Science* 48.8 (2006): 2036-2049.

42. Lu, Si-Yuan, et al. "Influence of heat treatment on the microstructure and corrosion resistance of 13 wt pct Cr-type martensitic stainless steel." *Metallurgical and Materials Transactions A* 46.12 (2015): 6090-6102.

43. Lu, Si-Yuan, et al. "The effect of tempering temperature on the microstructure and electrochemical properties of a 13 wt.% Cr-type martensitic stainless steel." *Electrochimica Acta* 165 (2015): 45-55.

44. Anantha, Krishnan Hariramabadran, et al. "In Situ AFM Study of Localized Corrosion Processes of Tempered AISI 420 Martensitic Stainless Steel: Effect of Secondary Hardening." *Journal of the Electrochemical Society* 164.13 (2017): C810-C818.

45. Baldissera, Paolo, and Cristiana Delprete. "Deep cryogenic treatment of AISI 302 stainless steel: Part II–Fatigue and corrosion." *Materials & Design* 31.10 (2010): 4731-4737.

46. Yasavol, N., and F. Mahboubi. "The effect of duplex plasma nitriding-oxidizing treatment on the corrosion resistance of AISI 4130 steel." *Materials & Design* 38 (2012): 59-63.

47. Oppenkowski, A., S. Weber, and W. Theisen. "Evaluation of factors influencing deep cryogenic treatment that affect the properties of tool steels." *Journal of Materials Processing Technology* 210.14 (2010): 1949-1955.

48. Zhang, Yue, et al. "Influence of microstructure evolution on tribocorrosion of 304SS in artificial seawater." *Corrosion Science* 88 (2014): 423-433.

49. Xing'an, Wang, et al. "Effect of rare earth addition on microstructure and corrosion behavior of plasma nitrocarburized M50NiL steel." *Journal of Rare Earths* 34.11 (2016): 1148-1155.

50. Vignal, Vincent, Stéphanie Bissey-Breton, and Jean-Baptiste Coudert. "Mechanical properties and corrosion behaviour of low carbon martensitic stainless steel after machining." *International Journal of Machining and Machinability of Materials 7* 15.1-2 (2014): 36-53.

51. Anantha, Krishnan Hariramabadran, et al. "Correlative microstructure analysis and in situ corrosion study of AISI 420 martensitic stainless steel for plastic molding applications." *Journal of the Electrochemical Society* 164.4 (2017): C85-C93.

52. Sedriks, A.J., *Corrosion of stainless steel, 2. Edition*. United States: 1996.

53. Jargelius-Pettersson, R. F. A. "Application of the pitting resistance equivalent concept to some highly alloyed austenitic stainless steels." *Corrosion* 54.2 (1998): 162-168.

54. Rebak, R. B., and P. Crook. "Improved pitting and crevice corrosion resistance of nickel and cobalt based alloys." *Proc. Symposium on Critical Factors in Localized Corrosion III*. Vol. 194. 1999.

55. Shockley, J. Michael, Derek J. Horton, and Kathryn J. Wahl. "Effect of aging of 2507 super duplex stainless steel on sliding tribocorrosion in chloride solution." *Wear* 380 (2017): 251-259.

56. Stern, Milton, and Al L. Geary. "Electrochemical polarization I. A theoretical analysis of the shape of polarization curves." *Journal of the Electrochemical Society* 104.1 (1957): 56-63.

57. Marcelin, Sabrina, Nadine Pébère, and Sophie Régnier. "Electrochemical characterisation of a martensitic stainless steel in a neutral chloride solution." *Electrochimica Acta* 87 (2013): 32-40.

58. Frankel, Gerald S. "Electrochemical techniques in corrosion: status, limitations, and needs." *Journal of Testing and Evaluation* 42.3 (2008): 517-538.

59. Scully, J. R., and S. T. Hensley. "Lifetime prediction for organic coatings on steel and a magnesium alloy using electrochemical impedance methods." *Corrosion* 50.9 (1994): 705-716.

60. Taji, Iman, Mohammad Hadi Moayed, and Mostafa Mirjalili. "Correlation between sensitisation and pitting corrosion of AISI 403 martensitic stainless steel." *Corrosion Science* 92 (2015): 301-308.

61. Szklarska-Smialowska, Z., and ZS-Smialowska. *Pitting and crevice corrosion*. Houston, TX: NACE International, 2005.

62. Streicher, M. A. "Pitting corrosion of 18Cr-8Ni stainless steel." *Journal of the Electrochemical Society* 103.7 (1956): 375-390.

63. Rosenfeld, I. L., and I. S. Danilow. "Lochfraß-(Pitting-) Korrosion passiver, rostfreier Stähle." *Zeitschrift für Physikalische Chemie* 226.1 (1964): 257-282.

64. Chigirinskaya, L. "Corrosive Behavior of Chromium-Nickel-Molybdenum Steel Containing Nitrogen." *Prot. Met.(USSR)*20.3 (1984): 320-323.

65. Bandy, R., and D. Van Rooyen. "Properties of nitrogen-containing stainless alloy designed for high resistance to pitting." *Corrosion* 41.4 (1985): 228-233.

66. Wang, Fangfang, et al. "Corrosion resistance of carbon ion-implanted M50NiL aerospace bearing steel." *Progress in Natural Science: Materials International* 27.5 (2017): 615-621.

67. Laurent, Olivier, Bellus, Jacques, Puech, Sylvain, Devilder, Franck, and Benbahmed, Atman, "Review of XD15NW (Through Hardening) and CX13VDW (Case Carburizing) Cost-Effective Corrosion Resistant Bearing Steels Grades," *Bearing Steel Technologies: 10th Volume, Advances in Steel Technologies for Rolling*

Bearings, STP 1580, John M. Beswick, Ed., pp. 239-258, doi:10.1520/STP158020140121, ASTM International, West Conshocken, PA 2015.

68. Agarwal, Pankaj, Mark E. Orazem, and Luis H. Garcia-Rubio. "Measurement models for electrochemical impedance spectroscopy I. Demonstration of applicability." *Journal of the Electrochemical Society* 139.7 (1992): 1917-1927.

69. Luo, H., et al. "The electrochemical behaviour of 2205 duplex stainless steel in alkaline solutions with different pH in the presence of chloride." *Electrochimica Acta* 64 (2012): 211-220.

70. Liu, C., Q. Bi, and A. E. I. S. Matthews. "EIS comparison on corrosion performance of PVD TiN and CrN coated mild steel in 0.5 N NaCl aqueous solution." *Corrosion Science* 43.10 (2001): 1953-1961.

71. Tamilselvi, S., V. Raman, and N. Rajendran. "Corrosion behaviour of Ti–6Al–7Nb and Ti–6Al–4V ELI alloys in the simulated body fluid solution by electrochemical impedance spectroscopy." *Electrochimica Acta* 52.3 (2006): 839-846.

72. Hirschorn, Bryan, et al. "Determination of effective capacitance and film thickness from constant-phase-element parameters." *Electrochimica Acta* 55.21 (2010): 6218-6227.

73. Kvryan, Armen, Corey M. Efaw, Kari A. Higginbotham, Olivia O. Maryon, Paul H. Davis, Elton Graugnard, Hitesh K. Trivedi, and Michael F. Hurley. "Corrosion Initiation and Propagation on Carburized Martensitic Stainless Steel Surfaces Studied via Advanced Scanning Probe Microscopy." *Materials* 12, no. 6 (2019): 940.

74. Burstein, G. T., and S. P. Vines. "Repetitive nucleation of corrosion pits on stainless steel and the effects of surface roughness." *Journal of the Electrochemical Society* 148.12 (2001): B504-B516.

75. Georgiou, Emmanuel, and Dirk Drees. "Tribocorrosion: Risks and Potentials." 2016, www.lube-media.com/wp-content/uploads/2017/11/Lube-Tech107-TribocorrosionRisksandPotentials.pdf.

76. Sadeghi, Farshid, et al. "A review of rolling contact fatigue." *Journal of Tribology* 131.4 (2009): pp. 0414031-04140315.

77. Zaretsky, Erwin V., and Emanuel V. Branzai. "Effect of rolling bearing refurbishment and restoration on bearing life and reliability." *Tribology Transactions* 48.1 (2005): 32-44.

Figures

P675-HTT		P675-LTT	P675-CN
Carbide area (μm²)	4.17	1.73	1.02
Area Fraction (%)	27	15	13
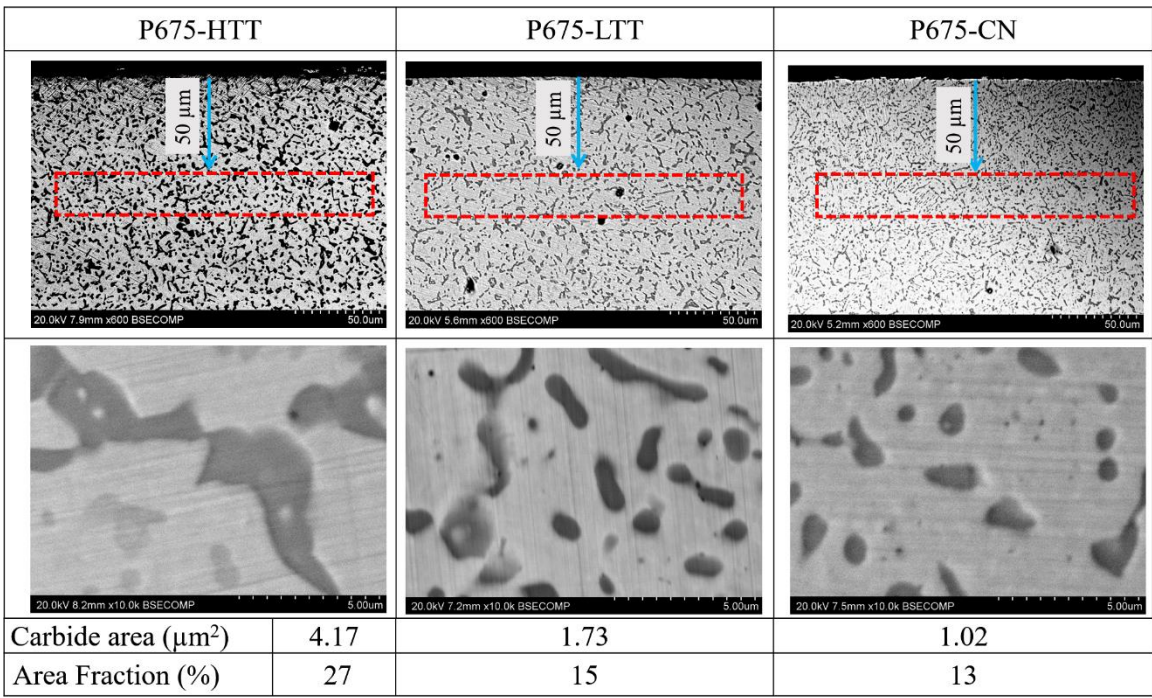
Figure 3.1   Backscatter electron micrographs (BEM) of the samples' cross section with illustrated box representing area where carbide size analysis was performed. Bottom row are BEM's of the surface of each sample to show that the matrix corresponds to similar carbide structure found on the surface. Table below images indicated average carbide area and area fraction for each of the steels obtained from three replicate steels and three separate locations on each sample

(a)   (b)
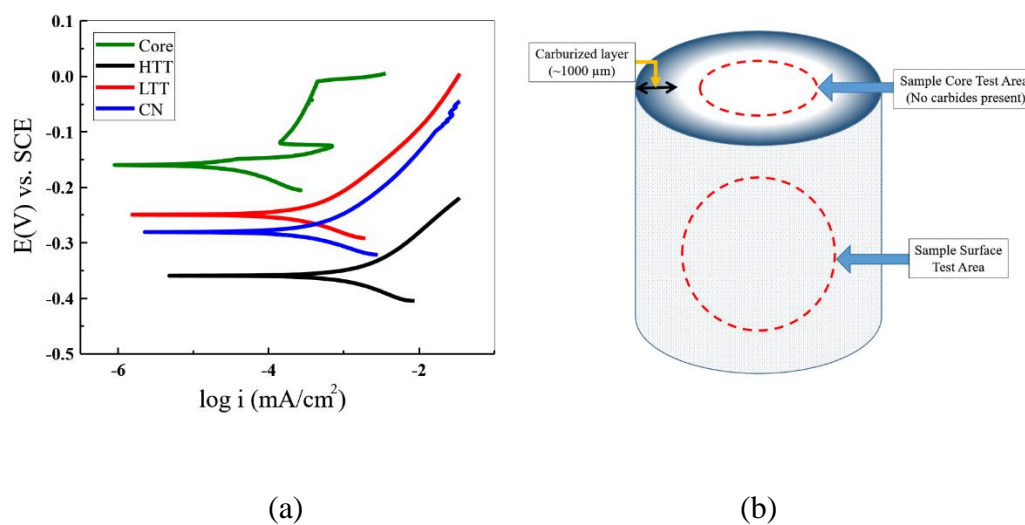
Figure 3.2   (a) Anodic Polarization (AP) scans of untreated P675 core and outer surface of P675-HTT, P675-LTT, and P675-CN to illustrate the passive nature of the core versus the active corrosion behavior of the surface. (b) Illustration of a steel cylinder sample indicating test areas for scans conducted for previous graph.
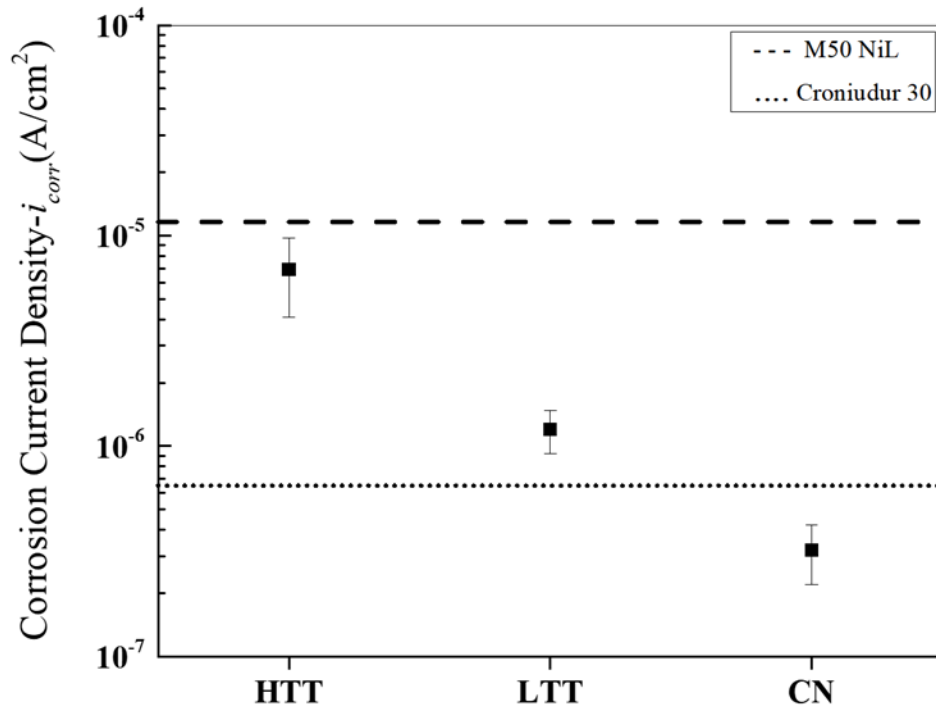
Figure 3.3 **Graph of averaged corrosion rate of each steel obtained by Tafel fitting of AP scans. Reference corrosion rates for M50 NiL (purple) and Cronidur 30 (orange) are shown as a reference to current bearing steels in service.**
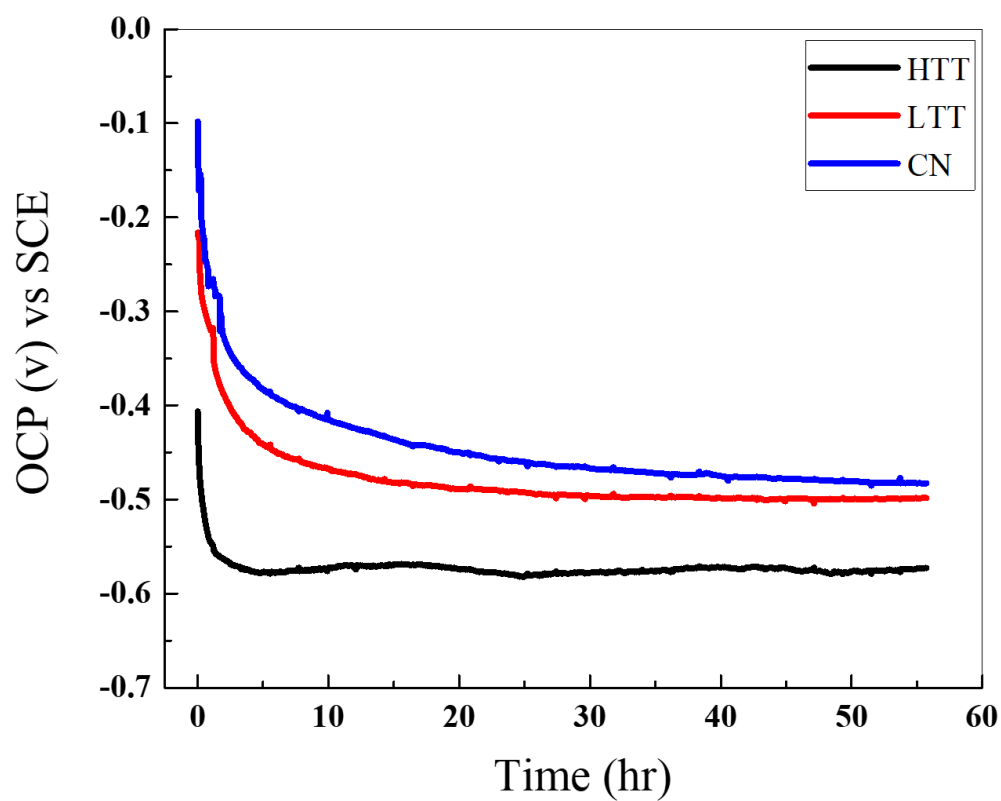
Figure 3.4   Open Circuit Potential (OCP) values obtained during EIS testing of P675-HTT (black), P675-LTT (red), and P675-CN (blue) averaged from 5 replicate scans of each steel where P675-HTT has a lower OCP than P675-LTT and P675-CN, indicating a lower corrosion potential.

(a) (b)
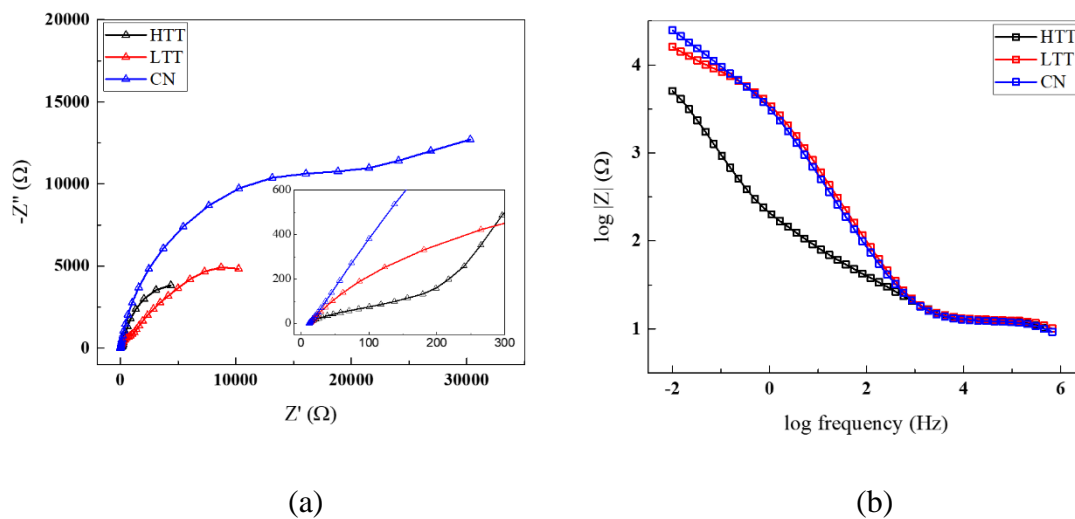
Figure 3.5 **Representative Nyquist Impedance (a) and Bode Impedance (b) plot for final cycle of testing for each steel (~54 hours in solution). Nyquist plot includes an inset plot highlighting the differences in high frequency behavior for each sample to show how samples behave during the first scan.**

(a) (b) (c) (d)
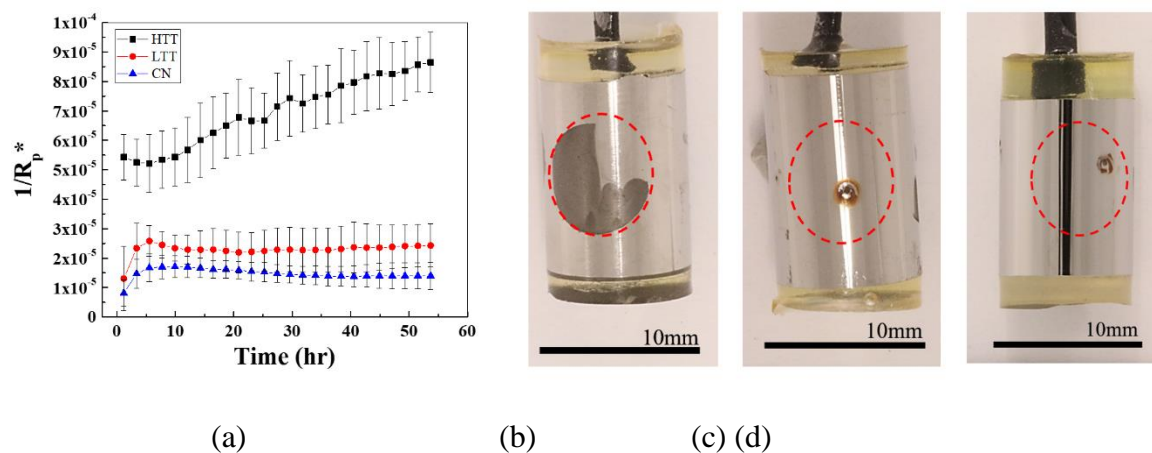
Figure 3.6 **(1/Rp*) as a function of time-indicating corrosion rate for P675-HTT, P675-LTT, and P675-CN (a). Photograph of representative samples post electrochemical testing (b) P675-HTT, (c) P675-LTT, and (d) P675-CN showing different corrosion morphology for each steel.**
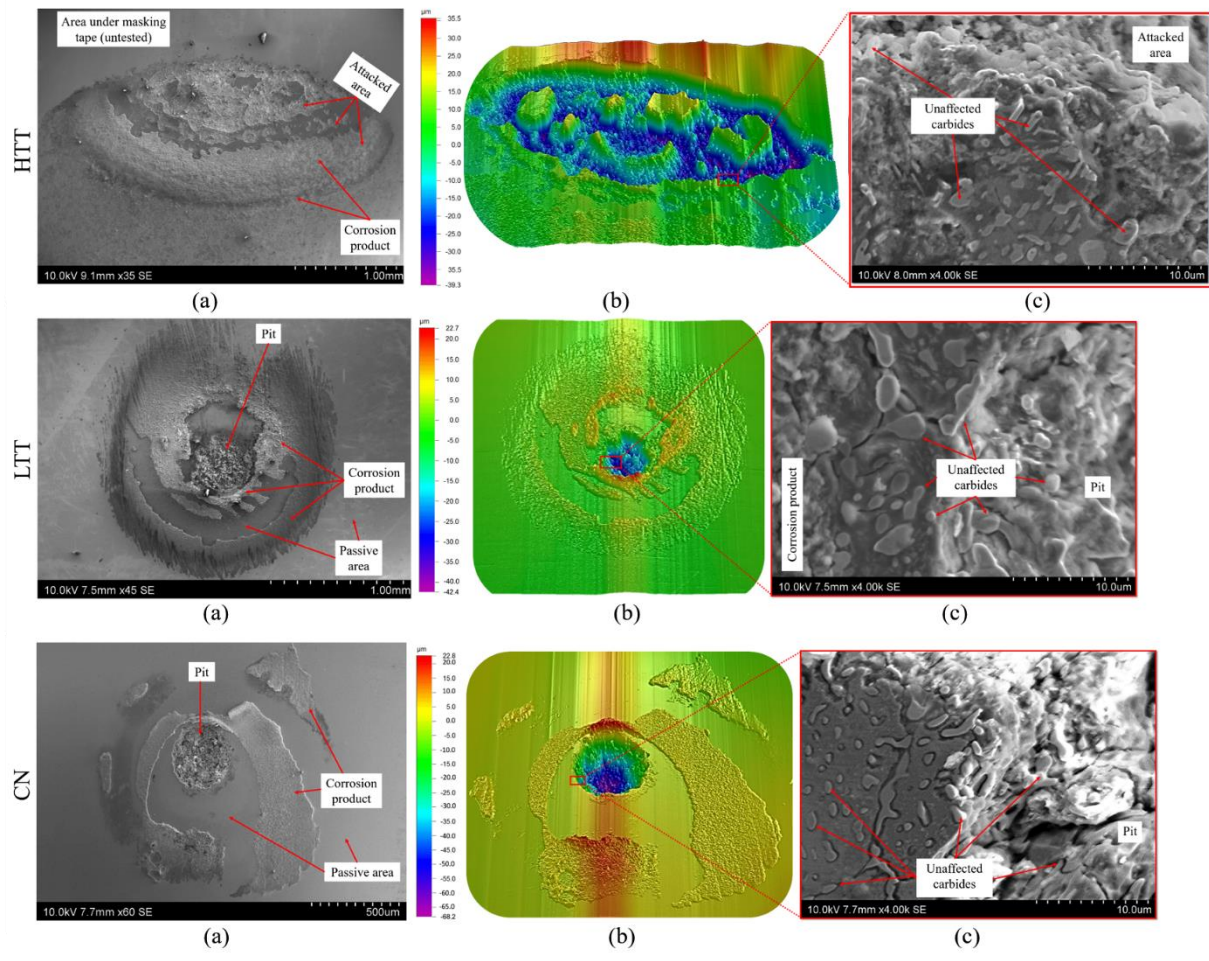
Figure 3.7 **(a) SEM micrographs of electrochemically tested surfaces for P675-HTT, P675-LTT, and P675-CN showing differences in corrosion morphology. (b) 3-Dimensional stylus profilometry (SP) to highlight depth and height of corrosion attack of testing area for each sample. (c) SEM micrographs of carbides on the edge of the corroded areas for each steel as indicated by the red box on the SP image preceding it. This zoomed in micrograph illustrates how carbides are affected in each of the steels and how corrosion affects the surrounding matrix.**

(a)
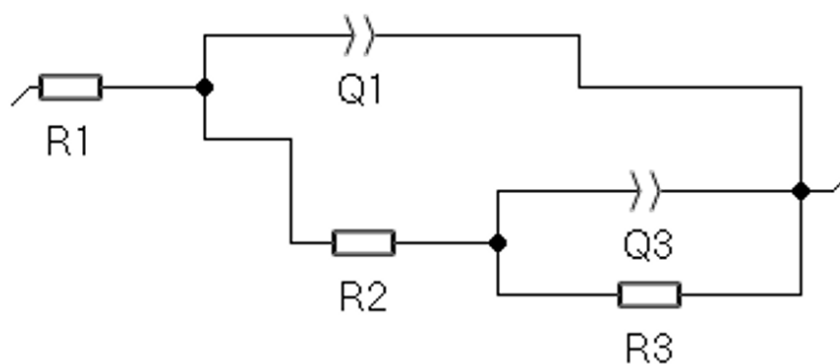
Steel	R1 (Ω)	Q1 (F.s$^{(\alpha-1)}$)	α1	R2 (Ω)	Q3 (F.s$^{(\alpha-1)}$)	α3	R3 (Ω)
P675-HTT	11	3.14E-04	0.70	116	6.24E-04	0.94	8615
P675-LTT	12	4.71E-05	0.85	3997	3.48E-04	0.69	21607
P675-CN	12	4.50E-05	0.85	7926	4.26E-04	0.59	33681

Figure 3.8   (a) Modified Randles circuit model used to fit the EIS data. Table of averaged values of fitting parameters obtained by fitting the equivalent circuit to 25 individual EIS scans/cycles, obtained over a period of ~54 hours of testing.
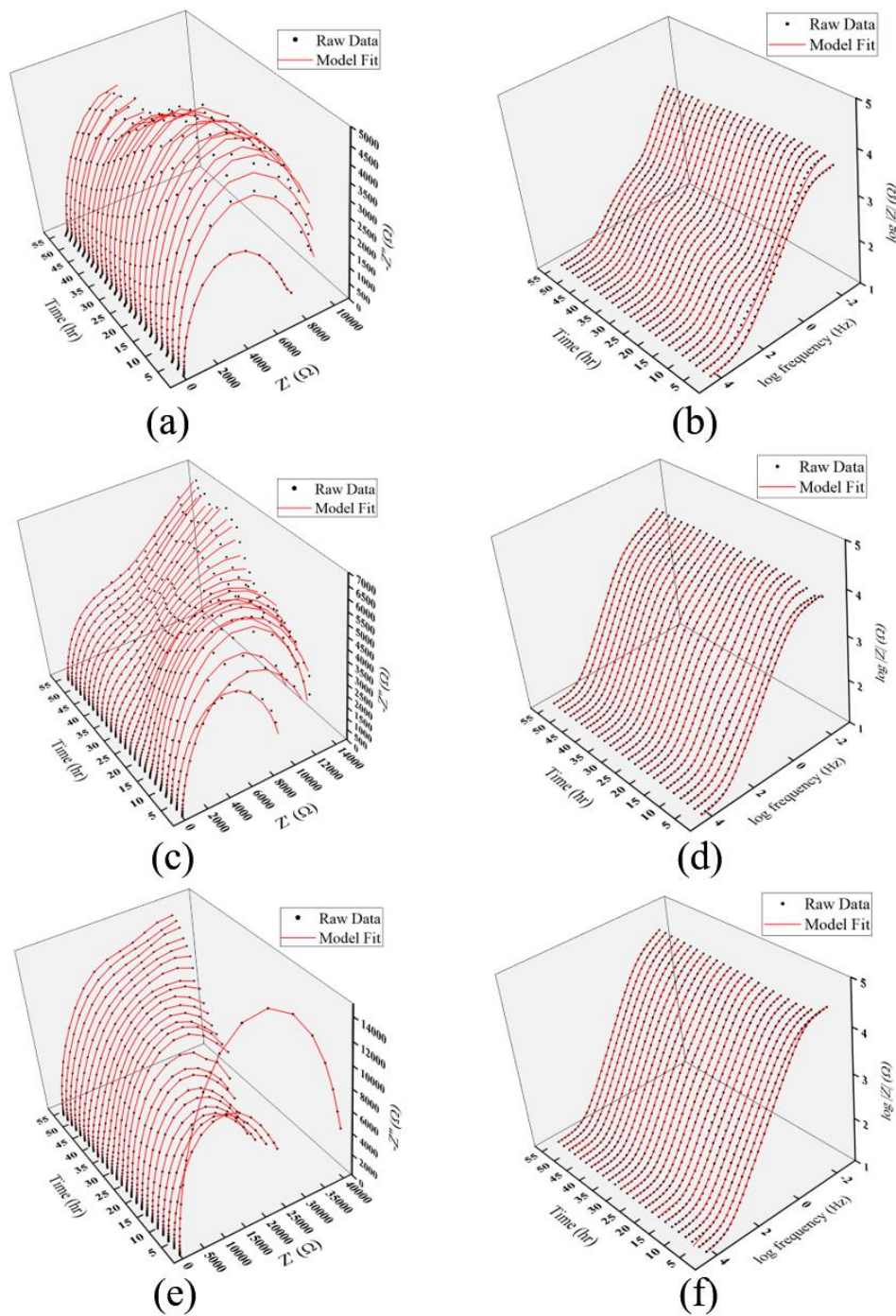
Figure 3.9   Representative EIS 3-D Nyquist and Bode impedance plots as a function of time with fitted data obtained by modeling via the equivalent circuit for P675-HTT (a,b), P675-LTT (c,d), and P675-CN (e,f) highlighting the difference in impedance behavior for each of the steels and overall good quality of the fit.
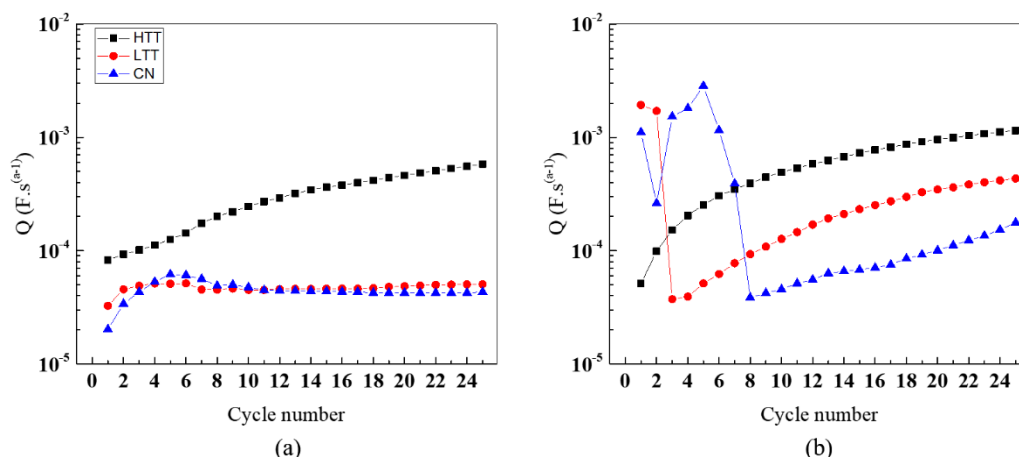
Figure 3.10   Averaged fitting parameters for P675-HTT, P675-LTT, and P675-CN as a function of time cycles (scans) for Q1(a) and Q3 (b) using the modified Randles equivalent circuit.Q1 represents the oxide layer and Q3 represents the overall matrix of the steel.
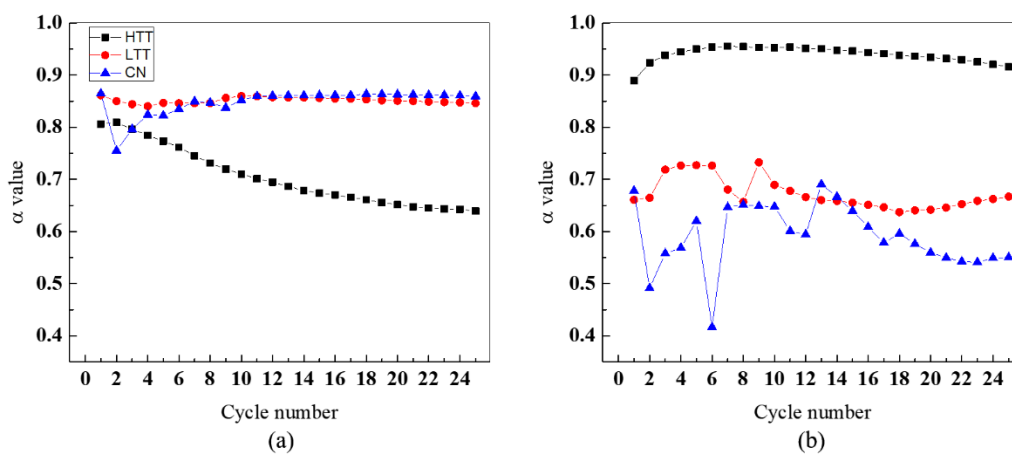
Figure 3.11   Averaged fitting parameters for P675-HTT, P675-LTT, and P675-CN as a function of time cycles (scans) for α1(a) and α3 (b) using the modified Randles equivalent circuit where α=1 is a pure capacitor and α=0 is a pure resistor. α1 represents the oxide layer of each steel and α2 represents the matrix of each steel.
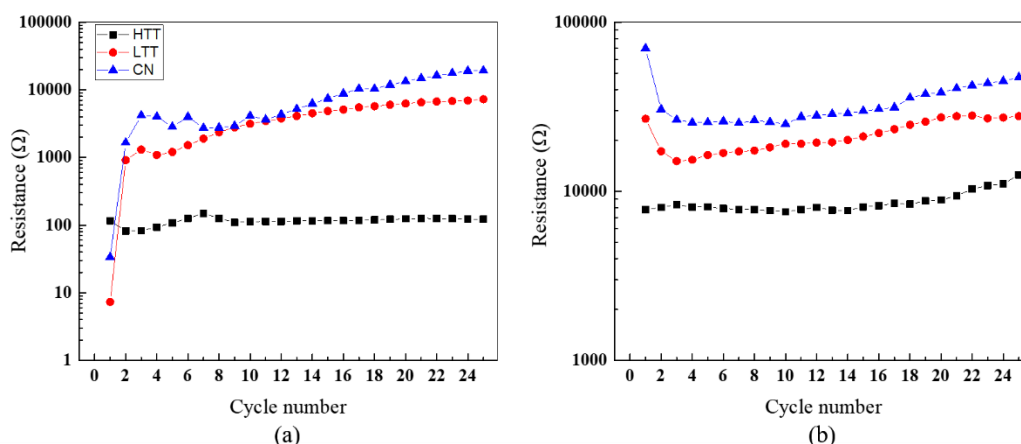
Figure 3.12   Averaged fitting parameters for P675-HTT, P675-LTT, and P675-CN as a function of time cycles (scans) for R2 (a) and R3 (b) using the modified Randles equivalent circuit. R2 represents the resistance of the oxide layer of each steel and R3 represents the resistance of the matrix of each steel.
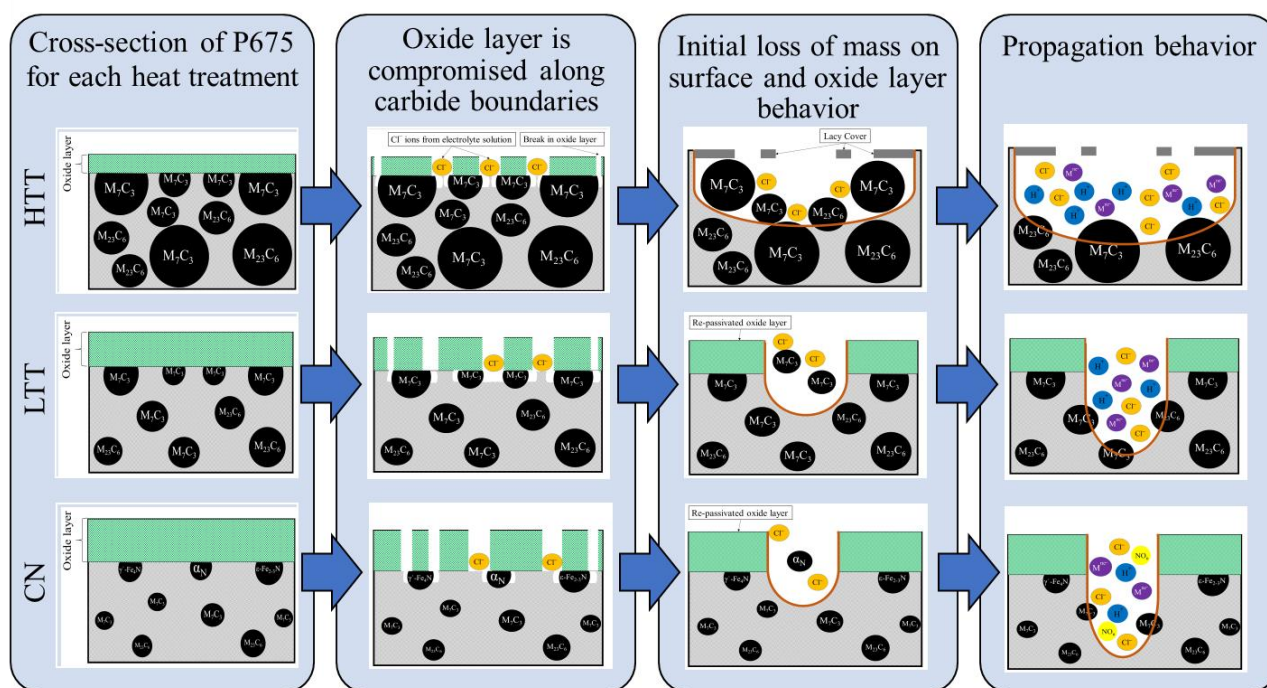
Figure 3.13   Cross-sectional schematic models highlighting differences in corrosion and degradation mechanism for the steels tested.
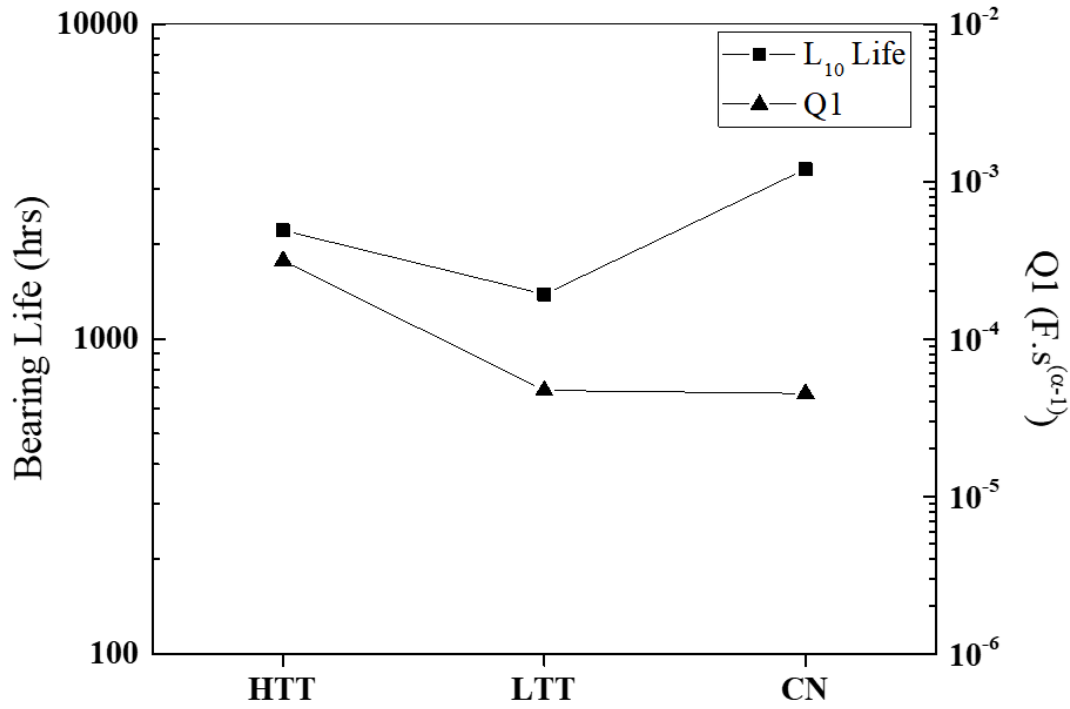
Figure 3.14   Bearing life (L10) and fitting parameter Q1 extracted from electrochemical testing (Figure 4.8).

Tables

Table 3.1   Nominal composition (wt%).

Steel	C	Mn	Cr	Mo	Si	Ni	S	V	Co
UNS 42670/ AMS 5930B (Pyrowear 675)	0.05-0.09	0.50-1.00	12.00-14.00	1.50-2.50	0.10-0.70	2.00-3.00	0.010	0.40-0.80	4.00-7.00

Table 3.2 **Probability of localized or general corrosion behavior for P675-HTT, P675-LTT, and P675-CN as determined via visual observation post electrochemical testing. Probabilities presented in the table were calculated using Equation 1 where n is the number of samples subject to the respective form of corrosion and N is the total number of electrochemical tests.**

Steel	Corrosion attack behavior	
	Localized	General
P675-HTT	0.08	0.92
P675-LTT	0.90	0.30
P675-CN	0.90	0.20

CHAPTER FOUR: MICROGALVANIC CORROSION BEHAVIOR OF CU-AG

ACTIVE BRAZE ALLOYS INVESTIGATED WITH SKPFM

This chapter is published by MDPI in the *Metals* journal and should be referenced

appropriately.

Reference:

Kvryan, A., Livingston, K., Efaw, C.M., Knori, K., Jaques, B.J., Davis, P.H., Butt, D.P.

and Hurley, M.F., 2016. Microgalvanic Corrosion Behavior of Cu-Ag Active Braze

Alloys Investigated with SKPFM. *Metals*, *6*(4), p.91.

Microgalvanic Corrosion Behavior of Cu-Ag Active Braze Alloys Investigated With SKPFM

Armen Kvryan[a]

Kari Livingston[b]

Corey M. Efaw[a]

Kyle Knori[a]

Brian Jaques[a]

Paul H. Davis[a]

Darryl P. Butt[a]

Michael F. Hurley[a]

[a]*Micron School of Materials Science & Engineering, Boise State University, Boise, ID 83725-2090*

[b]*Department of Mechanical & Biomedical Engineering, Boise State University, Boise, ID 83725-2085*

Author Roles

Author Contributions: Michael F. Hurley, Paul H. Davis and Darryl P. Butt conceived and designed the experiments; Corey M. Efaw, Armen Kvryan and Michael F. Hurley performed the experiments; Kari Livingston, Armen Kvryan, Paul H. Davis and Corey M. Efaw analyzed the data; Kyle Knori, Brian J. Jaques, Darryl P. Butt and Paul H. Davis contributed reagents, materials and analysis tools. All authors contributed to writing the paper.

Abstract

The nature of microgalvanic couple driven corrosion of brazed joints was investigated. 316L stainless steel samples were joined using Cu-Ag-Ti and Cu-Ag-In-Ti braze alloys. Phase and elemental composition across each braze and parent metal interface was characterized and scanning Kelvin probe force microscopy (SKPFM) was used to map the Volta potential differences. Co-localization of SKPFM with energy dispersive spectroscopy (EDS) measurements enabled spatially resolved correlation of potential differences with composition and subsequent galvanic corrosion behavior. Following exposure to the aggressive solution, corrosion damage morphology was characterized to determine the mode of attack and likely initiation areas. When exposed to 0.6 M NaCl, corrosion occurred at the braze-316L interface preceded by preferential dissolution of the Cu-rich phase within the braze alloy. Braze corrosion was driven by galvanic couples between the braze alloys and stainless steel as well as between different phases within the braze microstructure. Microgalvanic corrosion between phases of the braze alloys was investigated via SKPFM to determine how corrosion of the brazed joints developed.

Introduction

Failure, whether chemical or mechanical in nature, often occurs where dissimilar materials are joined together. Common joining techniques range from mechanical fastening (e.g., bolt or rivet) to solid state joining (e.g., diffusion bonding). Brazing is an alternative joining technique in which a filler material is heated so as to form metallurgical bonds with the surfaces of the parts (parent materials) being joined. Brazing is a relatively low temperature process wherein the filler (braze material) is heated to a temperature above its melting point but below that of the parent materials. Joints formed by brazing can achieve very tight tolerances and offer desirable mechanical properties, similar to diffusion bonded materials, but have the advantage of being easily disassembled [1].

Many different braze alloys are available—designed for specific applications. A braze that performs well mechanically may have limited utility based on environmental compatibility. For example, silver-based braze alloys typically have a lower corrosion rate in an industrial atmosphere than in a marine environment [2]. When used in settings where contact with certain types of fuel may occur, silver-based brazes have poor corrosion resistance that can ultimately lead to failure [3]. The effect of brazing on the corrosion behavior of the resultant parts (including parent materials) has not been widely investigated. Through gaining a better understanding of this vital relationship between brazing and its influence on corrosion behavior, it may be possible to optimize processing parameters and develop more effective brazes. Thus, it is important to understand the mechanism(s) that control the corrosion development at and near joints. Consequently,

the impact of brazing on the corrosion behavior of the overall system is investigated in this work.

<u>Background</u>

The Cu-Ag based systems investigated in this study were chosen because of their ease of application, commercial availability, and favorable compatibility with common engineering metals and technical ceramics. Good materials compatibility is due in part to effective wetting. Wetting, the ability of a liquid to maintain contact with a solid surface, is an important factor in the overall effectiveness of a braze [4]. The wetting parameter, or wettability, is the geometric complement of the contact angle, and thus is inversely related to the contact angle [5]. During brazing, good compatibility is achieved when the braze alloy wets the target material well. This ensures excellent surface coverage and any diffusion that occurs does not result in poor mechanical behavior. To promote wetting and joint compliance, reactive elements are added to brazing alloys [1]. The resultant brazing alloys are known as active brazing alloys (ABA). Titanium is often added to silver based braze alloys in order to enhance their ability to wet the parent material(s) being joined, which is vital when joining dissimilar materials, including ceramics [1]. In addition, an increased amount of titanium in brazes has been found to yield thicker joints [6]. In this study, commercially available Cu-Ag-Ti and Cu-Ag-In-Ti braze alloys were obtained and used to join 316L stainless steel samples. It should be noted that oxide layers on stainless steel, including 316L, can act as a barrier to wetting, resulting in lower degrees of wettability for the braze [7]. The indium additions (~12%) present in the Cu-Ag-In-Ti braze lower the metal surface tension [8]. Additionally, indium additions in a titanium-containing braze alloy increase activity of titanium and wettability [8,9].

In any joining technique, the joint must preserve mechanical integrity and environmental compatibility. Heat input and the introduction of dissimilar materials may provide initiation spots for pitting corrosion at microstructural heterogeneities, galvanic attack at the metal/braze interface, or dealloying within the braze material. Initially, corrosion within the braze alloy may cause loss of joint integrity and sustained braze corrosion may create an aggressive local chemical environment that can lead to depassivation of the parent material. Relatively low temperature brazing alloys typically rely on noble metals to provide good wetting behavior, adhesion, and joint compatibility. However, these alloys generally provide a thermodynamic driving force for galvanic corrosion when joined with the parent metal and are exposed to conditions that support active corrosion. Galvanic corrosion as the mechanism of failure for silver based brazes coupled to stainless steels was first proposed by Takemoto et al. [10].

Current research on the effect of brazing has mainly focused on compatibility and resultant mechanical behavior [11–14]. However, once a candidate braze has been identified, the reliability and resistance to environmental attack must be addressed to determine long-term viability. With the exception of a few isolated studies [15–18], the effect of brazing on corrosion behavior has received little attention in the open literature [18]. Because of the multicomponent aspect of brazes, a multiphase microstructure is usually seen post brazing where the two parent materials are joined [18]. This is mainly due to precipitation of stable or meta-stable phases during the brazing cycle [16]. Once these phases are present, they would be expected to have different electrochemical behavior based on composition. The local potential difference between dissimilar regions in the microstructure will influence corrosion behavior, and is known as microgalvanic

corrosion. The term microgalvanic corrosion describes a galvanic corrosion cell occurring on a sub-grain scale. Regions of varying composition result in potential differences amongst the individual phases in the braze, and tend to increase the corrosion rate of the less noble phases [16]. The concept of microgalvanic corrosion is important to joint reliability, as manipulations of the filler metal in the braze can dramatically influence the overall corrosion behavior of a braze [19].

Confirmation of a microgalvanic corrosion mechanism requires accurate characterization of the surface of the materials, both in terms of composition and electrochemical potential. Scanning Kelvin probe force microscopy (SKPFM) has been shown to be an effective technique to characterize expected electrochemical behavior of surface inhomogeneities within a metal alloy's microstructure [20]. A Kelvin probe measures the work function difference (Volta potential) between the surface of a sample and the probe itself. Correlation between the Volta potential difference (VPD) obtained via SKPFM and electrode solution potentials, and hence the likely development of galvanic couples during active corrosion conditions has previously been established [21]. However, this relationship should be approached with some caution for unconfirmed systems. SKPFM is a surface technique and sensitive to the formation of surface reaction products such as oxide layers that may influence the measurement, and thus may not always directly correlate with solution potential. However, by using an atomic force microscope (AFM) with surface potential feedback and nullification, SKPFM is able to map Volta potential differences on a surface with extremely fine (sub-micron) resolution. Compared to other local techniques, SKPFM currently provides the highest achievable spatial resolution for studying corrosion initiation driven by microstructure

inhomogeneities. This paper utilized SKPFM to analyze and characterize the VPD between the different metallic/intermetallic phases present within the brazes studied. This method was used to investigate and explain corrosion initiation and propagation driven by galvanic corrosion arising from compositional differences within brazing alloys used to join 316L stainless steel.

Materials and Methods

Materials and Joining Procedure

Commercial 316L stainless steel sheet with a thickness of 3 mm was water-jet cut into disk shaped samples of various sizes to be brazed. The braze alloys used were Cu-Ag-Ti-ABA with a thickness of approximately 50 μm and Cu-Ag-In-Ti-ABA with a thickness of 55 μm. Compositions of all materials are listed in Table 4.1. Stainless steel disks were polished to a 1 μm finish with SiC polishing pads. The as-received Cu-Ag-Ti and Cu-Ag-In-Ti foils were lightly polished to an 800 grit finish and cut to sizes just smaller than the stainless steel disks. After polishing, all samples were ultrasonically cleaned in ethanol for 15 min, washed in deionized water, and dried using compressed air.

Two geometrical configurations were used during brazing: sandwich (stainless steel/braze foil/stainless steel) and coated (braze foil on stainless steel disk). Prior to firing, the cleaned and polished samples were placed in an alumina boat wrapped in niobium foil and inserted into the furnace hot zone. The system was then purged with ultra-high purity argon gas (UHP Ar, 99.999%, Norco, Boise, ID, USA) for 20 min before continuously flowing with oxygen gettered UHP Ar. Stainless steel joining with Cu-Ag-Ti was achieved through the following thermal cycle suggested by the supplier:

ramp to 700 °C (80 °C below the solidus temperature of Cu-Ag-Ti) at 5 °C/min and hold

for 20 min before ramping to 830 °C (15 °C above the liquidus temperature of Cu-Ag-Ti

braze alloy) at a rate of 5 °C/min and held there for 15 min. The furnace was then cooled

to room temperature at a rate of 5 °C/min. To create Cu-Ag-In-Ti joints, the furnace was

ramped from room temperature to a temperature of 500 °C (130 °C below the solidus

temperature of Cu-Ag-In-Ti) at a rate of 5 °C/min and held for 20 min, followed by a

ramp to 730 °C (15 °C above the liquidus temperature of Cu-Ag-In-Ti) at a rate of 5

°C/min and held for 15 min, then cooled at a rate of 5 °C/min to room temperature, again

as per the supplier recommendation.

<u>Scanning Kelvin Probe Force Microscopy (SKPFM) of Brazed Regions</u>

For SKPFM, brazed samples were cross sectioned, cold mounted in epoxy, and

polished with progressively finer grit silicon carbide pads and diamond slurries starting

with 400 grit and ending with a 1 μm diamond slurry. Next, the samples were cleaned

ultrasonically in a bath of non-denatured (200 proof) High Performance Liquid

Chromatography (HPLC)/spectrophotometric grade ethanol (Sigma-Aldrich, St. Louis,

MO, USA). The final polishing step employed a VibroMet 2 vibratory polisher (Buehler,

Lake Bluff, IL, USA) in which samples were polished for 1 h using a 12" Mastertex PSA

pad (Buehler) covered with a 0.50 μm diamond slurry (MasterPrep Polishing Solution,

Buehler). The polished samples were then rinsed with ethanol and blown dry with

compressed air. Prior to imaging, an electrical connection between the sample surface

and the AFM stage was established using colloidal silver paint and verified with a

voltmeter. Imaging was conducted using a Bruker Dimension Icon AFM operating in

frequency modulation Peak Force KPFM (FM PF-KPFM) mode with a PFQNE-AL

probe (Bruker, Santa Barbara, CA, USA). PF-KPFM is a dual-pass method wherein the first pass acquires topography via Peak Force tapping (i.e., rapid force curves). The second pass is then used to measure the tip-sample surface potential difference at a user-determined fixed lift height above the sample surface. The SKPFM technique and important experimental considerations have been described in greater detail previously [22], but lift heights of ~100 nm and a frequency modulation based detection scheme were employed. To enhance signal to noise and minimize the effects of residual sample roughness on the surface potential image, a slow scan rate was used (~0.05–0.1 Hz). Because SKPFM measures the difference in work function between the AFM probe and the sample surface (i.e., the relative rather than absolute surface potential), potentials of the different phases are reported relative to each other. Absolute potentials can be determined; e.g., using an inert gold standard as a reference material.

Braze Phase Composition

A Scanning electron microscope (SEM) (Hitachi S-3400N-II, Hitachi, Tokyo, Japan) equipped with energy dispersive spectroscopy (EDS) capabilities was used to image and analyze the mounted braze joint cross-sections for both Cu-Ag-Ti and Cu-Ag-In-Ti alloys after SKPFM characterization. Performing SEM after SKPFM was to avoid effects of electron beam irradiation on the surface potential measured. The cross section of each braze alloy was imaged in both secondary electron mode and backscatter electron mode. Subsequently, elemental mapping was performed on the cross sections of each sample, along with multi-point analysis at selected locations.

<u>Corrosion Testing</u>

To assess corrosion behavior electrochemical and exposure testing in 0.6 M NaCl solution at room temperature (22–24 °C) was conducted. Potentiodynamic testing was performed on both the braze alloys and stainless steel samples separately following thermal treatment using the prescribed brazing furnace profile. The braze alloy samples were prepared by applying multiple coatings of either the foil or paste braze compound to one face of a stainless steel coupon. Multiple braze coatings ensured that only the braze material was exposed to solution when tested, with no impact from the underlying stainless steel possibly present at the pinholes that may occur with a single coating. A conventional 3-electrode cell with a Pt mesh counter electrode and a saturated calomel (SCE) reference electrode was used for potentiostat controlled polarization measurements.

Results

<u>Brazed Stainless Steel Joint Characterization</u>

Metallographic samples of the post-braze joint cross-section were examined via SEM in order to characterize the resulting joint (Figure 4.1). The joints formed a clean, tight, hermetic seal with the parent 316L samples. Both brazes were approximately 50 μm in width and displayed distinctive eutectic type phases in the braze region following the prescribed thermal cycles.

EDS line scans are presented in Figure 4.2 (Cu-Ag-Ti) and Figure 4.3 (Cu-Ag-In-Ti) below. The Cu-Ag-Ti braze had a Ag-rich matrix with numerous distributed regions, generally ~1–10 μm across, of a precipitated Cu-rich phase. Generally, the EDS results did not indicate noticeable diffusion of the braze filler materials into the stainless steel.

However, in a few areas the EDS scans indicated some transport of the braze alloy elements into the stainless steel, resulting in a Ti and Ag-containing region adjacent to the braze for the Cu-Ag-Ti braze sample. It was also observed that that the bulk of the titanium in the braze segregated to one side of the braze/stainless steel interface (Figure 4.2). The Cu-Ag-In-Ti braze phase structure consisted of an Ag-In-rich matrix phase with numerous regions of a precipitated Cu-rich phase. Ti was also found to be present in some of the Cu-rich regions.

Phase separation within the braze regions was further characterized via optical microscopy to aid with identification of the various phases present when initiating SKPFM scans. Optical images obtained of the Cu-Ag-Ti and Cu-Ag-In-Ti braze areas showed clear variation of phase composition within the braze, with uniform 316L stainless steel on either side (Figure 4.4). The identical sample regions seen in Figure 4.4 were also characterized and discussed later in this paper.

In order to obtain semi-quantitative compositions of the phases, EDS multi point scans were acquired for both Cu-Ag-Ti and Cu-Ag-In-Ti samples. Multiple spectra were taken at representative points within the individual phase regions of each sample. The average composition values in atomic percent obtained for each phase present are listed in the tables adjacent to the respective images (see Figure 4.4). The Cu-Ag-Ti sample had a standard deviation below 3, whilst the Cu-Ag-In-Ti had a standard deviation below 5. For the Cu-Ag-Ti braze alloy, two primary phases, composed primarily of either copper or silver, dominate the microstructure of the braze in agreement with previous findings [8]. This bead-like microstructure develops with overall low solubility of titanium within the Cu-Ag-Ti braze. Titanium was not detected in the eutectic phases, but was instead

found along the interface between the braze and parent stainless steel metal [8]. Additionally, some titanium diffused into the neighboring stainless steel. This was also observed in previous research, and is attributed to the lack of both titanium solubility within the braze and miscibility within the adjacent stainless steel, leading to near-complete segregation [8,23]. In contrast, three distinct phases were observed in the Cu-Ag-In-Ti brazed joint. Also, segregation of the titanium to the interface was suppressed. Ti content varied in and near regions where a distinct Cu-Ti phase was observed (Figure 4.4b) and suggested incomplete phase transformation. The Cu-Ti rich phase present was likely the Cu_4Ti intermetallic phase [23,24].

Corrosion Behavior of Brazed Joints

Electrochemical Testing of Braze Materials

Representative polarization curves from Cu-Ag-Ti (blue trace) and Cu-Ag-In-Ti (green trace) braze alloys are presented in Figure 4.5. Polarization data obtained from a bare 316L coupon (red trace) is also included in Figure 4.5 for comparison. The two different braze alloys displayed nearly identical polarization behavior. The braze alloys exhibited normal Tafel behavior indicative of activation polarization control with an corrosion rate, i_{corr} (at open circuit) of approximately $1 \times 10{-}5$ Amps/cm^2, approximately two orders of magnitude greater than the i_{corr} of passive 316L. Moreover, the E_{corr} (corrosion potential) of the braze alloys was approximately 50 mV less than that of 316L, −0.16 V vs. SCE.

To determine any effect the thermal braze cycle might have on the inherent corrosion behavior of 316L, polarization curves were conducted on bare 316L samples that had been fired according to the braze cycle mentioned in the experimental section. When compared to the unfired stainless steel, the fired stainless steel sample displayed a

much smaller passive region with pitting occurring at approximately 0.05 V vs. SCE

(Figure 4.6). The pitting potential, or potential at which pitting corrosion occurs, was

seen when a sharp increase in current occurred upon increasing potential. The pitting

potential of the fired sample was significantly lower than the unfired 316L sample, likely

due to grain boundary sensitization [25]. The effect on localized corrosion behavior could

be expected since the sample was held in the sensitization range for approximately 35

min. Optical microscopy of the pitted surface (not shown here) revealed grain boundary

attack had occurred at areas adjacent to pits on the fired sample. In contrast, pits on the

unfired sample did not show evidence of preferential grain boundary attack near the pit

openings, confirming some degree of sensitization on the 316L sample as a result of the

thermal braze cycle.

<u>Exposure Testing at Open Circuit Potential</u>

Exposure testing was conducted to observe macroscopic corrosion propagation

behavior of the braze alloy and stainless steel at the free corrosion potential under natural,

galvanic coupling conditions. Circular braze foil coupons were fabricated such that the

foil occupied approximately 80% of the exposed surface area of the polished face of the

316L disk. Following firing, the coated samples and an untreated 316L control sample

were immersed in 0.6 M NaCl solution and the samples were observed periodically to

monitor corrosion progression, as shown in Figure 4.7.

The 316L control sample (not shown) did not display evidence of depassivation or

production of any significant corrosion products for the duration of testing (166 days, or

~24 weeks). However, after only 22 days of immersion both of the braze foil coated

samples showed evidence of macroscale corrosion damage (Figure 4.7). Visual

observation revealed that corrosion was limited to the braze foil surface, while the remaining uncoated area of the 316L sample appeared unaffected. While the extent of the corrosion damage was not quantified, the presence of blue-green corrosion reaction products covering both the Cu-Ag-Ti and Cu-Ag-In-Ti foil surfaces suggested preferential corrosion of the Cu-rich phase present in each braze alloy [14]. Moreover, both samples also exhibited regions of dark red corrosion products deposited within the foil-coated region toward the end of the test duration. It is suspected these corrosion products were iron oxide-hydroxides generated from the underlying stainless steel which had become exposed following corrosion perforation of the braze foil coating.

SKPFM Measurements

SKPFM was used to measure Volta potential differences (VPD) among the various phases present on the surface of the brazed region of the stainless steel joint. SKPFM measurements were obtained prior to SEM/EDS characterization of the same regions on both braze alloy joints to avoid any effect of electron irradiation on surface potential measurements [22,26,27]. Potential maps acquired from SKPFM coupled with composition maps obtained from SEM/EDS clearly showed that the observed variations in potential correlated with changes in composition within the braze regions (Figures 4.8 and 4.9).

From the SKPFM VPD data, there is a clear difference in potential values between the two primary phases for the Cu-Ag-Ti braze sample, with the Ag-rich phase as the brighter or more noble area, and the Cu-rich phase darker (more active potential). The Volta potential observed for the stainless steel outside the braze region was more negative than either of the braze phases (Figure 4.8b). These differences are expected

based solely on composition, and the difference promotes dissimilar metal, galvanic couple driven corrosion within the braze alloy. Similar results were obtained on the Cu-Ag-In-Ti sample, with the most noble phase being the Ag-rich phase. The most active braze phase is the Cu-Ti rich phase, while the Volta potential of the Cu-rich phase falls in between the two. The surrounding stainless steel was similar to the Ti-Cu rich phase (Figure 4.9).

Discussion

Research on braze reliability has largely focused on evaluating mechanical integrity of the joint [11–14]. Accordingly, corrosion behavior of brazes has received little attention in the open literature. The limited studies available focusing on stainless steel have considered different Ag-based braze compositions than studied here, but the systems behaved similarly and it was proposed that galvanic cells developed at the braze-stainless steel interface promoting corrosion driven by the electrically connected dissimilar metals [10,15–18,28]. However, in these studies, local galvanic couple corrosion was only postulated from bulk corrosion observations, it was not directly confirmed as in the present work with SKPFM. Other studies observed that partitioning of more noble alloying elements (preferred cathode sites) within the braze alloy occurred, causing depletion in the surrounding matrix and likely lead to preferential corrosion in those regions. In the systems investigated herein, similar corrosion behavior was confirmed [15–17]. Visual observation of corrosion propagation on braze alloy-stainless steel couples (Figure 4.7) showed that active corrosion rapidly initiated on the braze alloy first, with the surrounding uncoated stainless steel unaffected. The polarization curves presented in Figure 4.5 also suggest that the more anodic braze alloy will be

preferentially attacked at an increased corrosion rate when galvanically connected to the more noble stainless steel cathode. Stainless steel had an open circuit potential (OCP) approximately 50 mV more noble that either of the braze alloys alone. On a macroscale, the stainless steel acts as cathode when galvanically coupled to the more anodic braze alloys, driving preferential corrosion of the braze alloy. This galvanic couple situation is particularly detrimental for joint integrity because of the typically large cathode (stainless steel) to anode (braze alloy) area ratio. At free corrosion conditions the anodic reaction occurring on the braze alloy is polarized towards the stainless steel, further accelerating the anodic reaction rate of the braze alloy. Because of the large cathode to anode area ratio there is ample cathode area available to support the increased dissolution rate of the braze, leading to eventual loss of joint integrity.

Following initiation, during corrosion propagation, the stainless steel also becomes susceptible to corrosion degradation near the braze interface, which is a further detriment to joint integrity. Corrosion attack on a 316L coupon with a foil braze coating on the surface showed that the copper phase was preferentially attacked, and the presence of the braze alloy served as a crevice former under which localized corrosion was able to propagate into the stainless steel (Figure 4.10). In Figure 4.10, the samples were exposed for 7 days to 0.6 M NaCl at OCP followed by a potentiodynamic scan from open circuit to 0.5 V vs. SCE, prior to cleaning and cross sectioning. The left image (Figure 4.10) was obtained from a cross section that bisected a corrosion pit which grew and propagated underneath the braze alloy coating. Eventual corrosion attack of the stainless steel in a brazed sample was also observed during free corrosion conditions when immersed in 0.6 M NaCl solution. As seen in Figure 4.7, the generation of voluminous dark red corrosion

products indicated that braze alloy corrosion likely generated a sufficiently aggressive local chemical environment to depassivate the underlying stainless steel. While the uncoated regions of the stainless steel coupon did not display evidence of corrosion damage, it is evident that the galvanically driven braze alloy corrosion led to subsequent corrosion attack of the joined stainless steel at the interface for both braze alloys considered.

For the Cu-Ag-Ti braze alloy, corrosion caused by segregation of Ti to the braze-stainless steel interface (Figure 4.8) could also promote loss of joint coherency. The image on the right in Figure 4.10 shows preferential corrosion attack on the Cu-rich phase of the braze alloy and an area of corrosion damage along the 316L and Cu-Ag-Ti coating interface. The behavior of Ti was similar to that observed in literature [2] and can be attributed to the strong interfacial reactions between the Cu and Ti found in the braze [5]. The addition of In in the Cu-Ag-In-Ti samples did not support Ti segregation to the joint interface, and hence would be expected to be beneficial to joint integrity.

In addition to the macroscale galvanic couple between braze alloys and stainless steel, both braze alloys formed multiple distinct phases following thermal treatment, resulting in microgalvanic cells between phases during active corrosion conditions. Open circuit potentials obtained from potentiodynamic polarization testing of both braze alloys were intermediate to those listed in the galvanic series for seawater for pure copper and pure silver [15,29]. Based on the galvanic series, the measured OCP of the bulk two phase (copper-rich and silver-rich) braze structure is in agreement with what would be expected from mixed potential theory. Within the braze alloy the expected electrode potential difference implies that when corrosion occurs, the Cu-rich phase of the braze

alloy will be anodic to the more noble Ag-rich phase and suffer from preferential microgalvanic attack, even in the absence of a stainless steel couple.

The nature of microgalvanic corrosion within the braze alloys was further investigated with SKPFM. The goal of using SKPFM was to measure Volta potential differences between phases within the microstructure to determine relative nobility of the individual phases. Schmutz and Frankel, along with Leblanc, have established a direct correlation between Volta potentials measured in air and respective solution potentials of metals [26,27,30]. Importantly, the VPD observed was an effective indicator of how corrosion developed due to microstructural features. Subsequent to these findings, several research groups [31–39] have been able to verify that SKPFM is both reliable and effective in characterizing various alloy systems to accurately explain corrosion initiation behavior.

Galvanic corrosion on the microscale strongly influenced corrosion within the braze alloys. As determined via SKPFM, within the Cu-Ag-Ti braze, the Ag-rich phase was the most noble, followed by the Cu-rich phase, and finally stainless steel had the lowest overall potential (see Figure 4.11a, Table 4.3). For the Cu-Ag-In-Ti braze, the Ag-rich phase is the most noble, followed by the Cu-rich phase, then the Ti-Cu rich phase, as in Figure 4.12a,b and Table 4.4. The approximate average Volta potentials differences between phases in both braze alloys are presented in Tables 4.3 and 4.4 with corresponding images of the SKPFM images of the brazes in Figures 4.11 and 4.12, respectively. The SKPFM data presented in Figures 4.11 and 4.12 are from identical areas characterized with SEM/EDS (Figures 4.8 and 4.9). The co-localization of SKPFM and SEM/EDS techniques at the identical area provides direct evidence of the influence

of local composition on Volta potential. Hence, in addition to the galvanic couple between the braze and stainless steel, variations in composition between phases provided the basis for microgalvanic corrosion within the braze alloys studied.

Interestingly, SKPFM results showed the stainless steel surface had an average Volta potential that was less noble than any of the braze phases measured (Figures 4.11 and 4.12). This is contrary to the known and observed corrosion behavior, in that corrosion preferentially occurs within the braze alloy, with the coupled stainless steel acting as a cathode in the galvanic couple (Figures 4.5 and 4.7). This finding is important because it highlights an instance where caution must be exercised when inferring electrochemical behavior from Volta potential measurements. In the case of stainless steel, the presence of a protective passive oxide layer makes it an ineffective anode, and the resulting solution potential is more noble than the braze material. Hence, it is essential to verify expected relative nobility obtained from SKPFM measurements with the observed corrosion and electrochemical behavior in solution, as done here.

Conclusions

The composition, phase separation, surface potential differences, and corrosion behavior of Cu-Ag braze alloys (Cu-Ag-Ti and Cu-Ag-In-Ti) and the joined material (316L) were investigated and correlated. SKPFM measurements provided new insight to the origins of microgalvanic corrosion within the brazed region and confirmed the manner that corrosion develops, which previously had only been postulated to explain bulk corrosion observations of brazed joints. Significant findings include:

(1) Co-localized SKPFM and SEM/EDS provided evidence of phase separation within the braze regions that resulted in surface potential differences. Moreover, the

measured surface potentials correlated with the observed microgalvanic corrosion behavior, thereby highlighting the utility of combining these methods for the future study, prediction, and prevention of microgalvanic corrosion.

(2) Microgalvanic cells were confirmed via SKPFM VPD values. The two phases present in the Cu-Ag-Ti braze alloy samples differed by ~60 mV in surface potential, while the Cu-Ag-In-Ti samples exhibited a range in surface potential differences up to ~250 mV across three phases.

(3) Electrochemical testing on the individual materials was used to verify expected galvanic behavior. Stainless steel exhibited passive behavior and had an OCP that was noble to either of the braze alloys, which exhibited active corrosion behavior and i_{corr} approximately two orders of magnitude larger than stainless steel. The role of stainless steel in the direction of the galvanic couple was in conflict with that expected from SKPFM measurements and provided an exceptional case where SKPFM Volta potential did not correlate with solution potential.

(4) Exposure testing of stainless steel samples coated with each braze alloy were conducted at OCP in 0.6 M NaCl. It was found the braze alloy undergoes active corrosion that induces accelerated attack on the underlying 316L material. Additionally, it was seen that the Cu-rich phase of the braze alloy underwent preferential attack compared to the Ag-rich phase and corrosion propagation in the braze alloy was aggressive enough to depassivate the adjacent 316L stainless steel.

(5) The thermal brazing cycle caused sensitization of the 316L parent material and resulted in grain boundary attack and a pitting potential that was approximately 200 mV more negative than the unfired 316L.

References

1. Jacobson, David M., and Giles Humpston. *Principles of brazing*. ASM International, 2005.

2. Dev, S. C., et al. "Corrosion behaviour of silver brazing alloys in different environments." *Anti-Corrosion Methods and Materials* 44.4 (1997): 260-264.

3. Dimatteo, A., et al. "Compatibility of nickel and silver-based brazing alloys with E85 fuel blends." *Materials and Corrosion* 66.2 (2015): 158-168.

4. Shafrin, Elaine G., and William A. Zisman. "Constitutive relations in the wetting of low energy surfaces and the theory of the retraction method of preparing monolayers1." *The Journal of Physical Chemistry* 64.5 (1960): 519-524.

5. Dezellus, Olivier, and N. Eustathopoulos. "Fundamental issues of reactive wetting by liquid metals." *Journal of Materials Science* 45.16 (2010): 4256-4264.

6. Paiva, O. C., and Mário A. Barbosa. "Microstructure, mechanical properties and chemical degradation of brazed AISI 316 stainless steel/alumina systems." *Materials Science and Engineering: A* 480.1-2 (2008): 306-315.

7. Kozlova, O., et al. "Wetting and brazing of stainless steels by copper–silver eutectic." *Materials Science and Engineering: A* 495.1-2 (2008): 96-101.

8. Abed, Abdulrahman, Issam S. Jalham, and Alan Hendry. "Wetting and reaction between β′-sialon, stainless steel and Cu–Ag brazing alloys containing Ti." *Journal of the European Ceramic Society* 21.3 (2001): 283-290.

9. Nicholas, M. G., T. M. Valentine, and M. J. Waite. "The wetting of alumina by copper alloyed with titanium and other elements." *Journal of Materials Science* 15.9 (1980): 2197-2206.

10. Takemoto, T., and I. Okamoto. "Effect of Composition on the Corrosion Behavior of Stainless Steels Brazed with Silver-Base Filler Metals." *Welding Research Supplement* (1984): 300.

11. Lee, Jung G., et al. "High strength bonding of titanium to stainless steel using an Ag interlayer." *Journal of Nuclear Materials* 395.1-3 (2009): 145-149.

12. Liu, C. C., C. L. Ou, and R. K. Shiue. "The microstructural observation and wettability study of brazing Ti-6Al-4V and 304 stainless steel using three braze alloys." *Journal of Materials Science* 37.11 (2002): 2225-2235.

13. Singh, M., T. P. Shpargel, and R. Asthana. "Brazing of Stainless Steel to Yttria-Stabilized Zirconia Using Gold-Based Brazes for Solid Oxide Fuel Cell

Applications." *International journal of applied ceramic technology* 4.2 (2007): 119-133.

14. Singh, Mrityunjay, Tarah P. Shpargel, and Rajiv Asthana. "Brazing of yttria-stabilized zirconia (YSZ) to stainless steel using Cu, Ag, and Ti-based brazes." *Journal of materials science* 43.1 (2008): 23-32.

15. Anastasio, S., et al. "Corrosion of superaustenitic stainless steel N08367 brazed with a nickel-chromium-silicon-phosphorous alloy: Electrochemical corrosion behavior of isolated and combined materials." *Corrosion* 65.6 (2009): 388-403.

16. James, J. P., F. Bocher, and J. R. Scully. "Effect of braze clearance on localized corrosion of a superaustenitic stainless steel brazed with a Ni-based alloy (Ni-22Cr-6.3 Si-3.8 P)." *Corrosion* 65.8 (2009): 511-526.

17. Sorensen, N. R. "The Environmentally Assisted Failure of Cusil in Mattsson's Solution." *Corrosion* 42.5 (1986): 299-306.

18. Lee, M. K., et al. "Phase-dependent corrosion of titanium-to-stainless steel joints brazed by Ag–Cu eutectic alloy filler and Ag interlayer." *Journal of Nuclear Materials* 439.1-3 (2013): 168-173.

19. Chiu, L. H., C. H. Wu, and H. Chang. "Galvanic corrosion on vacuum-brazed UNS S31803 duplex stainless steel using Ni-Cr-Fe-P alloy filler metals." *Corrosion* 63.2 (2007): 127-134.

20. Guillaumin, V., P. Schmutz, and G. S. Frankel. "Characterization of corrosion interfaces by the scanning Kelvin probe force microscopy technique." *Journal of the electrochemical society* 148.5 (2001): B163-B173.

21. Schmutz, P., and G. S. Frankel. "Corrosion study of AA2024-T3 by scanning kelvin probe force microscopy and in situ atomic force microscopy scratching." *Journal of the Electrochemical Society* 145.7 (1998): 2295-2306.

22. Hurley, M. F., et al. "Volta potentials measured by scanning kelvin probe force microscopy as relevant to corrosion of magnesium alloys." *Corrosion* 71.2 (2014): 160-170.

23. Yue, Xin, et al. "Microstructure and interfacial reactions of vacuum brazing titanium alloy to stainless steel using an AgCuTi filler metal." *Materials characterization* 59.12 (2008): 1721-1727.

24. Elrefaey, A., and W. Tillmann. "Effect of brazing parameters on microstructure and mechanical properties of titanium joints." *Journal of materials processing technology* 209.10 (2009): 4842-4849.

25. Jones Denny, A. "Principles and prevention of corrosion." *Upper Saddle River, NJ, USA, Pearson-Prentice Hall* (1992).

26. Schmutz, P., and G. S. Frankel. "Characterization of AA2024-T3 by scanning Kelvin probe force microscopy." *Journal of the Electrochemical Society* 145.7 (1998): 2285-2295.

27. Schmutz, P., and G. S. Frankel. "Influence of dichromate ions on corrosion of pure aluminum and AA2024-T3 in NaCl solution studied by AFM scratching." *Journal of the Electrochemical Society* 146.12 (1999): 4461-4472.

28. Chiu, L. H., W. C. Hsieh, and Y. C. Ling. "Effect of vacuum brazing on corrosion resistance of UNS S31803 and UNS S31200 duplex stainless steels." *Corrosion* 58.9 (2002): 797-803.

29. Forman, Charles M., and E. A. Verchot. "Practical galvanic series". *No. RS-TR-67-11*. Army Missile Command Redstone Arsenal Al Systems Research Directorate, 1967.

30. Leblanc, P., and G. S. Frankel. "A study of corrosion and pitting initiation of AA2024-T3 using atomic force microscopy." *Journal of the Electrochemical Society* 149.6 (2002): B239-B247.

31. Jia, J. X., et al. "Simulation of galvanic corrosion of magnesium coupled to a steel fastener in NaCl solution." *Materials and Corrosion* 56.7 (2005): 468-474.

32. De Wit, J. H. W. "Local potential measurements with the SKPFM on aluminium alloys." *Electrochimica Acta* 49.17-18 (2004): 2841-2850.

33. Campestrini, P., et al. "Relation between microstructural aspects of AA2024 and its corrosion behaviour investigated using AFM scanning potential technique." *Corrosion Science* 42.11 (2000): 1853-1861.

34. Lacroix, Loïc, et al. "Combination of AFM, SKPFM, and SIMS to study the corrosion behavior of S-phase particles in AA2024-T351." *Journal of the Electrochemical Society* 155.4 (2008): C131-C137.

35. Femenia, M., et al. "Scanning Kelvin probe force microscopy and magnetic force microscopy for characterization of duplex stainless steels." *Journal of The Electrochemical Society* 150.6 (2003): B274-B281.

36. Sathirachinda, Namurata, Rachel Pettersson, and Jinshan Pan. "Depletion effects at phase boundaries in 2205 duplex stainless steel characterized with SKPFM and TEM/EDS." *Corrosion Science* 51.8 (2009): 1850-1860.

37. Sathirachinda, Namurata, et al. "Scanning Kelvin probe force microscopy study of chromium nitrides in 2507 super duplex stainless steel—Implications and limitations." *Electrochimica Acta* 56.4 (2011): 1792-1798.

38. Mato, S., et al. "Corrosion behaviour of a Ti-base nanostructure-dendrite composite." *Electrochimica acta* 50.12 (2005): 2461-2467.

39. Afshar, F. Norouzi, et al. "Scanning Kelvin probe force microscopy as a means of predicting the electrochemical characteristics of the surface of a modified AA4xxx/AA3xxx (Al alloys) brazing sheet." *Electrochimica Acta* 88 (2013): 330-339.

Figures

(a)   (b)
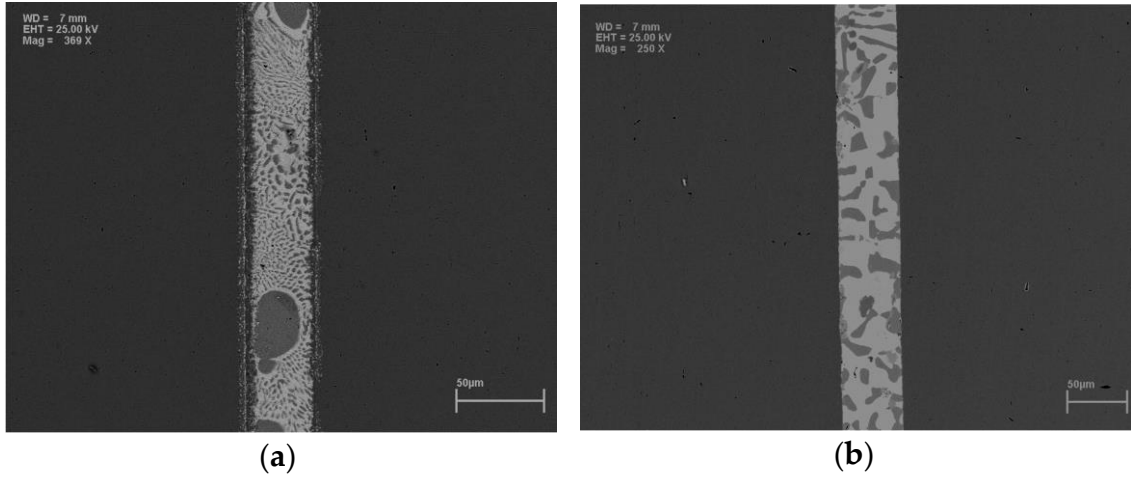
Figure 4.1   Scanning Electron Microscopy (SEM) images of cross sections of the resultant braze joint between two stainless steel 316L samples joined using: Cu-Ag-Ti (a) and Cu-Ag-In-Ti (b) braze alloys.

(a)

(b)
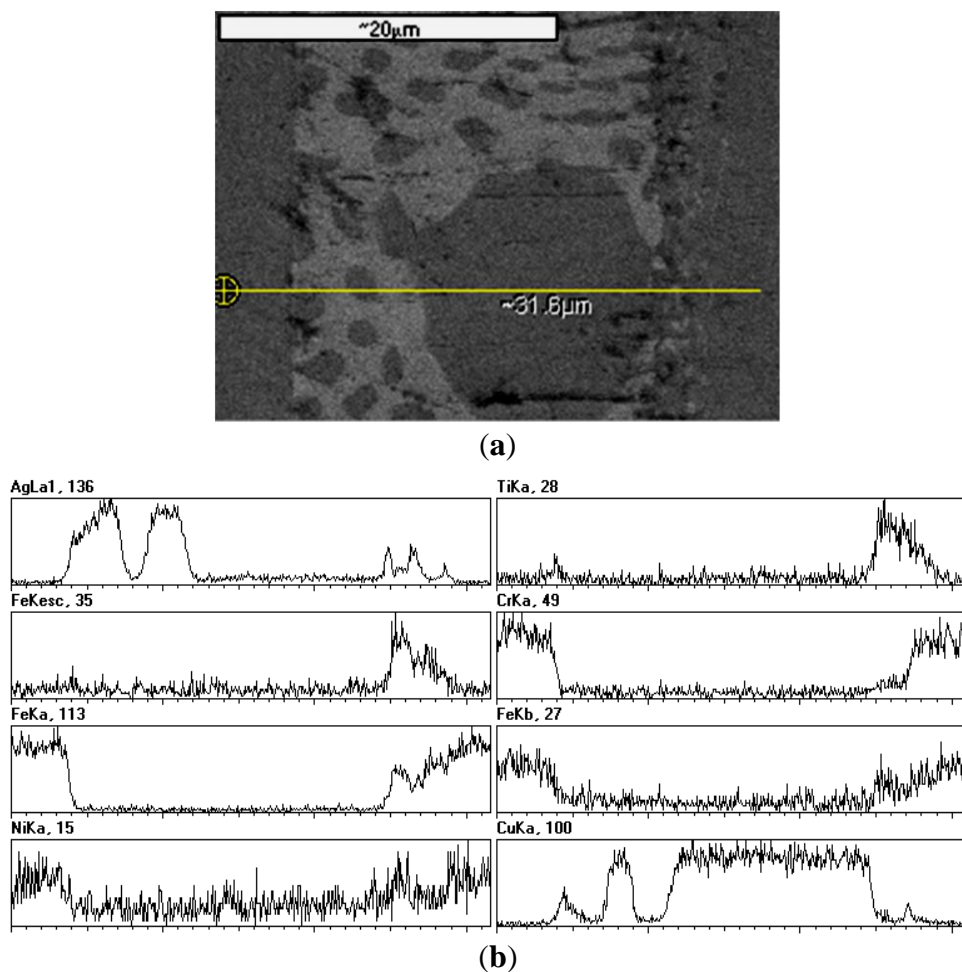
Figure 4.2   (a) SEM micrograph and corresponding (b) energy dispersive spectroscopy (EDS) line scan results from the cross section of a 316L stainless steel/Cu-Ag-Ti brazed joint.
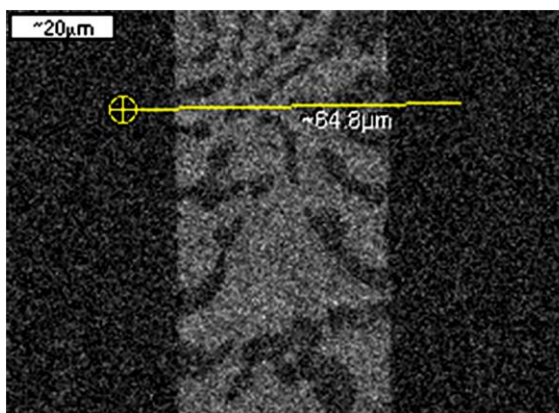
(a)
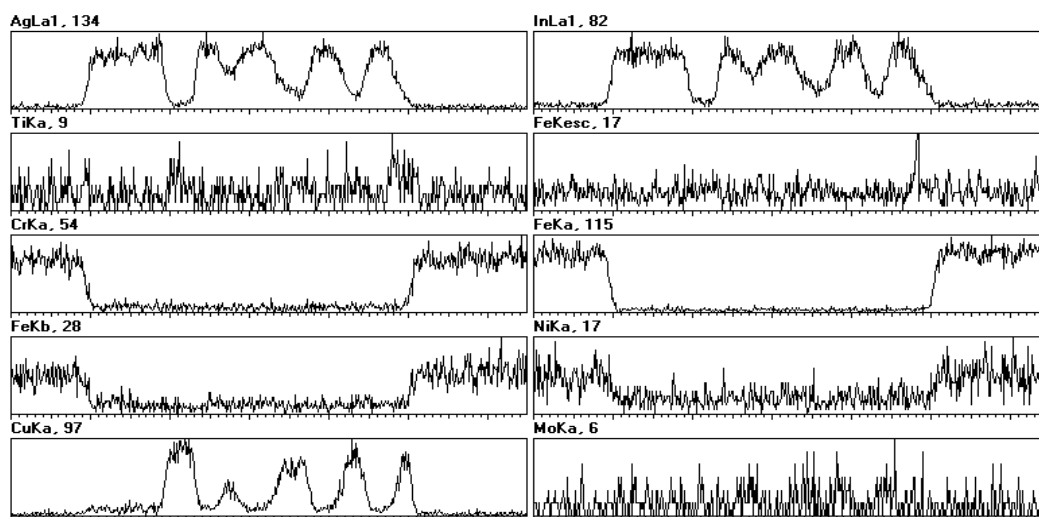
(b)

Figure 4.3 **(a) SEM micrograph and corresponding (b) EDS line scan of a cross section of a 316L stainless steel/Cu-Ag-In-Ti brazed joint.**
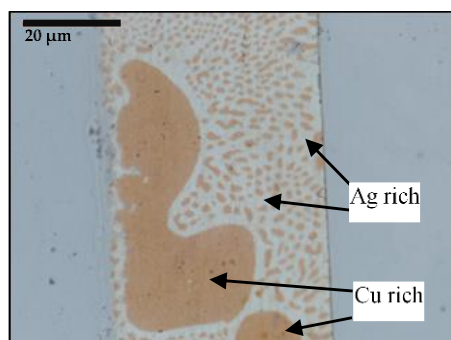
Phase	Cu	Ag	Ti
Cu Rich	94.65	5.10	0.50
Ag Rich	10.01	89.98	0.01

(**a**)
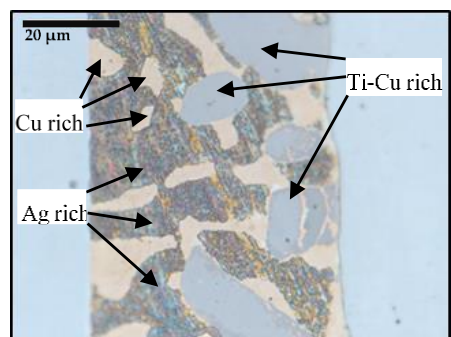
Phase	Cu	Ag	Ti	In
Cu Rich	90.18	5.86	2.09	1.88
Ag Rich	13.29	75.26	0	11.45
Cu-Ti Rich	77.27	0.84	21.21	0.67

(**b**)

Figure 4.4 **Optical image of a Cu-Ag-Ti braze (a) and Cu-Ag-In-Ti braze (b) with labeled markers indicating the microconstituent phases present. Tables to the right of each image present average atomic % for each phase in (a) and (b), respectively, calculated from EDS data.**
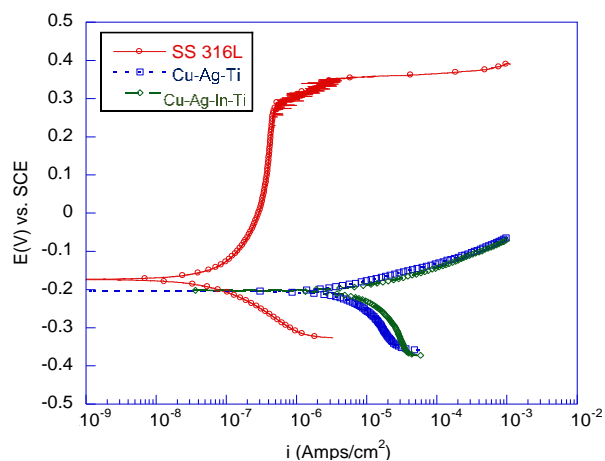
Figure 4.5 **Potentiodynamic polarization scans conducted on brazes (blue and green traces) and a 316L stainless steel sample (red trace) in 0.6 M NaCl. The scan rate for all testing was 0.166 mV/s.**
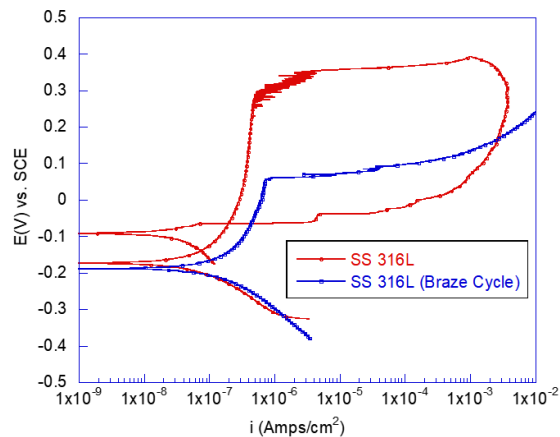
Figure 4.6   Potentiodynamic polarization scans conducted on 316L stainless steel subjected to a thermal brazing cycle (blue curve) compared to unfired 316L (red curve). Testing was conducted in 0.6 M NaCl with a scan rate 0.166 mV/s.
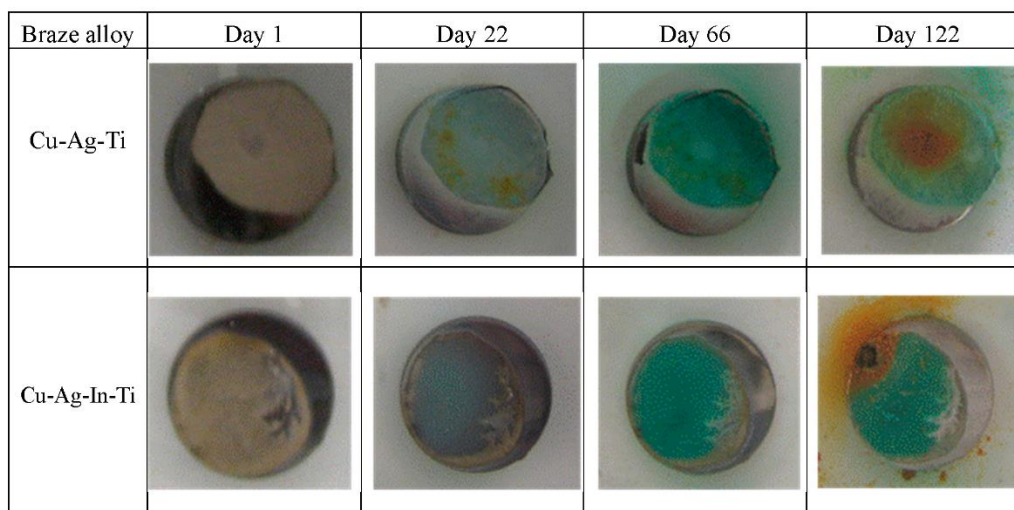
Figure 4.7   Time lapse photographs of corrosion propagation during long term exposure testing in 0.6 M NaCl. Cu-Ag-Ti (top) and Cu-Ag-In-Ti (bottom) braze alloy foil disks were used to coat ~80% of the exposed face area on 316L stainless steel samples. The stainless steel disk diameter was 16 mm for both samples.
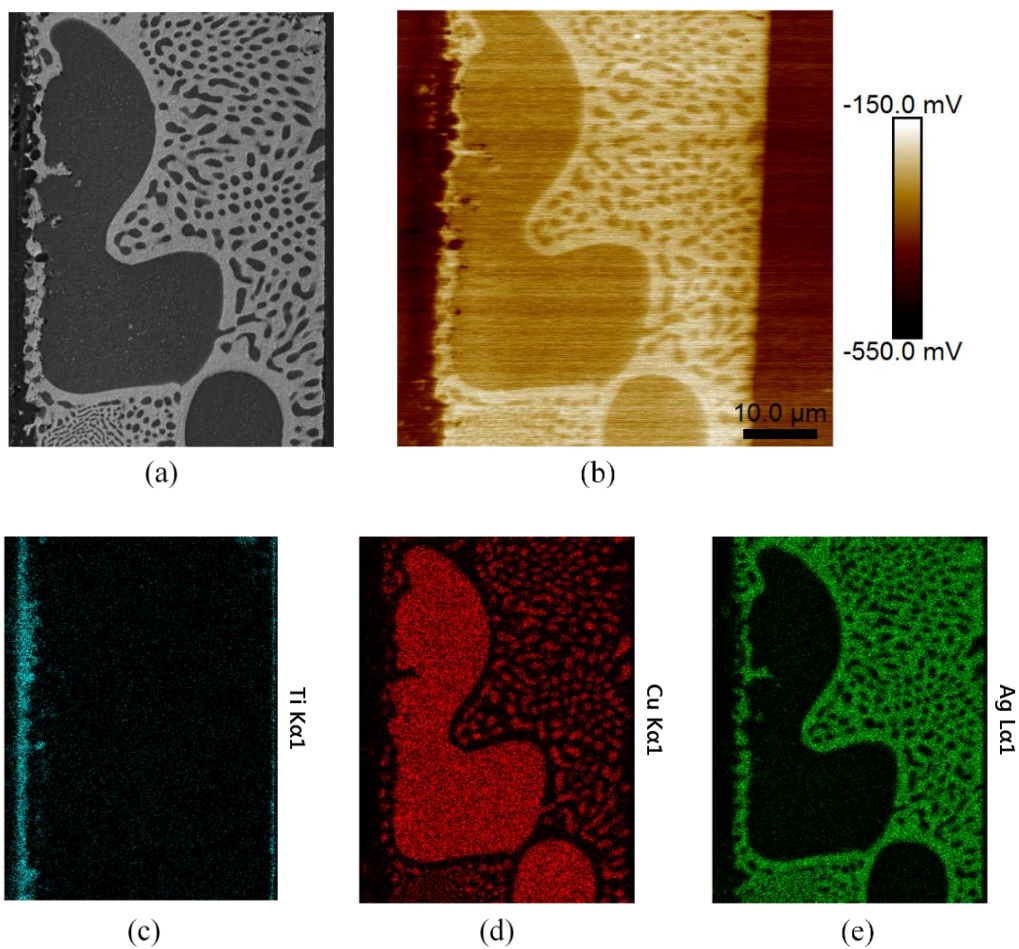
Figure 4.8 **Secondary electron SEM image of Cu-Ag-Ti sample (a) followed by corresponding Scanning Kelvin Probe Force Microscopy (SKPFM) surface potential image (b). EDS elemental maps of the identical region for: Titanium (c); Copper (d); and Silver (e) are shown.**

(a)　　　　　　　　　　　　　　(b)

(c)　　　　　　(d)　　　　　　(e)　　　　　　(f)
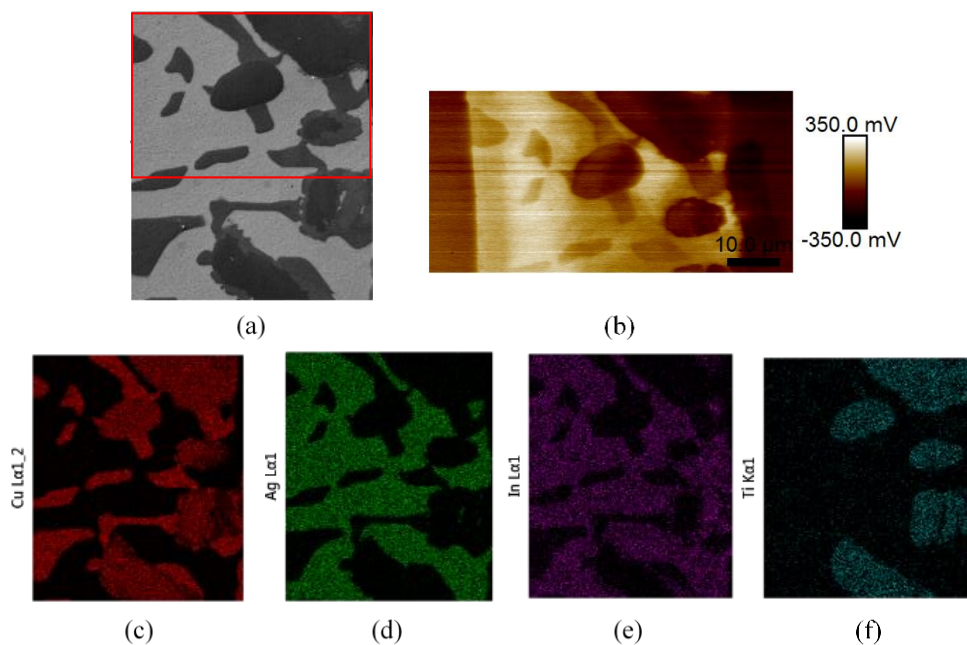
Figure 4.9　　Secondary electron SEM image of Cu-Ag-In-Ti sample with the red box indicating where SKPFM was performed (a). SKPFM surface potential image (b) and EDS elemental maps of the identical region for: Copper (c); Silver (d); Indium (e); and Titanium (f) are shown.
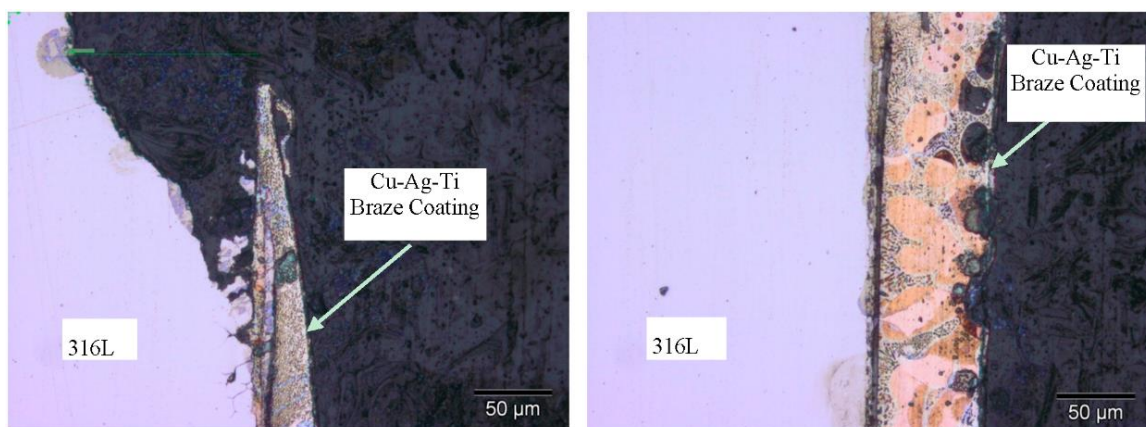
Figure 4.10　　Cross sectioned 316L stainless steel sample with a Cu-Ag-Ti braze alloy coating following exposure for seven days in 0.6 M NaCl followed by a potentiodynamic scan.

(a)   (b)

(c)
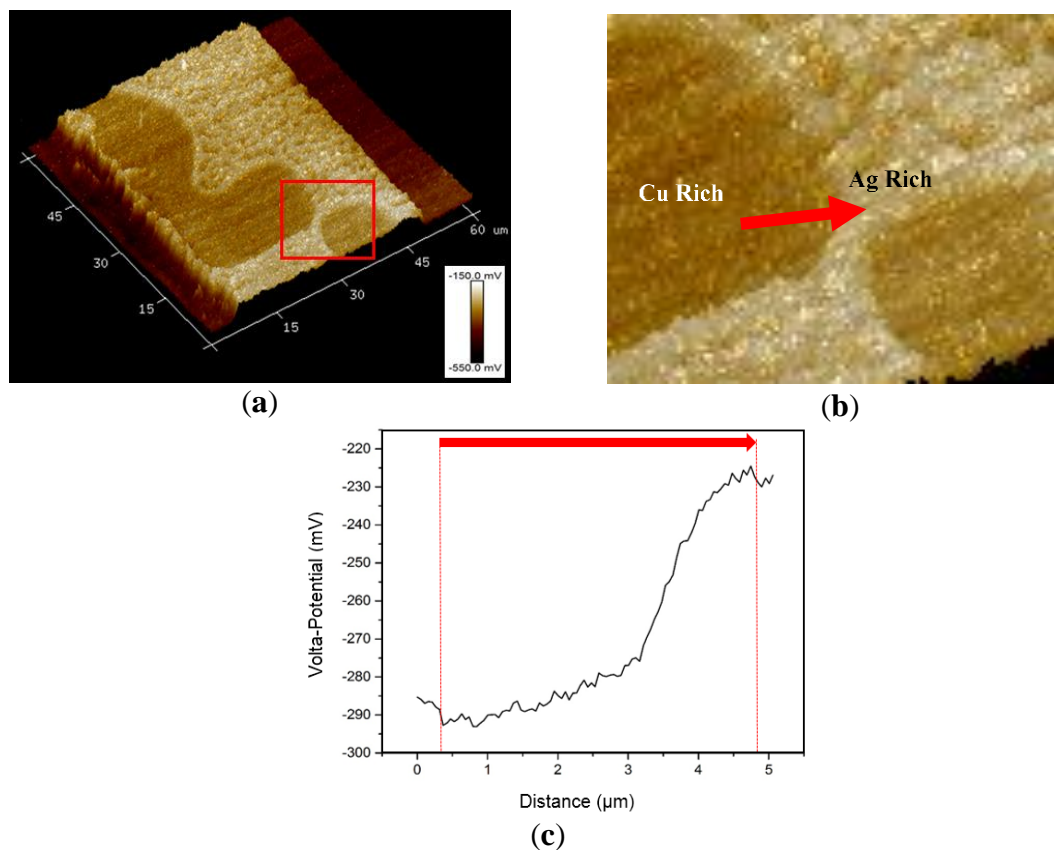
Figure 4.11   **(a) Three dimensional (3-D) SKPFM Volta potential image of Cu-Ag-Ti sample with a box indicating area of zoom seen in (b). The red arrow in (b) indicates location of data presented in graph (c) of potential values as a function of distance.**

(a)

(b)

(c)

(d)
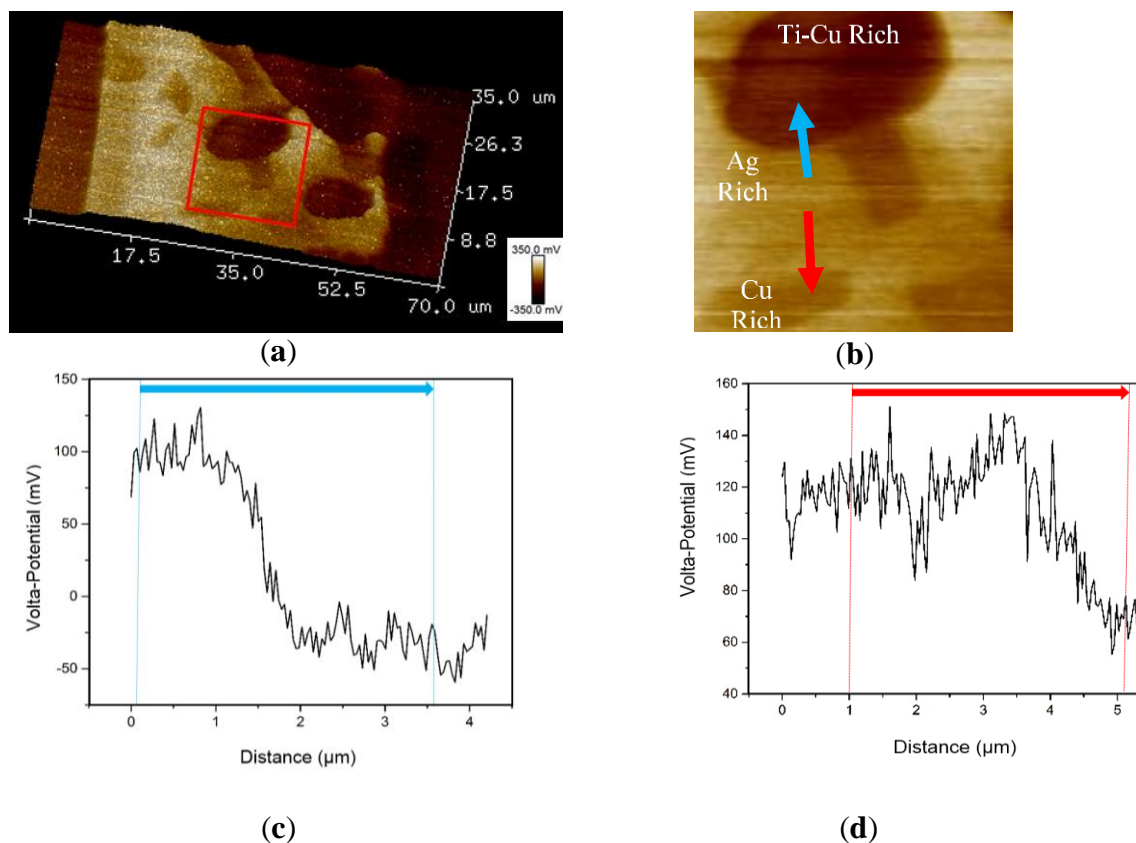
Figure 4.12 **(a) 3-D SKPFM potential image of Cu-Ag-In-Ti sample with a box indicating area of zoom seen in (b). The red and blue arrows in (b) indicate the locations of data presented in graphs (c) and (d). Potential values as a function of distance with indicating arrow: (c) Blue arrow (Ag-rich phase to Ti-Cu-rich phase); and (d) Red arrow (Ag-rich phase to Cu-rich phase).**

Tables

Table 4.1 **Compositions in atomic percent of the braze alloys**

Material	Ag	Cu	Ti	In
Cu-Ag-Ti	63.1	35.1	1.8	–
Cu-Ag-In-Ti	59.00	27.25	1.25	12.5

Table 4.2 **Compositions in atomic percent of joining material**

Material	C	P	Ni	Cr	Mn	Mo	N	Si	S	Fe
316L	0.0002	0.00036	0.101	0.1663	0.0168	0.0203	0.00066	0.00485	0.00026	Balance

Table 4.3 **Relative Volta potential difference (VPD) values in mV of phases within the Cu-Ag-Ti brazed joint. The first phase/metal is the more positive of the two.**

Microgalvanic Couple (Cathode–Anode)	ΔVPD (± 30 mV)
Ag Rich–Cu Rich	59
Cu Rich–Stainless steel	94

Table 4.4 **Relative VPD in mV of the Cu-Ag-In-Ti sample. The first phase/metal is the more positive of the two.**

Microgalvanic Couple (Cathode–Anode)	ΔVPD (± 30 mV)
Ag Rich–Cu Rich	52
Cu Rich–(Ti-Cu) Rich	97
(Ti-Cu) Rich–Stainless Steel	53

CHAPTER FIVE: CORROSION INITIATION AND PROPAGATION ON
CARBURIZED MARTENSITIC STAINLESS STEEL SURFACES STUDIED VIA
ADVANCED SCANNING PROBE MICROSCOPY.

This chapter has been accepted to be published by MDPI in a special issue entitled
Corrosion and Protection of Materials.

Reference:

Kvryan, A.; Efaw, C.M.; Higginbotham, K.A.; Maryon, O.O.; Davis, P.H.; Graugnard,
E.; Trivedi, H.K.; Hurley, M.F. Corrosion Initiation and Propagation on Carburized
Martensitic Stainless Steel Surfaces Studied via Advanced Scanning Probe Microscopy.
Materials **2019**, *12*, 940.

Corrosion initiation and propagation on carburized martensitic stainless steel surfaces studied via advanced scanning probe microscopy

Armen Kvryan[a]

Corey M. Efaw[a]

Kari A. Higginbotham[a]

Olivia O. Maryon[a]

Paul H. Davis[a]

Elton Graugnard[a]

Hitesh K. Trivedi[b]

Michael F. Hurley[a]

[a]Micron School of Materials Science & Engineering, Boise State University, Boise, ID 83725-2090

[b]UES, Inc., Dayton, OH 45432

Author Roles

All authors contributed to writing the manuscript. Conceptualization, Armen Kvryan, Corey M. Efaw, Paul H. Davis, Michael F. Hurley; Investigation, Armen Kvryan, Corey M. Efaw, Kari Higginbotham, Olivia Maryon; Project administration, Paul H. Davis, Michael F. Hurley; Visualization, Armen Kvryan, Corey M. Efaw, Kari Higginbotham, Olivia Maryon, Paul H. Davis, Michael F. Hurley; Resources, Paul H. Davis, Elton Graugnard, Hitesh K. Trivedi, Michael F. Hurley; Funding Acquisition, Hitesh K. Trivedi, Elton Graugnard , Paul H. Davis , Michael F. Hurley; Validation, Hitesh K. Trivedi ; Supervision, Michael F. Hurley.

Abstract

Historically, high carbon steels have been used in mechanical applications because their high surface hardness contributes to excellent wear performance. However, in aggressive environments, current bearing steels exhibit insufficient corrosion resistance. Martensitic stainless steels are attractive for bearing applications due to their high corrosion resistance and ability to be surface hardened via carburizing heat treatments. Here three different carburizing heat treatments were applied to UNS S42670: a high temperature temper (HTT), a low temperature temper (LTT), and carbo-nitriding (CN). Magnetic force microscopy showed differences in magnetic domains between the matrix and carbides, while scanning Kelvin probe force microscopy (SKPFM) revealed a 90-200 mV Volta potential difference between the two phases. Corrosion progression was monitored on the nanoscale via SKPFM and in situ AFM, revealing different corrosion modes among heat treatments that predicted bulk corrosion behavior in electrochemical testing. HTT outperforms LTT and CN in wear testing and thus is

recommended for non-corrosive aerospace applications, whereas CN is recommended for corrosion-prone applications as it exhibits exceptional corrosion resistance. The results reported here support the use of scanning probe microscopy for predicting bulk corrosion behavior by measuring nanoscale surface differences in properties between carbides and the surrounding matrix.

Introduction

The performance of advanced gas turbine engines is currently limited by degradation of the mechanical components, in particular rolling bearing elements such as the raceway [1]. This is because aerospace engine bearings are subject to extreme operating conditions, including elevated temperatures, high speeds, vibratory stresses, rolling contact fatigue, and complex lubricant and environment interactions [2]. Accordingly, both high hardness and high toughness are critical requirements for aerospace bearing materials, yet achieving both in a single material is challenging. M50, a through-hardened carbon steel, was developed for aircraft engine bearing applications and has become the standard bearing steel used in the United States due to its ability to perform well at high temperatures while maintaining relatively high fracture toughness compared to earlier generation carbon steels, such as AISI 52100 (UNS G52986) [1, 3, 4]. In the case of sea-based or coastal aircraft operations however, open turbine engine systems can limit the ability of ester-based lubricants to provide wear and corrosion protection, as the surrounding environment introduces water and marine aerosols into the engine during both storage and operation [5]. The presence of water in the lubricant can then serve to initiate aqueous corrosion during engine cycling and downtime [5]. Consequently, current aero-engine performance is limited by corrosion-enhanced wear of

the metallic bearings and drive components, which leads to increased maintenance and premature failure [1, 6-8]. Thus, there has been significant research effort to develop alternative bearing steels to M50 that exhibit enhanced corrosion resistance to support increased engine performance [3, 4, 7-10].

Martensitic stainless steels (MSSs) were developed for use in applications where high wear resistance and toughness is required whilst maintaining high corrosion resistance. These properties, combined with their potential for high hardness upon heat treatment [1, 11-15], have led to MSSs being implemented in many demanding applications, including bearings, molds, nuclear reactors, hydroelectric engines, and petrochemical steam and gas turbines and buckets [1, 11-20]. To improve surface wear resistance while maintaining the corrosion resistance of the core, MSSs can instead be surface treated (carburized), with carbon incorporated into the sample surface at elevated temperatures to form hard carbides with alloying elements such as chromium or vanadium [1, 21-23].

Highly corrosion resistant MSSs (e.g., Cronidur 30 or XD15NW) include additions of alloying elements (and/or nitrogen) and can have poor adhesive and wear performance [24]. While not as corrosion resistant, UNS S42670 or AMS 59030B (referred to herein as P675) is a relatively cost-efficient MSS with high corrosion resistance (equivalent to 440C steel) and bulk fracture toughness (higher than M50) [25]. P675 was specifically engineered for aerospace bearing applications in advanced gas-turbine engines, where conventional bearing steels (e.g., M50 and 440C) are adversely affected by corrosion in aggressive environments and/or do not have sufficient high temperature wear performance [8]. Although P675 shows improvement in corrosion

resistance relative to conventional bearing steels, higher surface hardness would lead to a longer wear lifetime in-service. Accordingly, secondary surface processing has been targeted as a way to increase the hardness and wear resistance of P675 [7, 9, 10, 26]. Such surface treatments impart a graded microstructure that extends ~1000 µm below the metal surface. Optimized wear properties are obtained by balancing the surface hardness and core ductility of composite microstructures across the gradient region. However, the increased surface hardness typically comes at the expense of corrosion resistance, as the formation of carbides on the surface locally depletes corrosion-resistant elements (e.g., chromium, vanadium, molybdenum) from the surrounding matrix [7, 20, 22, 23, 27, 28].

The corrosion performance of various P675 surface treatments has been previously assessed through accelerated DC and AC electrochemical testing in aqueous solutions [7, 9, 10]. These investigations provided a ranking of corrosion performance, showing that the final tempering temperature and processing atmosphere had a considerable influence on both the overall corrosion rate and damage morphology. Compared to M50, surface hardened P675 can be significantly more corrosion resistant, and higher processing temperatures typically increased susceptibility to general corrosion damage, while lower temperatures exhibited more localized corrosion relative to untreated P675 [7]. The influence of processing on P675 wear performance for the same steels in non-corrosive wear testing has also been reported, where higher processing temperatures (HTT) yielded longer bearing lifetimes compared to LTT [29, 30]. However, there remains a need for research into the interdependency between simultaneously balancing corrosion resistance and surface hardness for bearing

applications, since wear resistance (i.e., bearing performance) in corrosive environments is ultimately limited by corrosion [11].

Investigation of surface electronic properties can provide information to aid in the prediction of corrosion initiation sites [31]. Recently, scanning Kelvin probe force microscopy (SKPFM) has been used to investigate the role of nano- and micro-scale surface features on corrosion behavior [19, 32-42]. Additionally, magnetic force microscopy (MFM) [43-45] has been used to similarly provide insight into the magnetic behavior of alloy surfaces. SKPFM permits measurement with nanoscale resolution of Volta potential differences (VPDs), which are related to the electronic work function (EWF), while MFM provides information regarding the magnitude and orientation of the magnetic moments of surface domains. Likewise, in situ atomic force microscopy (AFM) has been used to monitor morphological changes during corrosion in electrolyte solution and link them to the electrochemical behavior of the material [19, 46-49]. The current work presents the first application of such techniques to investigate corrosion behavior of MSS P675 with various surface treatments. Since corrosion is the most common precursor to wear damage during aero-engine operation [8], the time to onset and rate of corrosion can directly control maintenance requirements and operational costs. Initiation and propagation are critical considerations because they determine both wear behavior as well as the lifetime of the part or engine [8, 50, 51]. The focus of this study is to understand the effects of heat treatment processing parameters on corrosion evolution in P675 by utilizing a combination of scanning probe microscopy (SPM) techniques and accelerated corrosion testing, thereby linking surface microstructural differences (on the nanoscale) with observed macroscale surface corrosion behavior and wear performance.

Materials and Methods

Materials

The nominal bulk composition of P675 (UNS S42670, the MSS studied here)

prior to heat treatment is shown in Table 5.1 [29]. To increase surface hardness, P675

samples were carburized, followed by quenching and tempering, to harden the outer layer

or case. Samples were cylindrical (9.5 mm diameter x 12 mm height) with post-treatment

case depths of 750-1250 µm radially inward [9]. Samples differed in the final tempering

temperature and carburization atmosphere: high temperature tempering (HTT) at 496°C,

low temperature tempering (LTT) at 315°C, and carbo-nitrided (CN) where the case was

obtained through a carburizing cycle followed by nitriding cycle during heat treating.

Further details on the processing routes are discussed in previous works [9, 10, 29, 30].

Prior to SPM characterization, samples were mechanically ground with SiC paper (to

2000 grit) in deionized (DI) water, followed by sequential polishing to 0.02 µm with a

colloidal silica aqueous slurry. After polishing, samples were rinsed with ethanol and

sonicated for 1 minute in ethanol to remove any polishing residue.

Electron Microscopy

A field emission scanning electron microscope (SEM, FEI Teneo, Hillsboro,

USA) coupled to an energy-dispersive X-ray spectrometer (EDS, 80 mm^2 Energy+,

Oxford Instruments, Abingdon, UK) was utilized to characterize the surface

microstructure and corrosion morphology of all samples, as well as construct elemental

composition maps of the heat-treated surfaces. SEM analyses were conducted in both

secondary electron (SE) and backscattered electron (BSE) imaging modes using 10–20

keV accelerating voltages.

Scanning Probe Microscopy

Ex situ SPM

Ex situ AFM, MFM, and SKPFM were performed under an inert argon

atmosphere containing <0.1 ppm H_2O and O_2 using a Bruker Dimension Icon AFM

housed in an MBraun glovebox (MBraun, Stratham, USA). Prior to imaging, previously

polished and sonicated samples were cleaned with HPLC/spectrophotometric grade

ethanol (Sigma-Aldrich, 200 proof, St. Louis, USA) using lint-free wipes (Kimtech).

Following ethanol cleaning, compressed ultra-high purity nitrogen gas (Norco UHP,

99.999%) was used to dry the surface of the steel and remove any remaining surface

particulates before introducing the samples into the glovebox antechamber.

Both MFM and SKPFM were performed using a dual-pass lift mode

implementation in which the first pass over each scan line acquires surface topography.

Upon completing the first pass, the probe then lifts off the surface to a user-defined

height above the surface. This height (i.e., tip-sample separation, 100 nm in this study)

remains constant throughout the second pass as the electromagnetic property of interest

(i.e., Volta potential difference in the case of SKPFM or magnetic moment in the case of

MFM) is measured. Surface topography was mapped using either intermittent contact

(tapping) mode in the case of MFM imaging or PeakForce tapping mode (Bruker Nano,

Santa Barbara, USA), which employs rapid force curve acquisition with a user-defined

force setpoint (typically 2 nN here), in the case of AFM and SKPFM. In MFM, the

magnetic force gradient between a magnetized Co-Cr coated AFM probe (Bruker MESP,

$k = 2.8$ N/m, $f_0 = 75$ kHz, $\mu = 1 \times 10^{-13}$ EMU, where 1 EMU = 1 erg G^{-1}) and the surface

of the material was observed during the lift mode pass. For consistency, all MFM

imaging reported herein was performed with the same MESP probe, which was magnetized immediately prior to imaging with its magnetic axis perpendicular to the sample surface. In SKPFM, the Volta potential difference (VPD) between a conductive probe (Bruker PFQNE-AL, $k = 0.8$ N/m, $f_0 = 300$ kHz) and the surface was quantified by application of a DC bias to null the tip-sample electric force gradient arising from the difference in Volta potential between the probe and sample surface. VPD maps were acquired utilizing frequency modulation SKPFM [31], as described in detail elsewhere [37,38]. These VPD maps were used to predict the corrosion behavior of the samples by suggesting the cathodic and anodic sites and the relative driving force for galvanic corrosion.

SKPFM was also used to observe corrosion initiation and propagation mechanisms by carrying out intermittent imaging at well-defined intervals throughout the corrosion process. While all such imaging was carried out within the controlled environment (<0.1 ppm H_2O and O_2) of the argon-filled glovebox, corrosion was initiated and allowed to proceed outside the glovebox, where samples were sequentially soaked for prescribed amounts of time in a 1 M NaCl solution prepared from reagent grade NaCl (Sigma Aldrich, St. Louis, USA) and deionized (DI) water. After each time increment, samples were rinsed with DI water to remove any adhered salt, dried with UHP nitrogen, and cleaned with ultrapure ethanol using lint-free wipes. The samples were then reintroduced into the glovebox and imaged via dual-pass SKPFM. Repeated nanoscale imaging at specific recurrent locations with micron-scale positional accuracy was made possible by fiduciary marks created with a diamond tip indenter. Testing and imaging

were performed ~500 µm away from the fiduciary mark to ensure results obtained were

not influenced by the indent

In situ SPM

To capture images of corrosion initiation and propagation in real time, in situ

PeakForce tapping (topographical) AFM was also performed. In contrast to the ex situ

(i.e., glovebox) SPM imaging, samples for in situ AFM imaging were mounted in a fluid

cell and immersed in a 0.1 M NaCl solution under ambient atmosphere. The NaCl

concentration was chosen such that it would initiate corrosion on samples at an

appropriate timescale to reveal changes in topography concurrent with corrosion

propagation and progression. Silicon nitride probes with a nominal tip radius of 20 nm

(Bruker ScanAsyst-Fluid, $k = 0.7$ N/m, $f0 = 150$ kHz) were used for repetitive imaging

(0.5 Hz scan rate) of 10 x 10 µm2 areas at 512 x 512 pixel resolution, corresponding to a

refresh rate of ~8.5 minutes to capture each image. Due to differences in time between

initial immersion of each sample and the initial image capturing (driven by optimization

of imaging parameters), the specific timing of subsequent images are not exact between

samples. The total amount of time each sample had been exposed to the corrosive salt

solution was documented at both the start and end of captured images.

Image Processing

SPM image processing and quantitative analysis were conducted using

NanoScope Analysis 1.90 (Bruker). All topographical images were processed with a first

order flatten filter to remove sample tip and tilt as well as any individual line-to-line

offsets. The images for HTT at 116 and 135 min required a 2nd order flatten procedure to

account for the deposited debris. To quantify the findings from SKPFM mapping, a

threshold technique was implemented (see example image in Figure 1 below) that utilized a user-determined cut-off potential based on the distribution of Volta potentials observed in the corresponding data histogram (512 bins). From the resulting thresholded data, the average Volta potential (with corresponding standard deviation) was calculated for each of the two phases present on the surface (i.e., matrix and carbides, identities confirmed through SEM/EDS characterization) [52]. Figure 1a shows a representative SKPFM Volta potential map for HTT P675. Figure 1b shows the matrix in dark brown with the carbides (data in blue) excluded, while the light brown areas visible in Figure 1c correspond to the carbides (with the matrix excluded and indicated by the dark blue areas). Using this method, an average VPD between the matrix and carbides was calculated for each SKPFM image.

Electrochemical Corrosion Testing

Electrochemical cyclic polarization testing was used to characterize corrosion behavior for each type of heat-treated steel. Sample preparation details can be found in a previous publication, thus the sample testing area was defined by masking off the sample such that only a circular area (diameter ~6.6 mm) test area was in contact with the electrolyte solution [7]. Testing was conducted in 0.01 M NaCl electrolyte solution with a potentiostat (SP-300, Bio-Logic, Seyssinet-Pariset, France) used to control and monitor a three-electrode system in a modified flat cell. A saturated calomel electrode (SCE) served as the reference electrode and a platinum mesh as the counter electrode. Following sample immersion, open circuit potential (OCP) was monitored for 30 min. The sample was then polarized at a scan rate of 0.5 mV/s from 100 mV below OCP to 600 mV above OCP or when pitting had stabilized, followed by a reverse scan back to OCP.

Results

<u>Surface Composition</u>

The carburizing and carbo-nitriding heat treatment processes performed on MSS

P675 resulted in the development of well distributed metal-carbon precipitates (carbides)

ranging in size from approximately 10 nm to 2 µm in diameter (Figure 2a), surrounded

by the martensitic matrix at the sample surface. In addition to the surface, the carbides are

present diminishingly, approximately 1000 µm radially inward into each of the samples

(data not shown). Sample surfaces were analyzed via EDS (Figure 2b) to resolve carbide

chemistry and determine alloying elements that segregated from the matrix to form these

carbides during heat treatment. Carbides resulting from all three surface treatments were

found to be predominantly carbon- and chromium-rich with lesser amounts of vanadium,

molybdenum and/or manganese, while the surrounding matrix showed primarily iron,

cobalt, and nickel. In previous work done on P675, X-ray diffraction (XRD) and electron

beam backscattered diffraction (EBSD) determined M_7C_3 (orthorhombic) and $M_{23}C_6$

(face-centered cubic) to be the primary carbides formed in P675 (M represents the metal

in the carbide), with $M_{23}C_6$ precipitating after M_7C_3, and chromium being the primary

metal constituent present in the carbides [27, 53]. HTT contains a greater population of

M23C6 carbides than LTT and CN due to its higher tempering temperature (i.e. increased

kinetics). By stoichiometry, the HTT carbides contain more chromium than the carbides

of the other two surface treated steels despite all having the same bulk composition

before heat treating. The large amount of chromium present in the bulk (pre-heat

treatment) P675 alloy (Table 5.1), coupled with the presence of molybdenum, should

yield a magnetic MSS [54-56]. However, EDS analysis (Figure 5.2a,b), performed on the

bulk surface of each steel, showed that the chromium and molybdenum primarily

segregated within the carbides following heat treatment (thereby increasing the likelihood

of magnetic carbides). EDS was performed on the bulk steel and not on the individual

carbides due to inconsistent results obtained since large interaction volumes (by the EDS)

penetrated both the carbide and surrounding matrix. In contrast, nickel, in the presence of

iron and carbon acts as an austenite stabilizer and thus promotes a non-magnetic

austenitic (fcc) structure [57]. MFM was therefore utilized to observe how the secondary

processing performed on these steels affected the magnetic properties of the surface.

Scanning Probe Microscopy

MFM

MFM was utilized to map variations in the magnetic moment projections (surface

normal direction) on the surface of the steels (Figure 5.3). In Figure 5.3, purple regions

are identified as carbides since these coincide with regions that are raised in topography

and visually similar to carbides seen in SEM/EDS analysis (see Figure 5.2).

Topographical relief of the carbides was expected due to differential polishing rates

during sample prep, resulting in the harder carbides slightly protruding above the

surrounding matrix. MFM results indicated that the carbides and the matrix both exhibit

out-of-plane magnetic domains (i.e., positive magnetic direction, non-parallel to surface),

but with varying magnitudes; carbides being noticeably larger than the matrix as expected

from the enhanced chromium concentration (see Figure 5.2). Within the matrix,

nanoscale variations in magnetic domain were also evident. In HTT these were larger and

more elongated those on either LTT or CN. CN had the finest distribution of different

magnetic domain regions able to be resolved within the matrix.

<u>Inert Environment SKPFM</u>

Freshly polished, cleaned, and dried samples underwent ex situ SPM imaging in an inert atmosphere glovebox. Images were acquired using sequentially larger scan areas of 10 x 10 μm^2, 20 x 20 μm^2, and 90 x 90 μm^2, with contrast between carbides and the surrounding matrix observed in both Volta potential and topography (Figure 5.4). Numerical VPD results were calculated per the method described earlier and compiled for comparison (see Figure 5.5; error bars are indicative of one standard deviation). The measured VPD of the carbides ranged from 60 to 200 mV greater than the steel matrix, depending on the scan size analyzed, with HTT possessing the highest difference and CN the lowest. The relative magnitudes of the carbide-matrix VPDs remained consistent regardless of scan size, suggesting even the smallest imaging areas chosen (10 x 10 μm^2) were large enough to be representative of the sample while also providing the highest spatial resolution of VPD variations.

<u>Intermittent SKPFM</u>

Intermittent ex situ SKPFM was performed to track the evolution of the surfaces resulting from sequential sustained exposure to corrosive conditions. Samples were placed in a corrosive salt solution and the VPD maps were obtained at intervals of 0, 1, 2, 10, and 15 cumulative minutes of exposure to 1 M NaCl solution (Figure 5.6). Qualitative differences in both appearance (surface topography and morphology) and carbide-matrix VPD over time were observed for the steels. The HTT sample showed the formation of particulates on the surface and degraded uniformly with time, leading to a progressively lower variation in surface VPD. In contrast, the CN sample showed little change in VPD or topography on the surface, indicating corrosion reaction kinetics were much slower

despite the distinct VPD contrast between the carbides and matrix. LTT exhibited behavior somewhere in between the other two steels. Initially salt deposits on the LTT surface obscured the steel topography and VPD variations. However, with increasing time LTT appeared similar to CN, as evidenced by the relatively large contrast in topography and VPD apparent by the 15 min mark (see Figure 5.6).

Figure 5.7 presents VPD maps (left column) and plots of Volta potential versus location (middle and right columns) for cross sections of different carbide/matrix interfaces as a function of exposure time. As can be seen in the top row of Figure 5.7, the VPD between the HTT carbides and the surrounding matrix decreased with exposure time, while the VPDs of the LTT (Figure 5.7(b1,b2)) and CN (Figure 5.7(c1,c2)) carbides remained relatively constant throughout testing. For HTT, corrosion proceeded simultaneously both along grain and carbide boundaries as well as within the matrix. Corrosion products evolved and settled on both the matrix and surface carbides, where cathodic activity was supporting anodic dissolution of the matrix. With this production and deposition of corrosion products, the VPD between carbides with a native oxide and matrix decreased on the HTT surface until there was very little difference observed between the two, as seen in Figure 5.7(a1,a2). Conversely, the LTT and CN samples underwent typical localized corrosion (see Figure 5.6), wherein highly localized attack adjacent to grain boundaries/carbides was seen, as evidenced by particulates settling on or near the carbide-matrix interface. As time in solution progressed, the VPD between the carbides and steel matrix remained essentially unchanged throughout the duration of testing, with matrix attack relatively shallow. Therefore, there are notable differences in the initiation of corrosion mechanisms between different heat treated samples.

<u>In Situ AFM</u>

To observe the progression of corrosion in real time while samples were immersed in 0.1 M NaCl solution, in situ AFM was employed to monitor topographical changes over time. Figure 5.8 shows the results for the three heat-treated P675 steels with no applied bias voltage. (Variations in exposure time across samples are due to differences in corrosion rate and the time necessary to implement optimized imaging parameters.) For HTT, corrosion activity rapidly progressed and large surface deposits (~1-2 µm wide) appeared on the surface after ~107 minutes (Figure 5.8). EDS analysis indicated these large features to be iron-rich corrosion products with NaCl (analysis not shown). Despite the deposited particles, distinct localized corrosion was not seen on the HTT sample. As testing progressed, corrosion reactions proceeded, depositing corrosion product particulates on the surface (see Figure 5.8–HTT 116 & 134 min). In comparison, highly localized corrosion was evident at the carbide-matrix interfaces in both the CN and LTT samples. CN showed the greatest segregation of corrosion between matrix attack and the unaffected carbides, as indicated by near complete but shallow etching attack along carbide boundaries (Figure 5.8). LTT appeared to behave somewhere in the middle of these two extremes, with particle build-up similar to HTT seen initially, but eventually these particles cleared to reveal evidence of localized corrosion propagation in the matrix adjacent to some of the carbides, similar to CN.

Time-dependent line profile analysis of selected carbide particles was conducted on each of the samples (Figure 5.9), confirming the qualitative observations arising from the images presented in Figure 5.8. HTT showed an increase in surface contrast of the carbides, up to 50 nm, with corresponding slight, uniform changes in the height of the

surrounding matrix. For LTT, height changes across the carbide/matrix interface initially (44 min) showed ~100 nm deep attack immediately adjacent to the carbides (Figure 5.9). Then at longer times (112 min), the height of the carbides increased, accompanied by shallower apparent depth of attack in the adjacent matrix area. These changes are likely associated with the production and deposition of insoluble corrosion products. CN exhibited the sharpest contrast in topography by the end of exposure to salt solution, with the carbide surface height increasing by ~25 nm relative to the adjacent bulk matrix, with matrix attack limited to ~75 nm deep and only extending approximately 0.5 µm away from the carbide interface. The depth of attack also decreased from 103 min to 112 min, indicating slight corrosion product deposition within the highly localized area of matrix attack.

Post-testing SEM imaging was conducted on the same sample surfaces (Figure 5.10) to record surface morphological differences following the in situ AFM testing. HTT exhibited a distinctively different surface morphology compared to LTT and CN, characterized by the presence of large, fluffy appearing salt-laden corrosion deposits. Beneath these deposits and surrounding the carbides, the entire matrix surface area was uniformly corroded with no indication of matrix passivity. In contrast, both the LTT and CN carbide boundaries were attacked, with NaCl particles present along the grain boundaries and carbide-matrix separation and subsequent grain separation (Figure 5.10). LTT showed some attack along carbide boundaries as well as some generalized attack as indicated by roughening of the entire surface due to corrosion product deposition. CN displayed much more localized attack at the carbide boundaries than LTT (dotted oval in right panel of Figure 5.10), and narrow "valleys" on the order of ~0.5 µm wide were

observed around the CN carbides, confirming observations in Figure 5.8. Furthermore, unlike LTT or HTT, CN did not show evidence of adhered or deposited corrosion products. Tracing the representative "line of attack" for the CN sample in Figure 5.10 reveals a grain undergoing intergranular attack, indicative of microgalvanic corrosion between the noble carbides and the active matrix.

<u>Electrochemical Corrosion Testing</u>

To elucidate the corrosion pitting and repassivation behavior of the samples, cyclic potentiodynamic polarization (CPP) scans were conducted on each of the samples to explore the effects of the differing heat treatments. Figure 5.11 shows the resultant polarization curves, along with macro images of the sample surfaces post-electrochemical testing. Testing indicated that HTT had the lowest OCP (-400 mV), followed by LTT (-200 mV) and CN (-80 mV), respectively. This ranking is in agreement with previous studies that ranked corrosion resistance for these same steels (i.e. corrosion rate determined via electrochemical methods) [7, 9]. The LTT and CN samples exhibited a rapid change in potential over a minimal increase in current density (Figure 5.11a, green boxed areas), indicative of typical passive behavior. The breakdown potential of the LTT and CN samples occurred at 40 mV and 95 mV, respectively. Conversely, the HTT sample showed active corrosion behavior as demonstrated by linear growth of the current density over the potential sweep. However, pits were initially observed on the HTT surface (-200 mV), but did not grow and as the anodic overpotential continued to increase. The post-corrosion images in Figure 5.11b show the difference in corrosion morphology for each sample following CPP testing. For HTT, the entire test area darkened due to corrosion product formation (Figure 5.11b), engulfing the initial isolated

areas of pitting. Arrows in Figure 5.11b indicate the four pits that first formed on the HTT sample before the entire test area underwent generalized corrosion. As expected from previous work [7], LTT and CN showed a distinctly different morphology of corrosion attack, with corrosion limited to only several dispersed pits on the surface of the sample. Compared to HTT, LTT showed limited regions of depassivation emanating from corrosion pits, evidenced by regions of minor surface darkening. In contrast, corrosion attack on CN displayed only highly localized, isolated pits (Figure 5.11b) with no visual evidence of any other associated areas of depassivation.

<div align="center">**Discussion**</div>

Nanoscale Origins of Corrosion Initiation

Determining the nanoscale contributions to a material's bulk corrosion rate is inherently difficult due to the complexity and multitude of variables that influence its behavior in a corrosive environment Corrosion is a spontaneous process driven by thermodynamics [58,59]. In a microgalvanic couple, the difference in electrode potential of the anode and cathode regions on the surface correlates with the magnitude of negative free energy change (thermodynamic propensity) for local corrosion to occur. SKPFM Volta potential (VPD) mapping is the highest spatial resolution method available to directly measure the relative thermodynamic propensity for corrosion between nanoscale heterogeneities in a material. For the MSSs considered in this study, the relatively high Cr composition of the carbides suggests they are likely noble in comparison to the matrix based on the galvanic series [60]. Hence, a larger VPD between carbides and the matrix will lead to a greater drive (i.e., increased microgalvanic full-cell potential) for corrosion of the matrix. Among the steels studied, HTT consistently exhibited the largest VPD

between the carbides and the matrix (200 mV), while LTT (150 mV) and CN (90 mV) were considerably less (Figure 5.5). The relative magnitudes of these VPDs can likely be attributed to carbide chemistry, as HTT carbide composition is predominantly $M(Cr)23C6$ compared to predominantly $M(Cr)_7C_3$ compounds for LTT and CN. An interesting finding of this study is that for each of the surface treatments considered, the bulk OCP values measured inversely corresponded with the magnitude of the VPD between the carbide and matrix phases (Figure 5.5); HTT had the greatest carbide/matrix VPD and least noble OCP (-400 mV), CN had the lowest VPD and most noble OCP (-80 mV), and LTT was intermediate with a carbide/matrix OCP of -200mV. This observation demonstrates how local SKPFM measurements of the relative microgalvanic couple potential contribute to the bulk OCP observed on each of the different surface-treated MSSs investigated. In addition, variations in chromium enrichment of the carbides subsequently influenced both the VPD and degree of passivity of the surrounding chromium-depleted matrix. The steepest VPD gradients measured were across the carbide/matrix interface (Figure 5.7), and so SKPFM measurements also provided a technique to predict and locate expected points of microgalvanic corrosion initiation on the surface.

<u>Corrosion Propagation</u>

SKPFM measures VPDs on the surface, which are influenced by the presence of oxide layers. With MSSs, passivating chromium oxide layers are readily formed and act as a kinetic barrier to corrosion, which complicates any correlation of thermodynamic propensity derived from SKPFM measurements. However, for the steels considered herein, since the bulk composition is the same, data obtained from SKPFM also provided

information on the spatial variations in surface properties that influence corrosion

propagation. Intermittent SKPFM testing was conducted to monitor shifts in

microgalvanic couples' VPD over time due to corrosion activity. For HTT, the VPD

between the carbides and the matrix decreased with time (Figure 5.7). As a result, as the

duration of corrosion propagation increased, the VPD between carbides and the matrix

approached 0 mV for HTT, resulting in a more thermodynamically homogenous surface.

In contrast, for LTT and CN the initial VPD between the carbides and matrix phase was

smaller, but remained nearly constant throughout testing, with only minor evidence of the

corrosion activity apparent on the surface (Figures 5.6 and 5.7). This behavioral

difference can be attributed to differences in the passive oxide layer performance, and is

also reflected in the VPD measurements, which are highly influenced by the presence of

surface oxides. Previous work by Schmutz and Frankel showed similar behavior on

aluminum alloys and indicates that the shift in VPD observed on HTT following active

corrosion was caused by oxide growth at cathodic sites and the generation and deposition

of corrosion products at active sites creating a more homogenous surface [51]. For

carburized MSSs, the magnitude of VPD surface variation measured by SKPFM pre-

corrosion provided an indication of the how the VPD evolved as a result of exposure to

corrosion conditions: smaller initial VPD between the carbides and matrix phase

indicated more robust passivity during corrosion, as seen in CN and LTT steels. For

HTT, the higher initial VPD between the carbides and matrix indicated a greater

susceptibility to depassivation and more uniform corrosion activity during propagation.

These findings were validated with bulk electrochemical testing (Figure 5.11), where

CPP testing showed that LTT and CN had a more protective oxide layer as indicated by

the presence of a passive region in the CPP scan. Moreover, during intermittent SKPFM testing the VPD on HTT evolved rapidly and HTT exhibited active corrosion behavior throughout CPP testing.

While the bulk amount of chromium present at the surface is the same for all steels considered, the spatial distribution is different among the three surface treatments, leading to distinctly different corrosion properties and behavior. Relative to LTT and CN, HTT tended to corrode more uniformly and had a higher VPD between carbides and matrix. HTT was more prone to depassivation compared to LTT despite both having identical bulk chemical composition and same carburization cycle (carburized in single furnace load). The different carbide-matrix VPDs among the samples influences or indicates how local solution chemistry likely evolves during active corrosion on MSSs. This suggests that for HTT, as pitting progressed, the local solution chemistry, most likely due to higher sensitization during tempering cycle, was sufficiently aggressive to cause widespread depassivation. Conversely, with LTT and CN samples, the VPD between carbides was smaller and pitting was unable to transition to more widespread corrosion, suggesting local solution chemistry evolution did not support auto-catalytic depassivation as corrosion propagated. Here the lower VPD observed for LTT and CN indicated the matrix phases exhibited more robust passivity than the matrix of HTT. The in situ SKPFM VPD measurements correlate with the observed corrosion morphology of the steels. That is, the measured carbide-matrix VPD for each steel is inversely proportional to the extent of general (uniform) corrosion resistance of the steel. The efforts in this paper show that SKPFM is able to effectively predict bulk corrosion

behavior of different surface treatments by observing and measuring nanoscale surface

VPD differences between carbides and the underlying matrix.

SPM Characterization and Implications on Wear

MFM provides a method to characterize local variations in magnetic properties

that contribute to the bulk magnetic properties. For all steels studied, the carbides showed

variable shades of purple/blue in the MFM maps (~1-3° phase shift), indicating slightly

different magnetic properties within the individual phases (Figure 5.3), likely due to

different carbide compositions in terms of the relative amounts of chromium and

molybdenum, which influence the magnetic properties of phases [61-64]. Sample CN had

a much less homogenous matrix that showed considerable variation in magnetic

properties and is likely an effect of the relatively highly surface retained austenite (18-

22%) found within the matrix phases compared to LTT (10-13%) and HTT (1-2%) [9,

30]. The bulk magnetism of the steels will change with tempering temperature and heat

treatment process, following changes to the microstructural phases formed [9, 30].

Further work is currently underway to investigate the implications of local magnetism

and magnetic domains on resulting wear and corrosion mechanisms.

Similarly, the ability to resolve nanoscale variations in the resistance to

deformation (elastic modulus) on a material's surface could help improve prediction of

the wear behavior. The PeakForce tapping mode employed here measured differences in

the elastic modulus distribution, as determined via the Derjaguin-Muller-Toporov (DMT)

model [65], for the carbide and the matrices of the steels simultaneously with topography

(see exemplary Figure 5.12). As seen in the CN image presented in Figure 5.12, carbides

had a higher relative modulus than the matrix, suggesting potential sites for development

of micro-cracking and fracture would likely lie at the interface between carbides and matrix where local modulus variation was greatest. Further work is underway to determine how these local differences in recorded modulus correlate to a material's ability to handle loads/stress in bearing applications

In service, the uniform degradation seen on HTT could be effectively monitored conventionally via visual inspection, detection of wear debris, or thickness monitors installed on bearing raceways. For CN and LTT, current methods of monitoring engine health are less effective since significantly lower amounts of reaction products are generated from highly localized corrosion. Localized corrosion may not be detected until it has led to significant wear damage. Bearing steel developers should therefore be cautious with heat treatments that yield a surface similar to CN which, although highly corrosion resistant, the passive surface will inevitably be compromised in wear applications. Small areas of highly localized corrosion pits lead to surface crater development which can potentially lead to highly undesirable and unpredictable failure via spalling. LTT behavior was intermediate between the two other surface treatments, with some localized attack on grain/carbide boundaries as well as some evidence of wider depassivation. In corrosive environments, the overall wear lifetime may be controlled by resistance to corrosion initiation, in which case LTT and CN could provide greater benefit than HTT. Previously conducted wear studies are in agreement with the recommendations given, and the results of this study provide nanoscale insight to help understand why HTT outperformed both CN and LTT during rolling contact fatigue testing even though it had significantly lower corrosion resistance [29, 30]. Based on this work, P675 HTT would be recommended over the other two tempering procedures for

use in aerospace bearings where corrosion is not a primary concern. However, when the bearing assembly is prone to corrosion attack, HTT is not recommended due to its overall low corrosion resistance [7] which would lead to premature failure via degradation of the material. In this case, CN is recommended for bearing use due to its high resistance to both corrosion onset and propagation [7].

Conclusions

P675 carburizable martensitic stainless steel (UNS S42670) samples were processed using two different heat treatment methods (carburizing and carbo-nitriding (CN)) and two tempering temperatures (HTT and LTT). Following, the research conducted in this paper highlights the viability of SKPFM to effectively predict bulk corrosion behavior by measuring nanoscale surface differences in VPDs between carbides and the surrounding matrix, thereby providing insight into bulk observations by using information obtained at the nanoscale. More generally, SPM can be used to evaluate the potential efficacy of different steels and/or surface treatments for use in corrosive environments.

- • MFM imaging distinguished local differences in magnetic properties where precipitated carbides exhibited a larger magnetic moment than the matrix, likely due to the presence of chromium relative to the chromium-depleted matrix.

- • SKPFM VPD measurements in an inert environment showed HTT as the thermodynamically most favorable to experience microgalvanic corrosion between the chromium-rich precipitated carbides and the surrounding martensitic matrix, with a measured carbide-matrix VPD of 200 mV, while LTT (150 mV) and CN (90 mV) were less.

- Intermittent SKPFM showed the HTT sample behaved differently during corrosion than the LTT and CN samples; by the end of the testing period, there was minimal VPD between the HTT carbides and the surrounding matrix, whereas the carbides present in the LTT and CN samples retained their relative nobility throughout testing.

- Corrosion propagation was also monitored in real time via in situ AFM and revealed that HTT underwent the most rapid spread of corrosion attack across the sample, while LTT and CN were less affected and showed much more localized, intergranular attack and adjacent to carbides.

- Bulk electrochemical testing results agreed with in situ AFM results, with LTT and CN showing distinct passive regions as compared to HTT, confirming the nanoscale differences in corrosion behavior observed between the steel heat treatments investigated.

References

1. Bhadeshia, H. K. D. H. "Steels for bearings." *Progress in materials Science* 57.2 (2012): 268-435.

2. Davies, D. P. "Gear materials in helicopter transmissions." *Met. Mater.* 2.6 (1986): 342-347.

3. Zaretsky, Erwin V. "Rolling bearing steels–a technical and historical perspective." *Materials Science and Technology* 28.1 (2012): 58-69.

4. Zaretsky, Erwin V. "Bearing and gear steels for aerospace applications." *NASA Technical Memorandum 102529* (1990).

5. Hurley, Michael F., et al. "Corrosion assessment and characterization of aerospace-bearing steels in seawater and ester-based lubricants." *Corrosion* 68.7 (2012): 645-661.

6. Popgoshev, D., and R. Valori. "Rolling contact fatigue evaluation of advanced bearing steels." *Rolling Contact Fatigue Testing of Bearing Steels*. ASTM International, 1982.

7. Kvryan, A., Faulkner, E., Lysne, D., Carter, N., Acharya, S., Rafla, V., Trivedi, H. K., and Hurley, M. F., "Electrochemical Corrosion Test Methods for Rapid Assessment of Aerospace Bearing Steel Performance," Bearing Steel Technologies: 11th Volume, Progress in Steel Technologies and Bearing Steel Quality Assurance, ASTM STP1600, J. M. Beswick, Ed., ASTM International, West Conshohocken, PA, 2017, pp. 466–486, http://dx.doi.org/10.1520/STP1600201601503

8. Zaretsky, Erwin V., and Emanuel V. Branzai. "Rolling Bearing Service Life Based on Probable Cause for Removal—A Tutorial." *Tribology Transactions* 60.2 (2017): 300-312.

9. Trivedi, Hitesh K., Otto, Frederick, McCoy, Bryan, Bhattacharya, Rabi S., Piazza, Timothy, "Heat Treatment Process for Martensitic Stainless Steel Pyrowear 675 for Improved Corrosion Resistance." *Bearing Steel Technologies: 10th Volume, Advances in Steel Technologies for Rolling Bearings, STP 1580*; John M. Beswick, Ed., pp 465-484, doi:10.1520/STP158020140061, ASTM International: West Conshocken, PA 2015

10. Trivedi, Hitesh K. and Monahan, Ray, "Low Temperature Plasma Nitriding of Pyrowear 675." *Bearing steel Technologies: 10th Volume, Advances in Steel Technologies for Rolling Bearings, STP 1580*, John M. Beswick, Ed., pp 444-464, doi:10.1520/STP158020140062 ASTM International: West Conshocken, PA, USA, 2015

11. Dalmau, A., C. Richard, and A. Igual–Muñoz. "Degradation mechanisms in martensitic stainless steels: Wear, corrosion and tribocorrosion appraisal." *Tribology International* 121 (2018): 167-179.

12. Ma, X. P., et al. "Microstructure and properties of 13Cr5Ni1Mo0. 025Nb0. 09V0. 06N super martensitic stainless steel." *Materials Science and Engineering: A* 539 (2012): 271-279.

13. Thibault, Denis, Philippe Bocher, and Marc Thomas. "Residual stress and microstructure in welds of 13% Cr–4% Ni martensitic stainless steel." *Journal of Materials Processing Technology* 209.4 (2009): 2195-2202.

14. Li, C. X., and T. Bell. "Corrosion properties of plasma nitrided AISI 410 martensitic stainless steel in 3.5% NaCl and 1% HCl aqueous solutions." *Corrosion Science* 48.8 (2006): 2036-2049.

15. Smallman, Raymond E., and A. H. W. Ngan. *Physical metallurgy and advanced materials*. Elsevier, 2011.

16. Klueh, R. L., and Andrew T. Nelson. "Ferritic/martensitic steels for next-generation reactors." *Journal of nuclear materials* 371.1-3 (2007): 37-52.

17. Zinkle, Steven J. "Advanced materials for fusion technology." *Fusion engineering and design* 74.1-4 (2005): 31-40.

18. Puli, Ramesh, and GD Janaki Ram. "Microstructures and properties of friction surfaced coatings in AISI 440C martensitic stainless steel." *Surface and coatings Technology* 207 (2012): 310-318.

19. Anantha, Krishnan Hariramabadran, et al. "Correlative microstructure analysis and in situ corrosion study of AISI 420 martensitic stainless steel for plastic molding applications." *Journal of The Electrochemical Society* 164.4 (2017): C85-C93.

20. Klecka, Michael A. *Microstructure-property relationships and constitutive response of plastically graded case hardened steels*. 2011

21. Schneider, M. J., Chatterjee, M.S., and The Timken Company "Introduction to surface hardening of steels." *ASM Handbook, Steel Heat-Treating Fundamentals and Processes* 4 (2013).

22. Godec, Matjaž, et al. "Characterization of the carbides and the martensite phase in powder-metallurgy high-speed steel." *Materials characterization* 61.4 (2010): 452-458.

23. Callister, W. *Materials Science and Engineering*. New York: Wiley. (2007)

24. Johnson, Michael, et al. *Thin Dense Chrome Bearing Insertion Program; Pyrowear 675 and Cronidur Wear Testing*. GE, (1998)

25. Wert, David E. "Development of a carburizing stainless steel alloy." *Advanced Materials and Processes* 145.6 (1994): 89-91.

26. Trivedi, Hitesh K., Vern Wedeven, and William Black. "Effect of Silicon Nitride Ball on Adhesive Wear of Martensitic Stainless Steel Pyrowear 675 and AISI M-50 Races with Type II Ester Oil." *Tribology Transactions* 59.2 (2016): 363-374.

27. Hetzner, Dennis W., and William Van Geertruyden. "Crystallography and metallography of carbides in high alloy steels." *Materials Characterization* 59.7 (2008): 825-841.

28. Goldschmidt, H. J. "The structure of carbides in alloy steels. 2. Carbide formation in high-speed steels." *Journal of the Iron and Steel Institute* 170.3 (1952): 189.

29. Trivedi, H. K., Rosado, L., Gerardi, D. T., Givan, G. D., McCoy, B., "Fatigue Life Performance of Hybrid Angular Contact Pyrowear 675 Bearings." *Bearing Steel Technologies: 11th Volume, Progress in Steel Technologies and Bearing Steel Quality Assurance, ASTM STP 1600*; J.M. Beswick, Ed., ASTM International: West Conshohocken, PA, 2017, pp. 275–295 http://dx.doi.org/10.1520/STP160020170003

30. Kirsch, M. and Trivedi, H., "Microstructural Changes in Aerospace Bearing Steels under Accelerated Rolling Contact Fatigue Life Testing." *Bearing Steel Technologies: 11th Volume, Progress in Steel Technologies and Bearing Steel Quality Assurance, ASTM STP 1600*, J.M. Beswick, Ed., ASTM International: West Conshohocken, PA, 2017, pp. 92–107, http://dx.doi.org/10.1520/STP160020170005

31. Reynaud-Laporte, Isabelle, et al. "An electrochemical-AFM study of the initiation of the pitting corrosion of a martensitic stainless steel." *Microscopy Microanalysis Microstructures* 8.3 (1997): 175-185.

32. Leblanc, Patrick P., and G. S. Frankel. "Investigation of filiform corrosion of epoxy-coated 1045 carbon steel by scanning Kelvin probe force microscopy." *Journal of The Electrochemical Society* 151.3 (2004): B105-B113.

33. Schmutz, P., and G. S. Frankel. "Characterization of AA2024-T3 by scanning Kelvin probe force microscopy." *Journal of the Electrochemical Society* 145.7 (1998): 2285-2295.

34. Campestrini, P. E. P. M., et al. "Relation between microstructural aspects of AA2024 and its corrosion behaviour investigated using AFM scanning potential technique." *Corrosion Science* 42.11 (2000): 1853-1861.

35. De Wit, J. H. W. "Local potential measurements with the SKPFM on aluminium alloys." *Electrochimica Acta* 49.17-18 (2004): 2841-2850.

36. Larignon, Céline, et al. "Combined Kelvin probe force microscopy and secondary ion mass spectrometry for hydrogen detection in corroded 2024 aluminium alloy." *Electrochimica Acta* 110 (2013): 484-490.

37. Hurley, M. F., et al. "Volta potentials measured by scanning kelvin probe force microscopy as relevant to corrosion of magnesium alloys." *Corrosion* 71.2 (2014): 160-170.

38. Kvryan, Armen, et al. "Microgalvanic Corrosion Behavior of Cu-Ag Active Braze Alloys Investigated with SKPFM." *Metals* 6.4 (2016): 91.

39. Guillaumin, V., P. Schmutz, and G. S. Frankel. "Characterization of corrosion interfaces by the scanning Kelvin probe force microscopy technique." *Journal of the electrochemical society* 148.5 (2001): B163-B173.

40. Andreatta, F., H. Terryn, and J. H. W. De Wit. "Corrosion behaviour of different tempers of AA7075 aluminium alloy." *Electrochimica Acta* 49.17-18 (2004): 2851-2862.

41. Örnek, Cem, Christofer Leygraf, and Jinshan Pan. "Passive film characterisation of duplex stainless steel using scanning Kelvin prove force microscopy in combination with electrochemical measurements." *NPJ Materials Degradation* 3.8 (2019).

42. Anantha, Krishnan Hariramabadran, et al. "In Situ AFM Study of Localized Corrosion Processes of Tempered AISI 420 Martensitic Stainless Steel: Effect of Secondary Hardening." *Journal of The Electrochemical Society* 164.13 (2017): C810-C818.

43. Ramírez-Salgado, J., et al. "Detection of secondary phases in duplex stainless steel by magnetic force microscopy and scanning Kelvin probe force microscopy." *Materials Characterization* 86 (2013): 250-262.

44. Sathirachinda, Namurata, Rachel Pettersson, and Jinshan Pan. "Depletion effects at phase boundaries in 2205 duplex stainless steel characterized with SKPFM and TEM/EDS." *Corrosion Science* 51.8 (2009): 1850-1860.

45. Femenia, M., et al. "Scanning Kelvin probe force microscopy and magnetic force microscopy for characterization of duplex stainless steels." *Journal of the Electrochemical Society* 150.6 (2003): B274-B281.

46. Birbilis, N., et al. "In situ measurement of corrosion on the nanoscale." *Corrosion Science* 51.8 (2009): 1569-1572.

47. Davoodi, Ali, et al. "In situ investigation of localized corrosion of aluminum alloys in chloride solution using integrated EC-AFM/SECM techniques." *Electrochemical and solid-state letters* 8.6 (2005): B21-B24.

48. Guo, L. Q., et al. "Effect of annealing temperature on the corrosion behavior of duplex stainless steel studied by in situ techniques." *Corrosion Science* 53.11 (2011): 3733-3741.

49. Park, Jonghyun, et al. "In situ atomic force microscopy studies on lithium (de) intercalation-induced morphology changes in LixCoO2 micro-machined thin film electrodes." *Journal of Power Sources* 222 (2013): 417-425.

50. Leblanc, P., and G. S. Frankel. "A study of corrosion and pitting initiation of AA2024-T3 using atomic force microscopy." *Journal of the Electrochemical Society* 149.6 (2002): B239-B247.

51. Schmutz, P., and G. S. Frankel. "Corrosion study of AA2024-T3 by scanning kelvin probe force microscopy and in situ atomic force microscopy scratching." *Journal of the Electrochemical Society* 145.7 (1998): 2295-2306.

52. Efaw, Corey M., et al. "Toward Improving Ambient Volta Potential Measurements with SKPFM for Corrosion Studies." *Journal of the Electrochemical Society* 166.11 (2019): C3018-C3027.

53. Klecka, Michael A., Ghatu Subhash, and Nagaraj K. Arakere. "Microstructure–property relationships in M50-NiL and P675 case-hardened bearing steels." *Tribology Transactions* 56.6 (2013): 1046-1059.

54. Lind, Micheal A. *The infrared reflectivity of chromium and chromium-aluminum alloys*. Dissertation. Iowa State University, 1972.

55. Fawcett, Eric, et al. "Spin-density-wave antiferromagnetism in chromium alloys." *Reviews of modern physics* 66.1 (1994): 25.

56. Iga, Atsushi, and Yoshio Tawara. "Magnetic properties of molybdenum-and wolfram-Modified Mn3B4." *Journal of the Physical Society of Japan* 24.1 (1968): 28-35.

57. Mouritz, Adrian P. *Introduction to aerospace materials*. Elsevier, 2012.

58. Ahmad, Zaki. *Principles of corrosion engineering and corrosion control*. Elsevier, 2006.

59. Lauter, V., et al. "Reference module in materials science and materials engineering." (2016): 1-27.

60. Forman, Charles M., and E. A. Verchot. "Practical galvanic series". *No. RS-TR-67-11*. Army Missile Command Redstone Arsenal Al Systems Research Directorate, 1967.

61. Sathirachinda, Namurata, et al. "Characterization of phases in duplex stainless steel by magnetic force microscopy/scanning Kelvin probe force microscopy." *Electrochemical and solid-state letters* 11.7 (2008): C41-C45.

62. Mészáros, I., and P. J. Szabo. "Complex magnetic and microstructural investigation of duplex stainless steel." *NDT & E International* 38.7 (2005): 517-521.

63. Tavares, S. S. M., M. R. Da Silva, and J. M. Neto. "Magnetic property changes during embrittlement of a duplex stainless steel." *Journal of Alloys and Compounds* 313.1-2 (2000): 168-173.

64. Tavares, S. S. M., et al. "Magnetic properties of the UNS S39205 duplex stainless steel." *Journal of alloys and compounds* 351.1-2 (2003): 283-288.

65. Derjaguin, Boris V., Vladimir M. Muller, and Yu P. Toporov. "Effect of contact deformations on the adhesion of particles." *Journal of Colloid and Interface Science* 53.2 (1975): 314-326.

Figures

<div align="center">(a)   (b)   (c)</div>
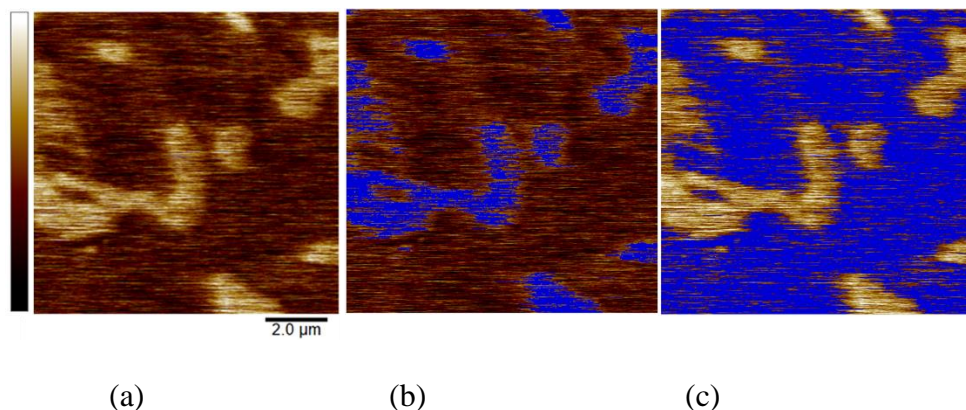
Figure 5.1   Representative 10 x 10 μm2 SKPFM images of P675-HTT. Dark brown corresponds to the softer matrix phase, which is lower in height following polishing than the harder, lighter brown carbides. Images show (a) the original Volta potential image (600 mV full scale range) and subsequent implementation of thresholding cutoffs (blue) to calculate average Volta potential differences (VPDs) for the (b) matrix and (c) carbides.


<div align="center">(a)</div>

	C	Cr	V	Mn	Mo	Co	Ni	Fe
HTT	4.1	12.5	0.5	0.8	0.6	5.4	2.12	72.9
LTT	5.3	13.0	0.6	0.7	1.6	5.2	2.4	70.8
CN	6.8	13.4	0.6	0.6	1.8	5.1	2.3	69.0

<div align="center">(b)</div>

Figure 5.2   (a) Grayscale BSE images (left column) of the three different P675 surface-treated samples (carbides appear darker than surrounding matrix) with corresponding colored EDS compositional maps highlighting the principal components of the carbides (middle columns) and bulk matrix (right columns) for the HTT, LTT, and CN samples (images for each row share the same micron bar). (b) Elemental composition in wt% (determined via EDS) for the surface of each steel (not individual carbides).
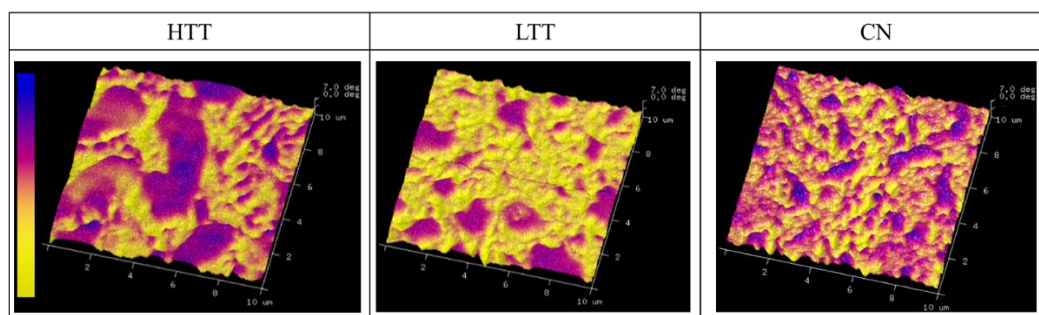
Figure 5.3   3D magnetic response maps with changes in height representative of differences in magnetism. Color scale ranges are 7 degrees (0° = yellow, +7° = blue) for magnetic response.
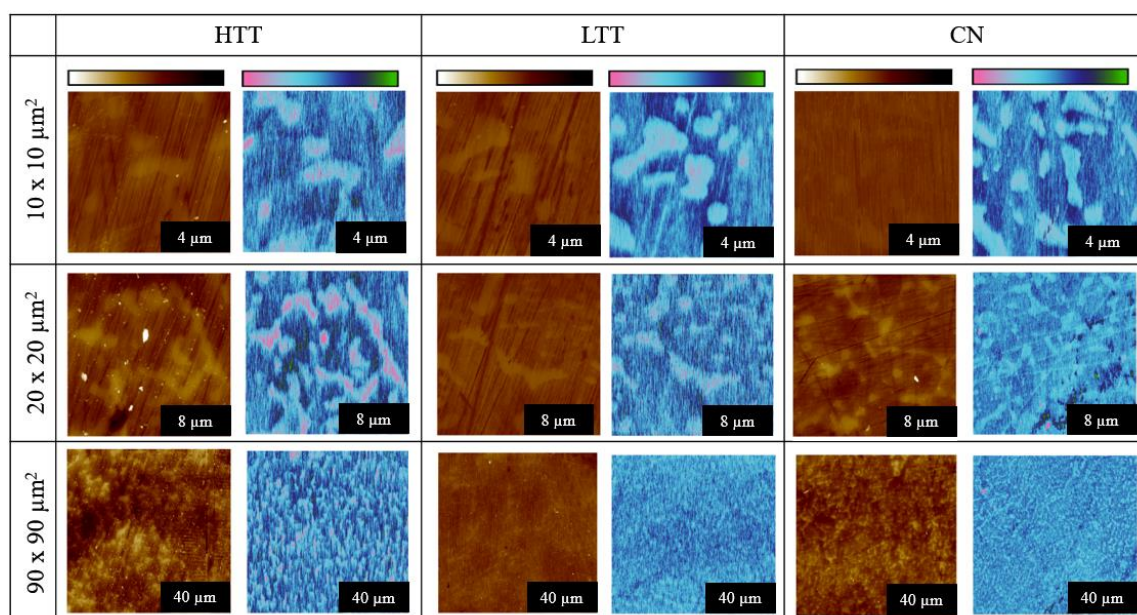

Figure 5.4   High resolution AFM topography (dark brown to white color scale, 100 nm full scale) and SKPFM Volta potential (green to pink color scale, 600 mV full scale) images over different size scan areas showing the different sizes and shapes of carbides distributed throughout the three sample types.
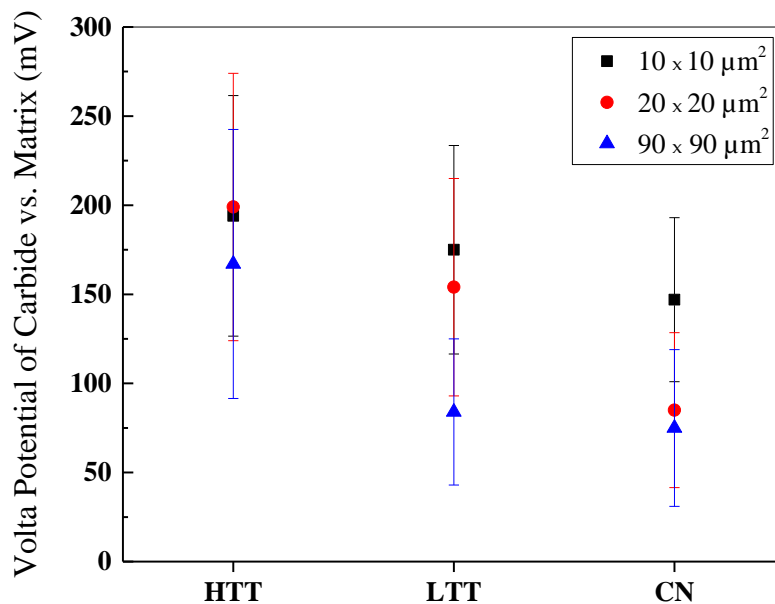
Figure 5.5 **Plot of measured VPDs (with standard deviation error bars) of carbide precipitates versus the surrounding matrix for the three P675 surface-treated steels as a function of scan area.**
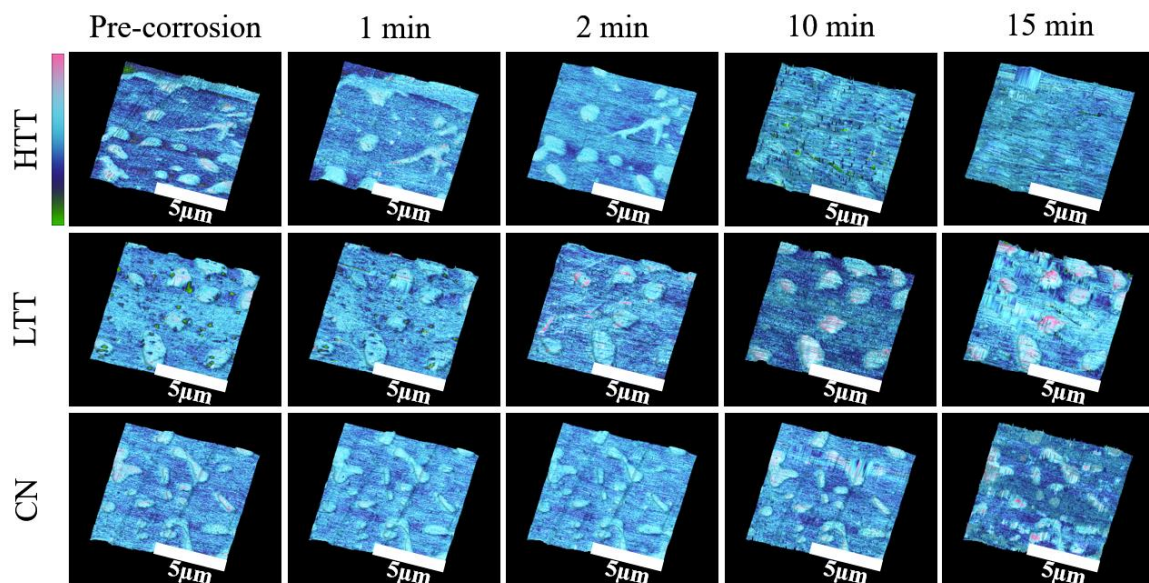

Figure 5.6 **SKPFM Volta potential maps (green to pink color scale-400 mV full scale) overlaid on the evolving 3D topography (30 nm full scale) of the three heat-treated MSSs as a function of immersion time in 1 M NaCl solution.**
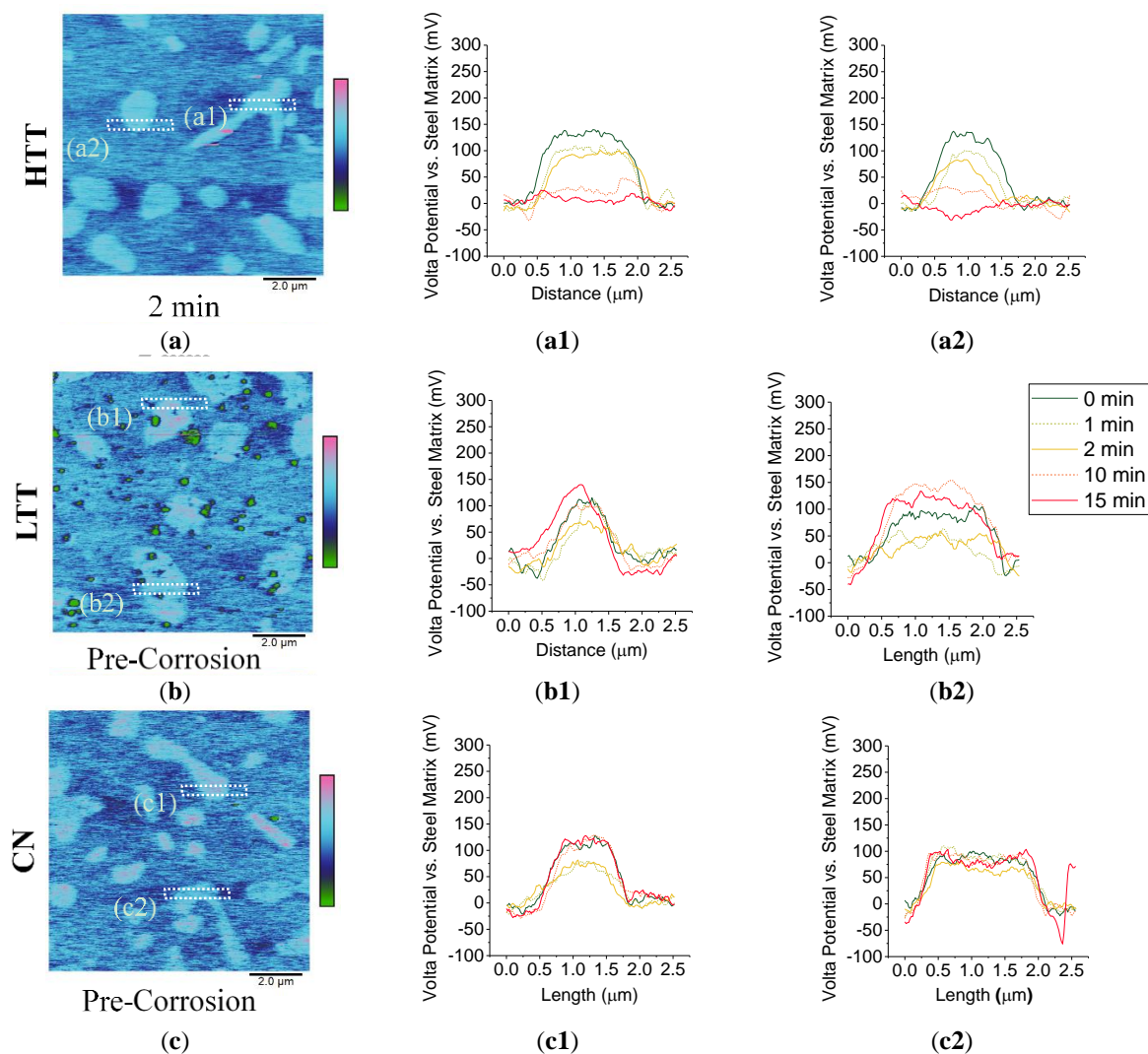
Figure 5.7 **SKPFM Volta potential maps ((a,b,c), 600 mV full scale, exposure time given below each image) for each of the three heat-treated MSSs with time-dependent Volta potential profiles (a1-c2) across two representative carbides plotted as a function of duration of exposure to 1 M NaCl solution. The location of the carbide represented by each profile is indicated by the corresponding dotted box in the exemplary SKPFM maps at left.**
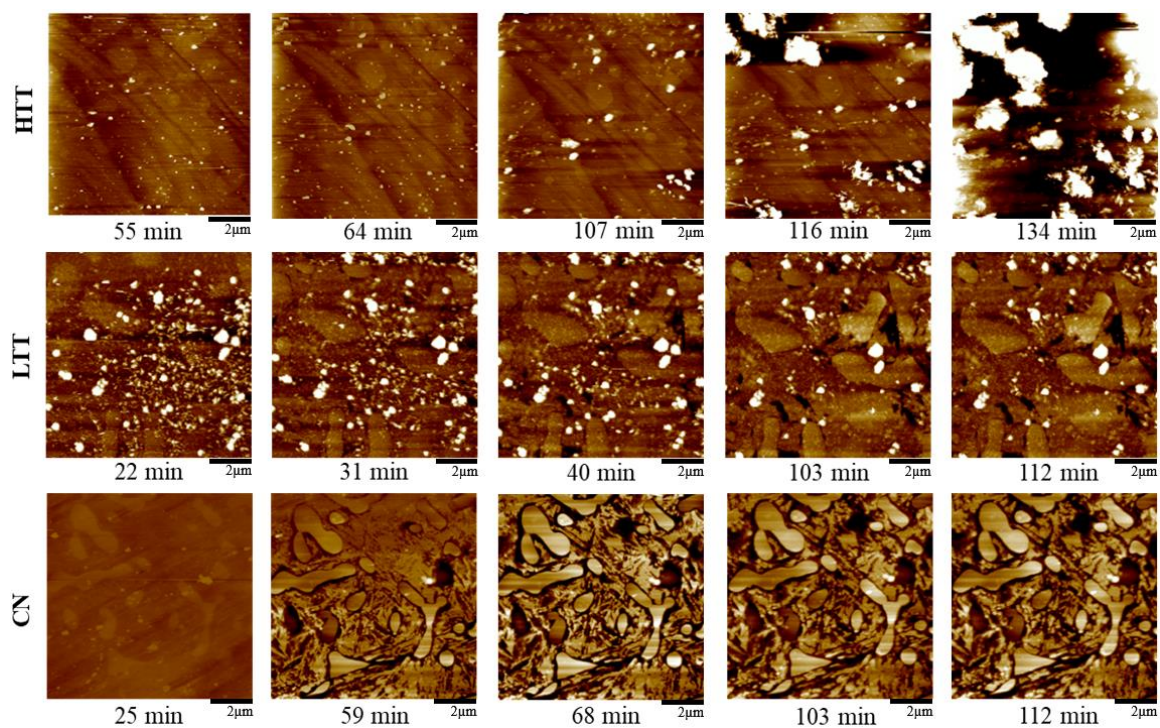
Figure 5.8   Time-lapse in situ AFM topography maps (160 nm full scale) for each of the heat-treated MSSs in 0.1 M NaCl solution, with approximate exposure time at the end of each scan indicated below the corresponding map (image time was ~8.5 min).
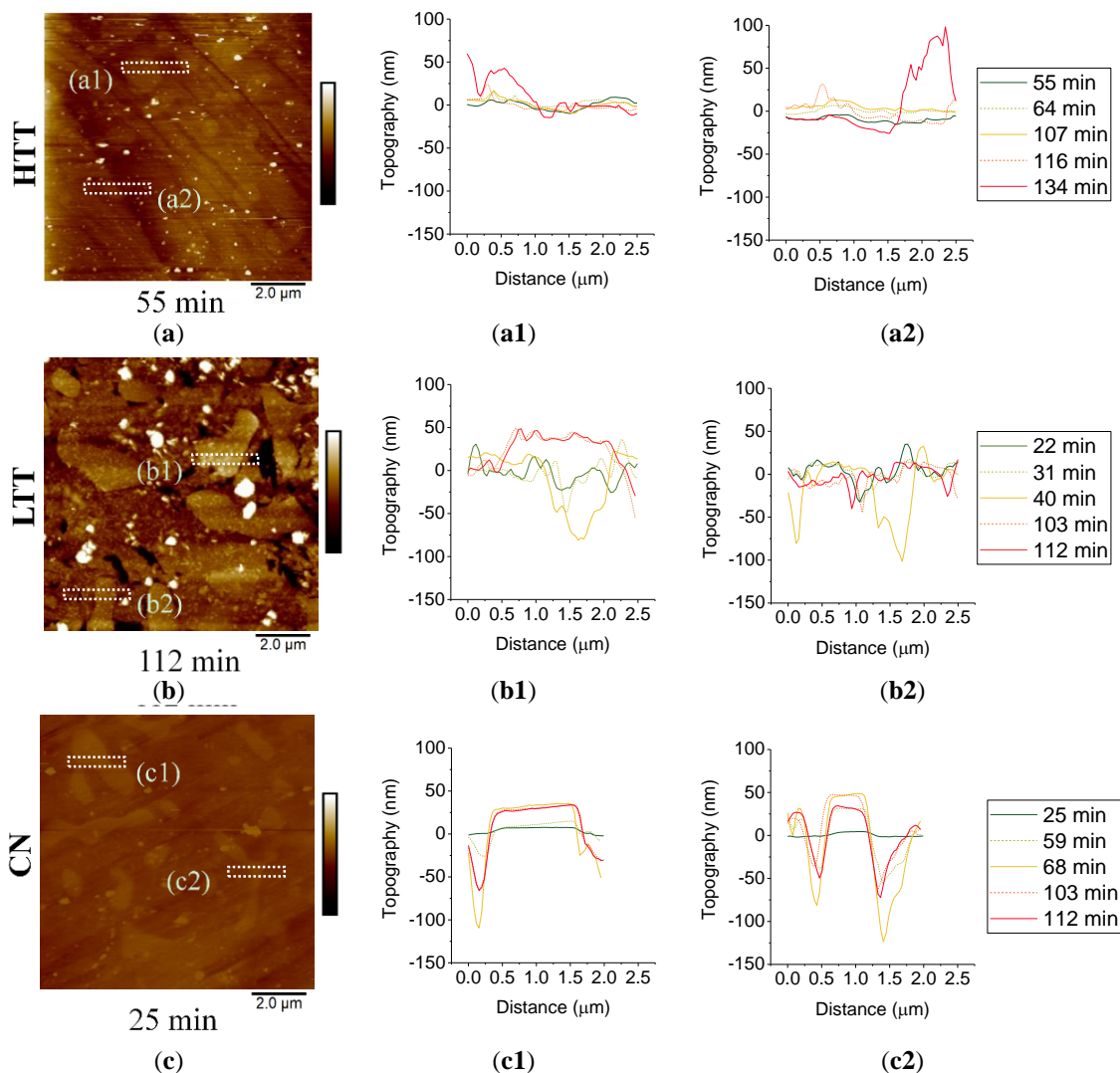
Figure 5.9 **Topography maps ((a,b,c), 160 nm full scale, exposure time indicated below corresponding map) for each of the three heat-treated MSSs with height profiles across selected carbide-matrix interfaces shown as a function of exposure time to 0.1M NaCl solution (a1-c2). Location of each profile is indicated by the corresponding box in the exemplary topography maps presented at left for each of the three heat-treated steels.**
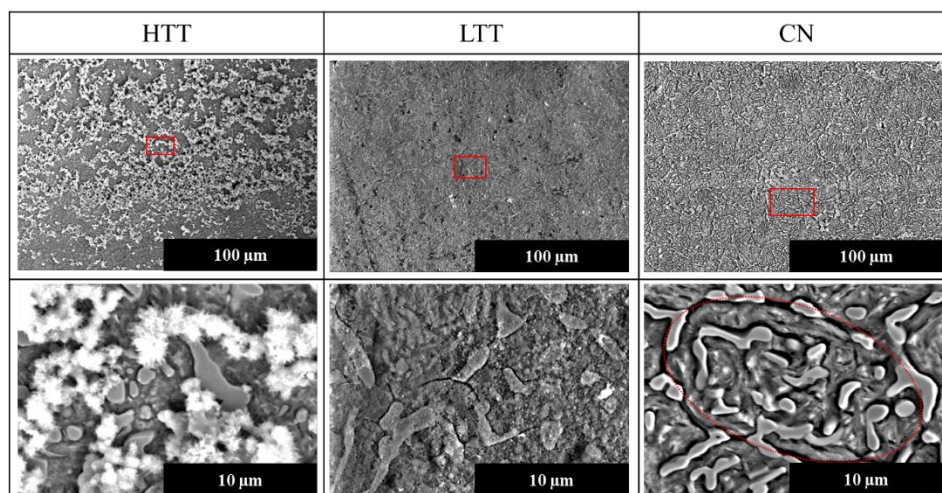
Figure 5.10 **SE SEM images of the sample surfaces following in situ AFM testing. Red squares in the images in the top panels indicate areas of magnified images below. Dotted red oval area in magnified CN image indicates the "line of attack" (see discussion).**
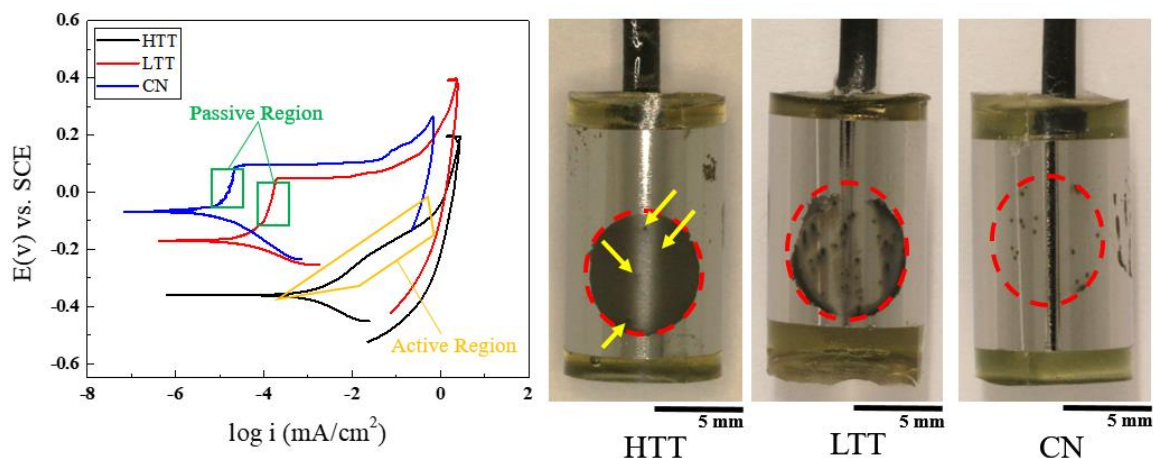
Figure 5.11 **(a) Cyclic potentiodynamic polarization (CPP) scans (0.01M NaCl electrolyte) for all three surface treatment samples. Passive regions for LTT and CN are indicated by green squares. (b) Images of the samples post-testing (after the area masking tape was removed) with dotted red circles indicating the test location on each sample surface. All samples display some isolated pitting; however due to the difficulty in clearly seeing the pits on the HTT sample (which, in contrast to the other samples, underwent generalized corrosion attack), yellow arrows indicate the location of the pits present on the HTT sample.**

(a)   (b)
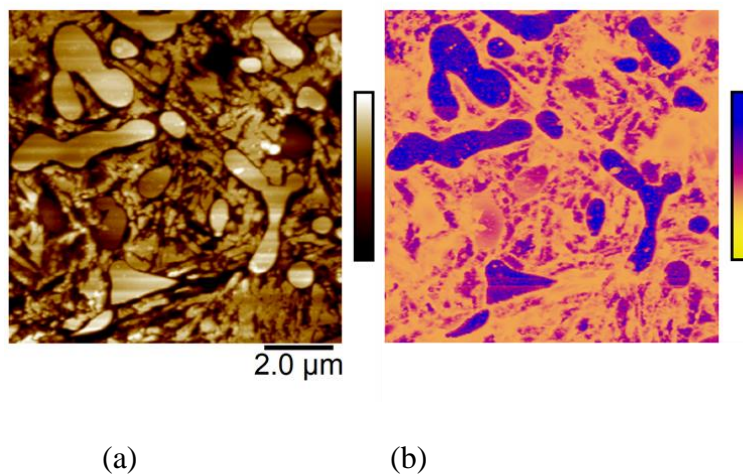
Figure 5.12 **(a) CN topography (160 nm full scale), and (b) DMT Modulus (1.5 GPa full scale). Images are representative of 103-112 minute submersion in 0.1M NaCl solution.**

Tables

Table 5.1 **Nominal composition (wt%) of P675 alloy (remainder is Fe). Adapted from Trivedi et al.**

Steel	C	Mn	Cr	Mo	Si	Ni	S	V	Co
Pyrowear 675 (AMS 5930B)	0.07	0.75	13	2	0.4	2.5	0.010	0.6	6.5

.

CHAPTER SIX: CONCLUSIONS

This work investigated the effects of heat treatment on MSS P675. In Chapter one, a brief introduction was given into how bearings currently in use have poor corrosion resistance and ultimately lead to premature failure. Current methods typically used by industry and government entities to measure corrosion resistance to rank steels, (e.g. salt spray chamber) are qualitative and based on observation. To advance understanding, Chapter two provided a rapid method to rank bearing steels based on corrosion resistance by using advanced electrochemical techniques such as AP and EIS. This was the first time these techniques were used to rank bearing steels and it was demonstrated that empirical calculators, such as PREN, were not a good predictors of corrosion behavior for case hardened bearing steels. Corrosion rate measurements verified previous findings that common bearings used today (i.e., M50) have poor corrosion resistance. Results from this study showed that corrosion behavior of P675 is highly dependent on the final heat treatment. This prompted a more focused investigation into how heat treatment affects the corrosion performance of P675. Specifically HTT, LTT, and CN were chosen because they are considered for the Department of Defense (DoD) applications.

In Chapter three, data obtained from EIS testing was fitted to a modified Randles circuit {R1+CPE1/ (R2+CPE3/R3)}. This model allowed the extraction of fitting parameters that were, in turn, used for developing and proposing a corrosion mechanism for each heat treated P675; HTT underwent general corrosion attack while LTT and CN

corroded via pitting. Carbide analysis revealed HTT had the largest and most amount of carbides, while LTT and CN were smaller and less frequent. Standard bulk electrochemical testing, such as AP and EIS methods do not accurately resolve all surface phenomena. Nanoscale testing is necessary to obtain more surface information. However, the P675 samples received were cylindrical in shape and were difficult to test.

Chapter four demonstrated a proof-of-concept whereby SPM techniques, specifically SKPFM, were co-localized with alloying composition (EDS) and electrochemical measurements to effectively predict corrosion initiation sites. These microgalvanic initiation sites were easier to resolve due to the larger features and the flatness of the sample. The knowledge acquired from Chapter four was used to monitor corrosion progression on the nanoscale using in-situ AFM and time-dependent SKPFM in Chapter five. This was a new and novel application of the technique to bearing steels.

In Chapter five, SKPFM results indicated that HTT was thermodynamically most favorable to experience microgalvanic corrosion between the chromium-rich precipitated carbides and the surrounding martensitic matrix. Intermittent SKPFM showed the HTT sample behaved differently during corrosion than the LTT and CN samples; by the end of the testing period, there was minimal VPD (i.e. minimal driving force for corrosion) between the HTT carbides and the surrounding matrix, whereas the carbides present in the LTT and CN samples retained their relative nobility throughout testing. Real time corrosion progression revealed that HTT underwent the most rapid spread of corrosion attack, while LTT and CN were less affected and showed much more localized, intergranular attack adjacent to carbides. Therefore Chapter five validated the corrosion mechanism proposed in Chapter three and the equivalent circuit used (i.e. modified

Randles circuit). Most notably, Chapter five highlights the viability of advanced SPM techniques to evaluate the potential efficacy of different steels and/or surface treatments for use in corrosive environments.

Since requirements for bearings are always evolving, steel designers are constantly engineering alloys using different alloying elements and heat treatments. This study contributes to the field of knowledge on how heat treatment affects corrosion performance of P675 and has shown that advanced surface characterization combined with electrochemical testing can be used to effectively predict corrosion performance for P675 and MSS's.

CHAPTER SEVEN: FUTURE WORK

Although a corrosion mechanism was proposed for each of the three heat treatments studied here, further work must be completed to determine how corrosion behavior affects wear. Specifically corrosive wear testing must be conducted on these steels to help correlate to actual wear in-service. A general guideline and suggestion on testing parameters is given here. A conventional Ball-on-Rod testing apparatus would be used to measure rolling contact fatigue where the baseline would be 208-size angular (40 mm) M50 hybrid bearings (M50 raceway and ceramic Si_3N_4 rolling elements). Based on previous wear testing the thrust load should range from 14000-23000 N, maximum Hertzian stress from 3.1-5.5 GPa, and lubricant used would be MIL-PRF-23699G (viscosity of 5 cSt at 100°C) with the possible addition of tribofilm enhancers/anti-wear additives (e.g. tricresyl phosphate (TCP)). Testing would conclude if the accelerometer measures 1g or greater and testing would be terminated if bearings survive 5000 hours. To observe wear behavior in corrosive applications two suggestions are presented:

1) The oil would not be filtered when returning to the system

2) The lubricant used has embedded metal particulates or NaCl added to it

One way to assess the corrosion behavior of these bearing steels as a function of wear could be to electrochemically test samples that underwent wear testing and predetermined times. That is, to subject samples to wear testing, and obtain samples at time intervals (e.g 500h, 1000h, 2000h, etc.) and observe how the steels corrosion behavior changes with the new introductions to the surface.

Also, the electrolyte solution used for electrochemical testing could better mimic the bearing environment in-service. That is, the solution could be prepared to contain some lubricant additives, while too much lubricant in the electrolyte can cause large resistance, which would hinder the experiment by not allowing charge transfer amongst the electrodes. Finally, by stirring the electrolyte media for the duration of the test, it would more accurately depict the constantly moving lubricant found in the actual aerospace bearing systems.